THERMAL RADIATIVE ENERGY TRANSFER IN POLARITONIC NANOSTRUCTURE ARRAYS

A Dissertation
Presented to
The Academic Faculty

By

Eric James Tervo

In Partial Fulfillment
Of the Requirements for the Degree
Doctor of Philosophy in Mechanical Engineering

Georgia Institute of Technology

December 2019

THERMAL RADIATIVE ENERGY TRANSFER IN POLARITONIC NANOSTRUCTURE ARRAYS

Approved by:

Dr. Baratunde Cola, Co-Advisor
G.W.W. School of Mechanical Engineering
Georgia Institute of Technology

Dr. Mathieu Francoeur
Department of Mechanical Engineering
University of Utah

Dr. Zhuomin Zhang, Co-Advisor
G.W.W. School of Mechanical Engineering
Georgia Institute of Technology

Dr. Satish Kumar
G.W.W. School of Mechanical Engineering
Georgia Institute of Technology

Dr. Michael Filler
School of Chemical and Biomolecular Engineering
Georgia Institute of Technology

Date Approved: July 26, 2019

To my wife, Allison

ACKNOWLEDGEMENTS

I would first and foremost like to thank my advisors, Dr. Baratunde Cola and Dr. Zhuomin Zhang, for their guidance and support throughout my Ph.D. Their advice and encouragement have been and will continue to be instrumental to my career. I have been fortunate to collaborate with several outstanding faculty members and students who have helped me to achieve my research goals, including Dr. Michael Filler, Dr. Mathieu Francoeur, Dr. James Hammonds, Michael Gustafson, Dmitriy Boyuk, Lindsay Walter, Zachary Herbst, Olalekan Adewuyi, Anil Yuksel, Dudong Feng, and Elham Bagherisereshki. I would also like to thank the past and current members of the NanoEngineered Systems and Transport Laboratory and the Nanoscale Thermal Radiation Laboratory for their ideas, assistance, and friendship throughout graduate school.

Finally, I would like to thank my family, especially Lori, Steve, Megan, Craig, and Allison. Their love and support, above all else, have enabled me to reach where I am today.

TABLE OF CONTENTS

LIST OF FIGURES

LIST OF SYMBOLS AND ABBREVIATIONS

$\mathbb{A}$	interaction matrix [units vary]
A_c	cross-sectional area [m^2]
A_0	constant in plasmon ruler equation [-]
a	radius [m]
AR	aspect ratio (LD^{-1}) [-]
c	speed of light in vacuum [2.998×10^8 m s^{-1}]
Br	Brillouin zone [m^{-1}]
D	diameter [m]
D_{1D}	one-dimensional density of states [s m^{-1}]
D_{3D}	three-dimensional density of states [s m^{-3}]
d	center-to-center separation distance [m]
DDA	discrete dipole approximation
DOS	density of states
DSC	differential scanning calorimetry
$\mathbf{E}$	electric field [N C^{-1}]
F	force [N]
$f^{(\mathrm{BE})}$	Bose-Einstein distribution function [-]
FE	fluctuational electrodynamics
FTIR-ATR	Fourier transform infrared attenuated total reflection
$\mathbb{G}$	dyadic Green's function [m^{-1}]
$\mathbb{G}^{(0)}$	free-space dyadic Green's function [m^{-1}]
G	thermal conductance [W K^{-1}]

$\mathbf{H}$ magnetic field [A m^{-1}]

h Planck constant [6.626×10^{-34} J s]

$\hbar$ reduced Planck constant [1.055×10^{-34} J s]

$\mathbb{I}$ identity matrix [-]

i imaginary unit ($\sqrt{-1}$)

∞ infinity [-]

$\mathbf{J}$ electric current density [A m^{-2}]

k wavevector, also $\tilde{k}$ ($\sqrt{\omega^2\mu_0\varepsilon_0\varepsilon_m}$ or $\omega\sqrt{\varepsilon_m}/c$) [$m^{-1}$]

k_B Boltzmann constant [1.381 J K^{-1}]

K spring constant [N m^{-1}]

KT kinetic theory

L length [m]

m effective mass [kg]

MB many-body method

N number of particles or subvolumes in system [-]

N_e dopant concentration [cm^{-3}]

NFRHT near-field radiative heat transfer

$\mathcal{O}$ on the order of

$\mathbf{p}$ dipole moment [C m]

Q heat transfer rate [W]

q charge [C]

$\mathbf{r}$ location vector [m]

$\mathbf{R}$ distance vector ($\mathbf{r}_1 - \mathbf{r}_2$) [m]

R distance ($|\mathbf{R}|$) [m]

$\mathbf{S}$	Poynting vector [W m^{-2}]
S	separation distance [m]
SP	surface polariton
SPhP	surface phonon polariton
SPP	surface plasmon polariton
T	temperature [K]
t	time [s]
$\mathcal{T}$	transmission coefficient [-]
T-DDA	thermal discrete dipole approximation
u	spectral energy density [J m^{-3} (rad s^{-1})$^{-1}$]
V	volume [m^3]
v_g	group velocity [m s^{-1}]

Greek Symbols

$\alpha^{(0)}$	bare polarizability [m^3]
$\alpha^{(\mathrm{CM})}$	Clausius-Mossotti polarizability [m^3]
$\alpha^{(\mathrm{d})}$	dressed polarizability [m^3]
χ	reduced absorption factor [m^3]
δ	Kronecker delta function [-]
ε	complex relative permittivity, also $\tilde{\varepsilon}$ [-]
ε_0	vacuum permittivity [8.854×10^{-12} F m^{-1}]
ε_m	relative permittivity of background medium [-]
$\epsilon_{\alpha\beta\gamma}$	alternating unit tensor ($\epsilon_{123/312/231}$ = 1, $\epsilon_{321/132/213}$ = -1, else $\epsilon_{\alpha\beta\gamma}$ = 0)
Γ	damping rate or scattering rate [rad s^{-1}]

κ thermal conductivity [W m^{-1} K^{-1}]

Λ energy propagation length or mean free path [m]

Λ_a amplitude propagation length [m]

λ wavelength [m]

λ_T characteristic thermal wavelength ($\hbar c(k_B T)^{-1}$) [m]

μ_0 vacuum permeability [$4\pi\times10^{-7}$ H m^{-1}]

ω angular frequency, also $\widetilde{\omega}$ [rad s^{-1}]

ω_1 natural frequency or absorption peak position of isolated resonator [rad s^{-1}]

ω_2 Absorption peak position of two adjacent resonators [rad s^{-1}]

ω_c coupling strength [rad s^{-1}]

Φ humidity ratio [%]

π pi [3.14159…]

σ Stefan-Boltzmann constant [5.670×10^{-8} W m^{-2} K^{-4}]

τ decay length scaling factor in plasmon ruler equation [-]

Θ mean energy of a Planck oscillator ($\hbar\omega f^{(\mathrm{BE})}$) [J]

ξ damping ratio (ζm^{-1}) [rad s^{-1}]

ζ damping coefficient [kg s^{-1}]

Superscripts

E electric

(fl) due to thermal fluctuations

H magnetic

(inc) incident part

(ind) induced part

(MB)	in the many-body method
(TDDA)	in the thermal discrete dipole approximation

Subscripts

$\parallel$	longitudinal
$\perp$	transverse
0	in vacuum
1,2,3,…	index of object under consideration
$\alpha, \beta, \gamma, ...$	indices 1,2,3 representing Cartesian components of vector quantities
b	thermal bath
H	hot object
LO	longitudinal optical
C	cold object
TO	transverse optical

Operators

$*$	complex conjugate
$\dagger$	conjugate transpose
$\times$	cross product
$\langle\,\rangle$	ensemble average
Im( )	imaginary part
$\cdot$	inner product
$\otimes$	outer product
Re( )	real part
Tr( )	trace

SUMMARY

Thermal radiation in arrays of nanostructures can exhibit interesting and unusual collective effects. When the nanostructures support surface plasmon polaritons or surface phonon polaritons, coupling between nanostructures can be very strong and enable large radiative energy transfers. These traits have led researchers to investigate polaritonic nanostructure arrays for a variety of energy transport applications. However, practical implementations have been limited due to deficiencies in the understanding of their thermal and electromagnetic interactions, particularly for closely spaced nanostructures and nonhomogeneous environments.

This dissertation aims to improve the theoretical description, advance the modeling approach, and perform an experimental investigation of radiative energy transport in polaritonic nanostructure arrays. On the experimental side, the thermal properties of packed beds of coated silica nanoparticles are measured, and the results suggest that their thermal conductivities exhibit significant radiative contributions. To model these and other types of nanostructure arrays, two theoretical formalisms are utilized and further developed. The first is a kinetic theory approach, which is used to investigate the radiative thermal conductivity of nanoparticle chains in isotropic surroundings. For more complex geometries and environments, a new kinetic modeling method is developed based on absorption spectroscopy data. The second is an exact method based on fluctuational electrodynamics. Two different approaches to this formalism, the many-body method and the thermal discrete dipole approximation, are unified and shown to be mathematically equivalent. A new, computationally efficient approach to fluctuational electrodynamics

methods using system Green's functions is also developed. To compare thermal radiation to other modes of heat transfer, an algorithm to determine radiative thermal conductivity from fluctuational electrodynamics is established and applied to ordered and disordered nanoparticle arrays.

Results from these studies provide insight on the interactions between thermal and electromagnetic effects, and they demonstrate that radiation in polaritonic nanostructure arrays can be a significant contributor to thermal transport. By comparing the kinetic formalism to the fluctuational electrodynamics formalism, it is shown that collective propagating polaritons dominate thermal radiation when those modes are supported and thermally activated. In dense polaritonic particle arrays, heat transfer by thermal radiation can approach the magnitude of phonon conduction. A new material structure consisting of repeated plasmonic resonators embedded in a semiconductor nanowire is also proposed that can achieve high radiative thermal conductivities.

The findings and methods presented here enhance the understanding of radiative heat transfer among nanostructures. This will facilitate the future development of material systems for guided, enhanced, and tunable thermal transport, with applications in thermal management, nanomanufacturing, and energy conversion.

CHAPTER 1. INTRODUCTION

The theoretical formulation by Polder and Van Hove in 1971 [1] and clear demonstration by Hu *et al.* in 2008 [2] of radiative heat transfer across nanoscale gaps exceeding the blackbody limit initiated a great deal of research on near-field thermal radiation and its applications. For certain materials that support surface polaritons (SPs), the energy exchange may be increased by orders of magnitude compared to the far-field limit [3], making this a promising phenomenon for technologies in thermal microscopy, thermal management, and energy conversion, among others. However, despite enormous progress in the investigation of near-field radiative heat transfer (NFRHT), it remains very difficult to fabricate and maintain the nanoscale gaps across large areas called for in many proposed devices [4, 5]. To illustrate the scope of this challenge, a 100 nm gap between parallel plates 1 cm wide is analogous to a 1 mm gap between plates 100 m wide. Even minor roughness or bowing will bring the surfaces into contact and alter the nature of the energy exchange.

An alternative approach to utilize NFRHT without the complications of macroscale parallel surfaces is to use nanostructures as the energy-exchanging materials. Over the past few decades there has been tremendous development in the ability to synthesize and manipulate nanostructures [6, 7]. This permits very precise design and fabrication of nanostructure arrays, both from a geometric and a materials perspective. Additionally, the phonon/electron thermal transport within an individual nanostructure and between adjacent contacting structures is significantly reduced due to size effects [8] and contact resistance [9], allowing NFRHT to play a more significant role in the total thermal

transport. These factors have motivated several researchers to develop theoretical and numerical formalisms for radiative exchange between many nanostructures [10], which include kinetic descriptions of propagating energy carriers analogous to phonon transport as well as exact methods that are based on Maxwell's equations. Because the field is relatively new, however, there are still discrepancies in some theoretical approaches, geometric limitations to modeling methods, and a lack of experimental studies on NFRHT between nanostructures.

The potential applications of NFRHT between nanostructures are numerous and make this topic well-worth further investigation. Some, such as solid-state near-field radiative energy converters (e.g. thermophotovoltaic cells) [5], have been studied in detail for NFRHT between macroscale planar surfaces. Using nanostructures as the emitter and/or cell could lead to novel architectures and simpler fabrication. Another example is the possibility of tunable heat transfer by active manipulation of optical properties, such as through gating or optical pumping of doped semiconductors [11], or by judicious material selection, such as using phase-change VO_2 to change from insulator to metallic behavior near a certain temperature [12]. Other applications are unique to many nanostructures, such as designing particle beds or nanowire arrays to dissipate heat through NFRHT interactions in addition to thermal conduction. As the understanding of these effects progresses, additional unforeseen behaviors and possibilities are sure to emerge.

This dissertation aims to improve the theoretical description, advance the modeling approach, and perform an experimental investigation of radiative energy transport in polaritonic nanostructure arrays. Measurements of the thermal properties of packed nanoparticle beds are conducted to resolve radiative contributions to thermal transport.

Various modeling approaches are used to investigate NFRHT in ordered and disordered particle arrays, and some aspects of these models are clarified and improved. Additionally, a new modeling approach is developed for nanostructures in nonhomogeneous environments.

The remainder of this dissertation is organized as follows:

- Chapter 2 provides background information on NFRHT and relevant classical electromagnetic (non-thermal) theory for nanostructure arrays, and it presents a review of previous research on thermal radiation in nanostructure arrays. The need for additional research is identified and the objectives of this dissertation are stated.
- Chapter 3 presents results from an experimental study of the effect of NFRHT on the thermal conductivity of packed beds of coated silica nanoparticles. This chapter demonstrates the need for improved modeling methods for thermal radiation between nanostructures.
- Chapter 4 develops a new kinetic modeling method for nanostructures in nonhomogeneous environments. The new method is used to propose a nanowire structure capable of sub-diffractional waveguiding and achieving radiative thermal conductivities comparable to the phonon and electron thermal conductivities.
- Chapter 5 unifies two existing formalisms of fluctuational electrodynamics for nanoparticles or discretized bodies, and it details a computational method to predict the radiative thermal conductivity from fluctuational electrodynamics. This approach is applied to ordered and disordered nanoparticle arrays. A system Green's function approach to this method is also developed for improved computational efficiency.

- Chapter 6 examines the correspondence of the kinetic and fluctuational electrodynamics methods by comparing predictions of thermal emission, density of photonic states, and radiative thermal conductivities.
- Chapter 7 summarizes conclusions from the present studies and recommends topics for future research.

CHAPTER 2. BACKGROUND AND OBJECTIVES

The theory and application of thermal radiation between many nanostructures is motivated by the phenomenon of NFRHT and rooted in the theory of classical electromagnetic coupling between small particles. This chapter introduces the concept of NFRHT and describes the computational and experimental advances in the field. It also presents the relevant background on classical electromagnetic theory for small particles, focusing on the sub-fields of sub-diffractional waveguiding and the discrete dipole approximation (DDA) that are adapted for thermal radiation calculations. A review of the literature on thermal radiation between many nanostructures is provided, which is split into the theoretical formalisms of kinetic theory (KT) and fluctuational electrodynamics (FE) that have been employed. Finally, the objectives of this dissertation are discussed.

2.1 Near-Field Thermal Radiation

All objects emit electromagnetic radiation due to random thermal fluctuations of charges within the material. When two macroscale objects are separated by distances greater than the characteristic thermal wavelength $\lambda_T = \hbar c (k_B T)^{-1}$, the radiative heat exchange is described by Planck's law and the materials' optical properties. The maximum net radiative heat flux is given in the blackbody limit as $\sigma(T_1^4 - T_2^4)$ if the objects absorb all incident radiation. However, this description is only valid if the size of the objects and their separation distance are larger than λ_T, which was recognized by Planck himself in his book on thermal radiation [13].

2.1.1 Conceptual Framework

When the distance between two objects is smaller than λ_T, the energy transfer can be significantly increased and exceed the far-field blackbody limit [1, 3, 4, 8, 14-21]. This

enhancement is caused by photon tunneling due to the presence of evanescent waves between the objects. When electromagnetic waves travel from within a material to an optically rarer medium at incidence angles greater than the critical angle, the wave is totally reflected inside the first material as illustrated in Figure 2.1. If total internal reflection occurs, an evanescent wave whose magnitude decays exponentially away from the interface exists in the second medium. The time averaged Poynting vector normal to the interface is zero, hence energy is not transferred from the first to the second medium. However, if another optically dense third material is placed close to the first one as shown in Figure 2.1, a reflected evanescent wave is formed due to the second interface [14]. The Poynting vector of the coupled evanescent fields has a nonzero normal component, and energy is transmitted between the first and third materials.

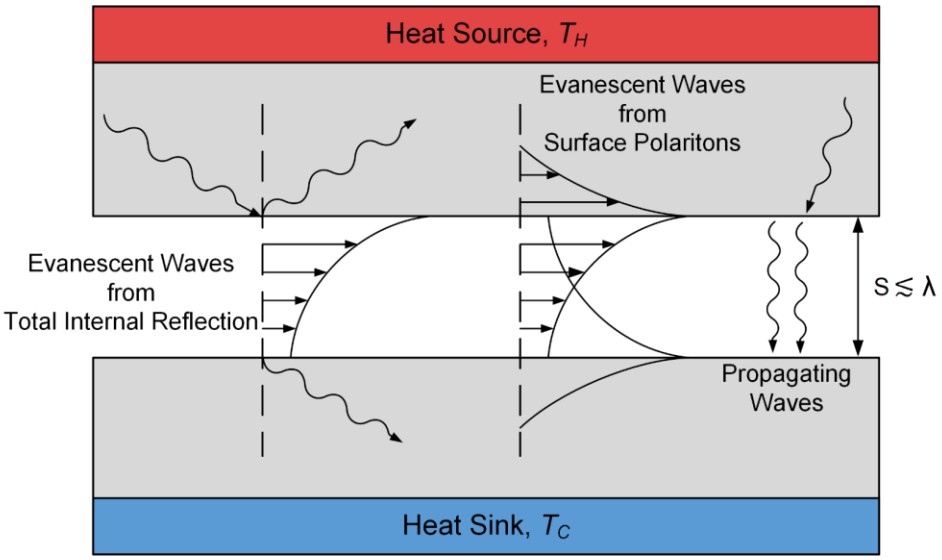

Figure 2.1. Schematic of propagating and evanescent waves contributing to near-field radiation heat transfer.

This phenomenon is known as photon tunneling, and this type of evanescent wave is referred to as a frustrated mode. Some materials such as polar dielectrics or noble metals

can support evanescent surface modes on both sides of an interface called surface phonon polaritons (SPhPs) or surface plasmon polaritons (SPPs). These can increase the radiation exchange even further [20] and are also depicted in Figure 2.1. SPs are caused by coherent oscillations of free electrons (SPPs) in noble metals or doped semiconductors and by optical phonon vibrations of bound charges (SPhPs) in polar dielectrics [22].

The thermal electromagnetic interactions between objects can be characterized via FE. This formalism describes thermally generated electromagnetic fields as a result of fluctuating thermal currents within a material. The thermal currents may be directly incorporated into Maxwell's equations by adding a $\mathbf{J}^{(\mathrm{fl})}$ term to Ampère's law. Using $f(t) = \int_{-\infty}^{\infty} \frac{d\omega}{2\pi} f(\omega) \mathrm{e}^{-i\omega t} = 2\mathrm{Re}\left[\int_{0}^{\infty} \frac{d\omega}{2\pi} f(\omega) \mathrm{e}^{-i\omega t}\right]$ as the Fourier transform convention (which is used throughout this dissertation), the differential forms of Faraday's law and Ampère's law for nonmagnetic materials may be written in the frequency domain as

$$\nabla \times \mathbf{E}(\mathbf{r}, \omega) = i\omega\mu_0 \mathbf{H}(\mathbf{r}, \omega) \tag{2.1}$$

$$\nabla \times \mathbf{H}(\mathbf{r}, \omega) = \mathbf{J}^{(\mathrm{fl})}(\mathbf{r}, \omega) - i\omega\varepsilon_0 \varepsilon(\mathbf{r}, \omega)\mathbf{E}(\mathbf{r}, \omega) \tag{2.2}$$

where $\varepsilon(\mathbf{r}, \omega)$ denotes the complex relative permittivity. Taking the curl of Equation (2.1) and inserting Equation (2.2) yields the vectorial wave equation for the electric field:

$$\nabla \times \nabla \times \mathbf{E}(\mathbf{r}, \omega) - k_0^2(\omega)\varepsilon(\mathbf{r}, \omega)\mathbf{E}(\mathbf{r}, \omega) = i\omega\mu_0 \mathbf{J}^{(\mathrm{fl})}(\mathbf{r}, \omega) \tag{2.3}$$

where k_0 is the wavevector in vacuum. A similar equation can be obtained for the magnetic field. One solution to the vectorial wave equations is provided by the dyadic Green's functions for the fields [23]:

$$\mathbf{E}(\mathbf{r},\omega) = i\omega\mu_0 \int_V \mathbb{G}^E(\mathbf{r},\mathbf{r}',\omega)\cdot\mathbf{J}^{(\mathrm{fl})}(\mathbf{r}',\omega)dV' \tag{2.4}$$

$$\mathbf{H}(\mathbf{r},\omega) = \int_V \mathbb{G}^H(\mathbf{r},\mathbf{r}',\omega)\cdot\mathbf{J}^{(\mathrm{fl})}(\mathbf{r}',\omega)dV' \tag{2.5}$$

where the Green's functions depend on the geometry of the system. $\mathbf{J}^{(\mathrm{fl})}$ is a stochastic quantity whose ensemble average is zero. The ensemble average of its spatial correlation function, however, is nonzero and is given by the fluctuation-dissipation theorem [24]:

$$\left\langle J_\alpha^{(\mathrm{fl})}(\mathbf{r},\omega)J_\beta^{(\mathrm{fl})*}(\mathbf{r}',\omega')\right\rangle = 4\pi\omega\varepsilon_0\mathrm{Im}[\varepsilon(\omega)]\Theta(\omega,T)\delta(\mathbf{r}-\mathbf{r}')\delta(\omega-\omega')\delta_{\alpha\beta} \tag{2.6}$$

where $\Theta(\omega,T)$ is the mean energy of a Planck oscillator given by

$$\Theta(\omega,T) = \frac{\hbar\omega}{\exp\left(\frac{\hbar\omega}{k_BT}\right)-1} \tag{2.7}$$

Equation (2.6) is written in Cartesian index notation (used throughout this dissertation), where the Greek subscripts are indices 1,2,3 representing Cartesian vector components. Repeated subscript variables in a single term are summed, such that $A_\alpha B_\alpha = \mathbf{A}\cdot\mathbf{B}$ and $A_\alpha B_\beta = \mathbf{A}\otimes\mathbf{B}$. With the electromagnetic fields and currents specified, the total heat flux at location $\mathbf{r}$ in the time domain may be expressed by integrating the Poynting vector [25] over all frequencies:

$$\mathbf{S}(\mathbf{r},t) = \int_0^\infty \frac{d\omega}{2\pi^2}\mathrm{Re}[\langle\mathbf{E}(\mathbf{r},\omega)\times\mathbf{H}^*(\mathbf{r},\omega)\rangle] \tag{2.8}$$

Here the $1/\pi^2$ factor results from the convention used for the Fourier transform. A corresponding π^2 factor exists in the fluctuation-dissipation theorem that differs from other works using the $f(t) = \int_{-\infty}^{\infty} d\omega\, f(\omega)\mathrm{e}^{-i\omega t}$ convention [3]. Combining Equations (2.4), (2.5), (2.6), and (2.8) yields a final expression for the heat flux emitted by volume V' at location **r**:

$$S_\alpha(\mathbf{r},t) = \int_0^\infty \frac{2k_0^2}{\pi} \int_V \mathrm{Re}\{i\Theta(\mathbf{r}',\omega,T)\mathrm{Im}[\varepsilon(\mathbf{r}',\omega)] \cdot \epsilon_{\alpha\beta\gamma} G^E_{\beta\delta}(\mathbf{r},\mathbf{r}',\omega) G^{H*}_{\gamma\delta}(\mathbf{r},\mathbf{r}',\omega)\} dV' d\omega \tag{2.9}$$

where $\epsilon_{\alpha\beta\gamma}$ is the alternating unit tensor. If the temperature distribution, optical properties, and dyadic Green's functions are known, the problem is fully specified and the total heat transfer may be determined by evaluating $\mathbf{S}(\mathbf{r},t)$ appropriately; for instance, between two parallel plates the component normal to the surface provides the heat flux from one plate to the other. Computational NFRHT problems therefore mostly deal with the challenge of determining the dyadic Green's functions for the system.

2.1.2 Computational and Experimental Developments

A wide variety of computational approaches to NFRHT exist, including both analytical and numerical methods. Because of the challenges associated with determining system Green's functions for complex structures, exact solutions have only been developed for a few simple geometries. These include two parallel half spaces [1], two parallel films [26], one-dimensional layered media [27-29], a sphere and a surface [30], two spheres [31], two long cylinders [32], and a linear chain of spheres [33]. Of these exact solutions, only a

linear chain of spheres represents a case of many nanostructures. Approximate solutions have also been determined for two nanoporous films [34], a sphere and a structured surface [35], and systems of many nanoparticles [10]. Numerical methods may be applied more broadly and include the scattering matrix approach [36-40], the fluctuating surface current formalism [41, 42], the fluctuating volume current formalism [43], the finite-difference time-domain method [44-47], the Wiener chaos expansion approach [48, 49], and the thermal discrete dipole approximation (T-DDA) [50-53].

While NFRHT enhancement has been predicted theoretically for different conditions in many studies, experimental investigations have been comparatively limited due to difficulties in maintaining a nanoscale vacuum gap between parallel surfaces. There has been more success in measuring heat transfer between a probe tip and a surface or between two microscopic structures, and several researchers have done so for separation distances down to a few nanometers [54-67]. These investigations have largely confirmed the accuracy of FE down to separation distances of about 10 nm. Despite challenges associated with larger areas, notable progress has been made for parallel-plate configurations with lateral dimensions up to 1 cm at a few hundred nanometers separation [2, 68-74]. Even with this progress, very few applications of NFRHT have been demonstrated experimentally. A few notable exceptions are the recent confirmation of near-field power enhancement of thermophotovoltaic cells [75, 76] and demonstration of photonic cooling aided by NFRHT [77]. However, these demonstrations still relied on the use of nanopositioners and microdevices with small areas to obtain the nanoscale separation distances.

2.2 Non-Thermal Electromagnetic Coupling Between Nanostructures

Although thermal radiation between nanostructures is a relatively new field, classical electromagnetic scattering and coupling between particles or nanostructures has a much longer history of investigation [78, 79]. Much of the knowledge gained from prior studies may be adapted to thermal radiation, thus it is important to provide an overview of the relevant research on non-thermal electromagnetic interactions between nanostructures. The two most applicable topics are the fields of sub-diffractional waveguiding, which is heavily used in the KT formalism of thermal radiation, and the DDA, which provides the basis for FE approaches to many nanostructures.

2.2.1 Sub-Diffractional Waveguiding

SPs exist not only on the surface of planar materials; they are also present if those materials have nanoscale dimensions. When surface modes are spatially confined to structures such as nanopillars or nanoparticles they are considered "localized" SPhPs or SPPs, as illustrated in Figure 2.2. Coupling of these modes between many neighboring structures can lead to substantial energy transport. Due to the nanoscale dimensions of the materials and the SPs, this energy transport can take place at length scales far below the diffraction limit. For instance, nanoscale polaritonic particles may serve as sub-diffractional waveguides for nanophotonic devices when organized into extended one-dimensional arrays [80-89]. The ability to confine and transmit light at such small dimensions has important implications for photonic circuits [90], plasmonic sensing [91], and other optical applications.

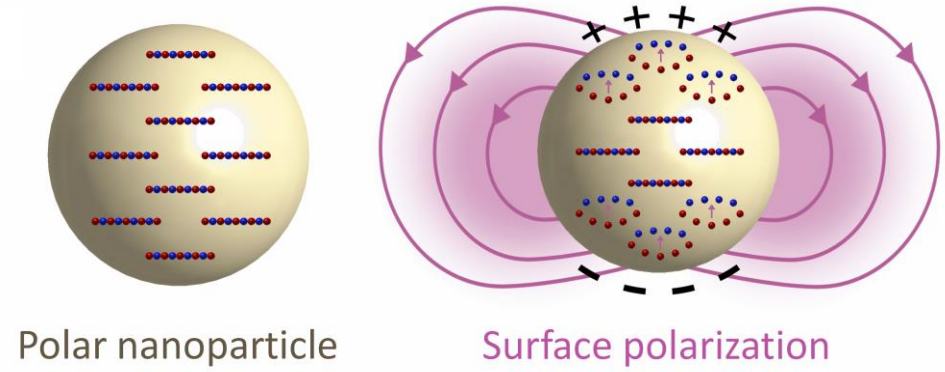

Figure 2.2. Illustration of nanoparticle with a localized surface phonon polariton resonance.

The ability of plasmonic particle chains to support sub-diffractional waveguiding was predicted by Quinten *et al.* in 1998 [80] and demonstrated experimentally by Maier *et al.* in 2003 [82]. These works initiated a wave of interest in energy transport along polaritonic particle chains that inspired many other researchers [81, 83-89]. The concept has been theoretically investigated by applying Maxwell's equations through the use of Mie theory [80], equations of motion for coupled dipole oscillation [81], and wave solutions to coupled electric field interactions [85] to name a few methods. A good review on the topic is available by Halas *et al.* [87]. In general, these methods calculate the dispersion relation for the propagating SP modes and then use the dispersion to predict mode propagation lengths and group velocities.

Early works in this area tended to use the quasi-static approximation for electric fields due to oscillating point dipoles when calculating the dispersion relation. Park and Stroud showed in 2004 that the dipolar approximation is only valid for spherical particles when the separation distance is approximately greater than or equal to the particle radius

[83], which has been confirmed with calculations by other researchers examining radiative heat transfer [31, 92]. This places an important constraint on spacing when considering arrays of nanostructures. The quasi-static approximation was shown to be overly simplistic for chains of metal nanoparticles by Weber and Ford in 2004; instead, the effects of retardation and radiation damping must be included [84]. Considering these effects, the dispersion relation for a chain of infinite particles modeled as point dipoles may be written as [85, 86]

$$0 = 1 + \frac{\alpha^{(\mathrm{d})}}{2\pi\varepsilon_m d^3}\sum_{j=1}^{\infty}\left[\left(1 - i\frac{\omega d\sqrt{\varepsilon_m}}{c}j\right)\frac{1}{j^3} - \frac{\omega^2 d^2 \varepsilon_m}{c^2}\frac{1}{j}\right]\cos(jkd)\, e^{i\omega j d\sqrt{\varepsilon_m}/c} \tag{2.10}$$

for the transverse modes and

$$0 = 1 - \frac{\alpha^{(\mathrm{d})}}{\pi\varepsilon_m d^3}\sum_{j=1}^{\infty}\left[\left(1 - i\frac{\omega d\sqrt{\varepsilon_m}}{c}j\right)\frac{1}{j^3}\right]\cos(jkd)\, e^{i\omega j d\sqrt{\varepsilon_m}/c} \tag{2.11}$$

for the longitudinal mode, where $\alpha^{(\mathrm{d})}$ is the dressed nanoparticle polarizability [78], ε_m is the relative permittivity of the surrounding medium, d is the center-to-center particle spacing, and k is the wavevector. To account for losses, either ω or k must be taken as a complex quantity. If ω is complex, its imaginary part is related to the mode lifetime, and if k is complex, its imaginary part is related to the propagation length. The dispersion relation may be solved numerically for both transverse and longitudinal modes with known geometry and material properties by re-writing Equations (2.10) and (2.11) in

polylogarithm form [85]. From the dispersion relation, the group velocity $v_g = \mathrm{Re}(\partial\omega/\partial k)$ and the energy propagation length $\Lambda = [2\mathrm{Im}(k)]^{-1}$ or $\Lambda = |v_g|[-2\mathrm{Im}(\omega)]^{-1}$ (amplitude propagation length $\Lambda_a = 2\Lambda$) [85] may be extracted and used to characterize waveguide performance.

2.2.2 Discrete Dipole Approximation

When light strikes a collection of small particles, the energy absorbed and scattered depends on electromagnetic interactions between all particles in the group [78, 79]. This is true regardless of whether the particles support SPs. In 1973, Purcell and Pennypacker [93] recognized an arbitrary body may also be approximated by an assembly of small particles or dipoles, and they introduced the DDA. The interactions between all dipoles may be expressed as a system of linear equations and solved in order to obtain the absorption and scattering properties of the body or collection of particles [94].

The DDA became widely used after it was further developed [95-98] and distributed as the publicly available software DDSCAT [99] by Draine *et al*. In addition to being formulated in terms of an assembly of point dipoles, the DDA may also be derived from the volume integral equation for the electric field [100-103], although this approach is mathematically equivalent [101, 104]. Two of the most common formulations of the DDA are the coupled dipole method [105] and the method of moments [106]. For both approaches, a body is replaced by an assembly of point dipoles. They differ, however, in the treatment of the dipoles' relation to the electric field. In the coupled dipole method, each dipole moment is expressed in terms of the *exciting* field from an external source and all other dipole moments. In the method of moments, each dipole moment is expressed in terms of the *actual* field from an external source and all dipole moments including its own dipole moment. The distinction is purely mathematical, and the two approaches were

shown to be equivalent by Lakhtakia and Mulholland [107]. This difference will prove to be important, though, when it is applied to thermal radiation in particles or discretized bodies.

The most commonly used form of the DDA is the coupled dipole method, and its conceptual framework is relatively straightforward. An external electric field $\mathbf{E}^{(\mathrm{inc})}(\mathbf{r},\omega)$ is incident on the scattering objects, which are approximated by a collection of N volumes modeled as electric point dipoles $\mathbf{p}(\mathbf{r},\omega)$. The dipole moments are related to the exciting electric fields (external field plus fields from all other dipoles) by the dressed polarizability. In this framework, a self-consistent set of linear equations may be written for each subvolume i as [97]

$$\mathbf{p}(\mathbf{r}_i,\omega) = \varepsilon_0 \alpha^{(\mathrm{d})}(\mathbf{r}_i,\omega)\left[\mathbf{E}^{(\mathrm{inc})}(\mathbf{r}_i,\omega) + \frac{k^2}{\varepsilon_m \varepsilon_0}\sum_{j\neq i}\mathbb{G}^{(0)}\left(\mathbf{r}_i,\mathbf{r}_j,\omega\right)\cdot\mathbf{p}\left(\mathbf{r}_j,\omega\right)\right] \tag{2.12}$$

$\mathbb{G}^{(0)}\left(\mathbf{r}_i,\mathbf{r}_j,\omega\right)$ is the electric dyadic Green's function for the background medium given by

$$\mathbb{G}^{(0)}\left(\mathbf{r}_i,\mathbf{r}_j,\omega\right) = \frac{\mathrm{e}^{ikR}}{4\pi R}\left[\left(1+\frac{ikR-1}{k^2R^2}\right)\mathbb{I} + \frac{3(1-ikR)-k^2R^2}{k^2R^2}\widehat{\mathbf{R}}\otimes\widehat{\mathbf{R}}\right] \tag{2.13}$$

where $\mathbb{I}$ is the identity matrix, $\mathbf{R} = \mathbf{r}_i - \mathbf{r}_j$, $R = |\mathbf{R}|$, and $\widehat{\mathbf{R}} = \mathbf{R}/R$. Equation (2.12) may be re-written in terms of an interaction matrix $\mathbb{A}$ as

$$\mathbb{A}^{(\mathrm{DDA})}\begin{pmatrix}\mathbf{p}(\mathbf{r}_1,\omega)\\ \vdots \\ \mathbf{p}(\mathbf{r}_N,\omega)\end{pmatrix}=\begin{pmatrix}\mathbf{E}^{(\mathrm{inc})}(\mathbf{r}_1,\omega)\\ \vdots \\ \mathbf{E}^{(\mathrm{inc})}(\mathbf{r}_N,\omega)\end{pmatrix} \tag{2.14}$$

where $\mathbb{A}^{(\mathrm{DDA})}$ is a $3N\times3N$ matrix with N^2 3×3 submatrices $\mathbb{A}_{ij}^{(\mathrm{DDA})}$ defined by

$$\mathbb{A}_{ij}^{(\mathrm{DDA})}=\begin{cases}\left[\varepsilon_0\alpha^{(\mathrm{d})}(\mathbf{r}_i,\omega)\right]^{-1}, & i=j\\ -\dfrac{k^2}{\varepsilon_m\varepsilon_0}\mathbb{G}^{(0)}\left(\mathbf{r}_i,\mathbf{r}_j,\omega\right), & i\neq j\end{cases} \tag{2.15}$$

A major benefit of Equation (2.14) is its form of $\mathbb{A}\cdot\mathbf{x}=\mathbf{b}$ with unknown $\mathbf{x}$, which permits iterative numerical solutions instead of directly solving for $\mathbf{x}$ by inverting $\mathbb{A}$ [94]. This allows systems of many thousands of subvolumes to be analyzed quickly with common desktop computers or very complex systems to be analyzed efficiently with high performance computing resources.

2.3 Thermal Radiation Among Many Nanostructures

While classical light scattering from small particles has a long history of study and is relatively well understood, thermal radiation in such systems has only been explored since the early 2000s [92, 108], particularly for objects which support SPs. Despite the field's recent history, significant progress includes the development of kinetic theories for arrays of plasmonic resonators [92, 108-113], exact many-body theories for collections of small particles [33, 53, 114-122], and the T-DDA for arbitrary bodies [50-53].

2.3.1 Kinetic Theory

Kinetic approaches to calculating thermal transport, often based on the Boltzmann transport equation, have been widely used to predict heat transfer by phonons and electrons

in a variety of materials and structures. Under the relaxation time approximation and the condition of local equilibrium, the Boltzmann transport equation describes heat flux in terms of the energy carriers' temperature, population statistics, velocity, and relaxation time [8]. If the complex dispersion relation for the energy carriers is known, this provides the velocities and relaxation times, allowing heat transfer characteristics to be calculated in a straightforward manner. A kinetic approach to thermal transport by SPs is therefore a natural extension to the field of sub-diffractional waveguiding discussed in Section 2.2.1.

Kinetic theory was first used to investigate the radiative thermal conductivity of nanoparticle chains by Ben-Abdallah and co-workers in the early 2000s [92, 108]. They analytically examined high temperature metallic particles at varying separation distances. For copper particles 20 nm in diameter at 900 K, they found that multipolar interactions result in radiative thermal conductivities up to about 0.1 W m^{-1} K^{-1} when the particles are in contact [92]. Ordonez-Miranda *et al.* later examined polar nanoparticles of varying shape at more moderate temperatures in the dipole limit [109-111], showing that prolate SiC spheroids with 50 nm minor axis diameter at 700 K in contact have a radiative thermal conductivity of 0.05 W m^{-1} K^{-1}. Ramirez and McGaughey examined a different type of system consisting of repeated disks of doped graphene near room temperature and found that the radiative thermal conductivities can be much higher, up to 4.5 W m^{-1} K^{-1} for 500 nm disks that are 50 nm apart at 300 K [112]. There are limitations to each of these systems and approaches, though. The radiative transport in nanoparticle chains is restricted due to inherent losses for metal-based SPPs [123] and strong dispersions (corresponding to low group velocities) for SPhPs in polar dielectrics [22]. The SPP resonance for metallic particles is also typically at high energies in the visible or ultraviolet regions, meaning that

very high temperatures are required to excite those modes. These factors reduce the thermal conductivities of particle chain systems and require optimized particle shapes to maximize heat transfer [111] which may be difficult to assemble in practical systems. The graphene disk system proposed by Ramirez and McGaughey may be able to address some of these limitations through good carrier mobility and lower SPP resonance energies [112], but it still could be challenging to fabricate the disks and maintain their positions.

Regardless of the material system under examination, the radiative thermal conductivity in the diffusive limit (propagation lengths are much less than the length of the system) may be calculated directly from the complex dispersion relation. The thermal conductivity for a chain of nanostructures supporting SPs may be derived from the Boltzmann transport equation and is [109, 124]

$$\kappa = \frac{1}{\pi A_c} \int_{\omega_{min}}^{\omega_{max}} \hbar\omega (2\Lambda_\perp + \Lambda_\parallel) \frac{\partial f^{(\mathrm{BE})}(\omega, T)}{\partial T} d\omega \tag{2.16}$$

where A_c is the cross-sectional area, ω_{min} and ω_{max} represent the bounds of the frequencies where SPs are supported, $\Lambda_\perp$ and $\Lambda_\parallel$ are respectively the propagation lengths for the transverse and longitudinal modes, and $f^{(\mathrm{BE})}(\omega, T)$ is the Bose-Einstein distribution function. The dispersion provides the frequencies and associated propagation lengths for the transverse and longitudinal modes as discussed in Section 2.2.1, allowing the calculation of thermal conductivity. The transverse propagation length is multiplied by two because there are two degenerate modes transverse to the chain axis in isotropic surroundings. The integration is performed over the frequencies where propagating SPs are supported, which is given by the dispersion relation. For SPhPs these will be within the

Reststrahlen band between the transverse optical and longitudinal optical phonon frequencies, and for SPPs these will be below the plasma frequency [22].

Equation (2.16) has some limitations and challenges associated with its use that are important to note. First, a kinetic approach only describes transport by the modes given in the dispersion relation. In this case, that is only the propagating SP modes. This formalism therefore does not include radiative transport by interactions other than SPs, such as propagating photons or frustrated mode interactions. These other modes can be dominant in materials with weak or no SP interactions, materials with other types of resonant interactions (e.g. magnetic), or materials whose SP resonance is at much higher energy than the $k_B T$ thermal energy. Second, Equation (2.16) requires a known dispersion relation, but this can be challenging to determine. For point dipoles in a homogeneous environment, the dispersion is known analytically and is given by Equations (2.10) and (2.11). For more complex geometries or environments, however, the dispersion may not be determined analytically. In these cases indirect numerical methods may need to be employed, such as tracking optical pulse propagation in finite-difference time-domain simulations [125]. For optimization problems or the design of new material systems, such numerical approaches may be computationally burdensome and difficult to compare to experiments.

2.3.2 Fluctuational Electrodynamics

The framework of FE described in Section 2.1.1 can, in principle, be applied to systems of many nanostructures to obtain exact solutions for the NFRHT. However, due to the difficulty in determining system Green's functions for complex geometries, this has only been achieved very recently by Czapla and Narayanaswamy for a linear chain of

spheres [33]. Their solution is based on numerically exact vector spherical wave expansions of the dyadic Green's functions. Other shapes and arrangements of many nanostructures do not yet have exact solutions, but some assumptions and approximations may be made to analyze them.

The most common and arguably most powerful simplification of a system of many nanostructures is to assume each structure may be modeled as a point dipole. This requires that the electric field and dyadic Green's function are constant throughout the volume of the structure, which in practice means that its size must be much smaller than the wavelengths and decay lengths of the electric fields [51]. As discussed in Section 2.2.1, it also requires that the separation distance between any two structures be approximately greater than their effective radius. When these conditions are met, the problem becomes greatly simplified because the electric field due to a point dipole in a homogeneous medium is simply described with the dyadic Green's function given by Equation (2.13). The situation is also then very similar to that analyzed with the DDA, except that thermal effects must also be considered.

Integrating thermal sources into the DDA formalism applied to many particles was first done by Ben-Abdallah *et al*. in 2011 [114], and the theory was further refined by Messina *et al.* in 2013 [115]. These works considered isotropic spherical nanoparticles suspended in vacuum, and the latter study also included the fields from an external bath. They showed that systems containing more than two particles depend strongly on the geometric configuration of all particles and can exhibit enhanced radiative heat transfer due to many-body effects. Since then, the theory has been extended and adapted to examine anisotropic particles [117], magnetic polarization [53, 119], core-shell particles [121], and

point multipoles [122]. This many-body theory has been used to predict a variety of interesting and potentially useful effects including heat superdiffusion in systems of plasmonic particles [126] and several magneto-optical phenomena [10, 127-129] such as a thermal Hall effect [127]. In parallel to this many-body formalism, the T-DDA was developed by Edalatpour and Francoeur in 2014 [50] and later refined [51-53] for arbitrary bodies discretized into subvolumes modeled as point dipoles (analogous to the DDA). The T-DDA is a promising technique due to its applicability to materials and geometries that may be difficult to examine via other methods; for instance, it has been used to understand spectral redshifts in near-field thermal spectroscopy [130].

Both the many-body method and the T-DDA share a common conceptual framework. Instead of an incident external electric field acting as a primary source term, thermal fluctuations of the dipole moments are the source of emitted electromagnetic fields. These are incorporated into the system by splitting each dipole moment into a part due to thermal fluctuations and a part induced by the electric fields:

$$\mathbf{p}_i = \mathbf{p}_i^{(\mathrm{fl})} + \mathbf{p}_i^{(\mathrm{ind})} \tag{2.17}$$

The induced part can be written in terms of the particle polarizability and electric field similar to Equation (2.12) in the DDA formalism, and the spatial correlation function for the fluctuating part can be determined from the fluctuation-dissipation theorem. This allows an interaction matrix to be specified which contains information about electromagnetic interactions between all particles, similar to Equation (2.14) in the DDA. In the many-body method, the final equation for the net heat transfer to the ith particle in the time domain is [115]

$$
\begin{aligned}
&Q_i(t, T_1, \ldots, T_N) \\
&= \int_0^\infty \frac{d\omega}{2\pi} \hbar\omega \left[\sum_{j \neq i} \frac{4\chi_i \chi_j}{\left|\alpha_i^{(\mathrm{d})}\right|^2} f_{ji}^{(\mathrm{BE})}(\omega) \mathrm{Tr}\left(\mathbb{A}_{ij}^{(\mathrm{MB})^{-1}} \mathbb{A}_{ij}^{(\mathrm{MB})^{-1\dagger}} \right) \right. \\
&\left. + \frac{4k^2 \chi_i}{\left|\alpha_i^{(\mathrm{d})}\right|^2} f_{\mathrm{b}i}^{(\mathrm{BE})}(\omega) \sum_{jk} \alpha_j^{(\mathrm{d})} \alpha_k^{(\mathrm{d})^*} \mathrm{Tr}\left(\mathbb{A}_{ij}^{(\mathrm{MB})^{-1}} \mathrm{Im}\left(\mathbb{G}_{jk}^{(0)} \right) \mathbb{A}_{ki}^{(\mathrm{MB})^{-1\dagger}} \right) \right]
\end{aligned}
\tag{2.18}
$$

where $f_{ji}^{(\mathrm{BE})}(\omega) = f^{(\mathrm{BE})}\left(\omega, T_j\right) - f^{(\mathrm{BE})}(\omega, T_i)$, $f_{\mathrm{b}i}^{(\mathrm{BE})}(\omega)$ is similar except the subscript b represents the thermal bath, $\mathbb{A}_{ij}^{(\mathrm{MB})^{-1}}$ is a 3×3 submatrix of the inverted interaction matrix, and χ_i is a reduced absorption factor given by [115]

$$
\chi_i = \mathrm{Im}\left(\alpha_i^{(\mathrm{d})}\right) - \frac{k^3}{6\pi\varepsilon_m} \left|\alpha_i^{(\mathrm{d})}\right|^2 \tag{2.19}
$$

In the T-DDA, the final equation for the net heat transfer to the ith subvolume in the frequency domain is [50, 51]

$$
\begin{aligned}
Q_i(\omega, T_1, \ldots, T_N) = \frac{\omega}{2} \sum_i &\left[\mathrm{Im}\left(\alpha_i^{(\mathrm{d})^{-1*}} \right) - \frac{2}{3} k_0^3 \right] \\
&\cdot \mathrm{Tr}\left[\left(\mathbb{A}^{(\mathrm{TDDA})^{-1}} \cdot \mathbb{R} \cdot \mathbb{A}^{(\mathrm{TDDA})^{-1\dagger}} \right)_{ii} \right]
\end{aligned}
\tag{2.20}
$$

where $\mathbb{A}^{(\mathrm{TDDA})^{-1}}$ is the inverted interaction matrix and $\mathbb{R}$ is a correlation matrix for an incident electric field.

Equation (2.18) for the many-body method and Equation (2.20) for the T-DDA are not the same, and their interaction matrices are also different from each other, despite the

fact that they share a conceptual framework. This is a result of differing formulations; the many-body method uses an *exciting* field formalism analogous to the coupled dipole method in the DDA, and the T-DDA uses an *actual* field formalism analogous to the method of moments in the DDA. They also use different forms of the fluctuation-dissipation theorem. Because of these dissimilarities, it is not clear whether the many-body method and the T-DDA are mathematically equivalent or what advantages one approach may have over the other.

Both formalisms share some limitations, however. Unlike the DDA, which may be expressed in the form $\mathbb{A}^{(\mathrm{DDA})} \cdot \mathbf{x} = \mathbf{b}$ and numerically solved for $\mathbf{x}$, the many-body method and the T-DDA require the inversion of their interaction matrices as shown in Equations (2.18) and (2.20). This is a computationally intensive process both in terms of execution time (order of $27N^3$ operations) and memory requirements (proportional to $9N^2$) because of the need to store and invert $\mathbb{A}$. This significantly limits the number of particles or subvolumes that can be examined, even with high performance computing resources. Another limitation of these methods is that they give the net heat transfer absorbed by a single particle or subvolume, which is why radiative thermal conductivities have not been reported with these methods for particle arrays like they have with KT approaches. For many systems, especially systems of many particles, absorption by an individual particle is not very useful when comparing radiative heat transfer to other modes of thermal transport, such as conduction by phonons or electrons.

2.4 Research Objectives

Although researchers have made a great deal of progress in understanding and modeling NFRHT among many nanostructures, practical applications of these concepts remain elusive. As discussed in the previous sections, this is due to material limitations in the systems previously considered, inflexible modeling approaches with respect to geometry and environment, mixed theoretical techniques in describing the radiation exchange, and computational restrictions for large numbers of nanostructures. To address these limitations, this dissertation aims to provide generally applicable tools to analyze NFRHT among nanostructures and provide initial predictions and measurements of NFRHT in various nanostructure arrays by achieving the following objectives:

1. Experimentally analyze systems of many polaritonic nanostructures to investigate whether thermal radiation is a significant contributor to total thermal transport.
2. Study radiative energy transport by propagating modes in environments that have not been previously analyzed, such as anisotropic and nonhomogeneous surroundings.
3. Predict and understand thermal radiation in ordered and disordered nanoparticle arrays with a variety of separation distances.

CHAPTER 3. PACKED NANOPARTICLE EXPERIMENTS

Although a number of researchers have analytically examined NFRHT between nanoparticles as described in the previous chapter, there have been no reports of a measured contribution by NFRHT to thermal transport among many nanoparticles. A model system to experimentally resolve NFRHT mediated by SPhPs is a packed polar nanoparticle bed, illustrated in Figure 3.1, for three primary reasons. First, the phonon thermal conductivity of a nanoparticle bed is dictated by high thermal boundary resistance at numerous contacts [9], which produces extremely low phonon thermal conductivity near room temperature (~0.05 W m^{-1} K^{-1}). Second, this system allows modification of the interstitial material between nanoparticles or coating of the nanoparticles to investigate effects of the medium on SPhPs. Third, packed nanoparticles can be approximated as three-dimensional nanoparticle crystals [131] for a theoretical development that is analogous to three-dimensional phonon transport in an atomic crystal.

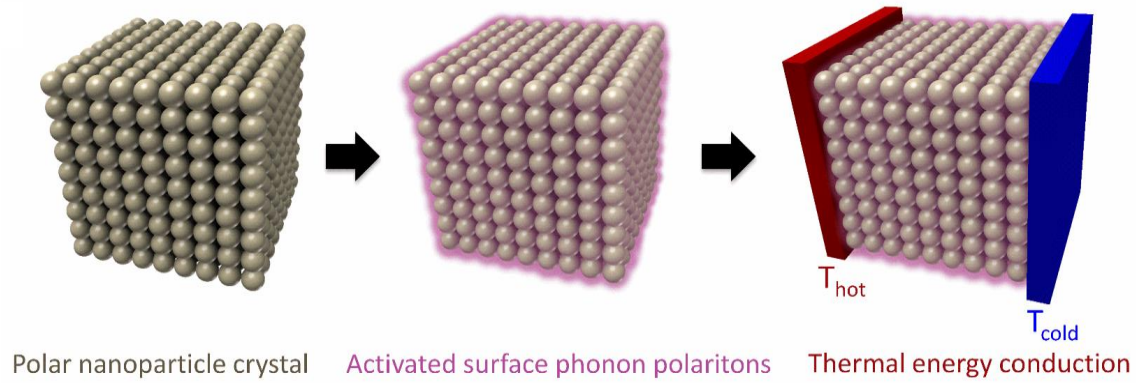

Figure 3.1. Near-field radiative heat transfer mediated by surface phonon polaritons in a packed nanoparticle bed.

This chapter describes experimental investigations of packed SiO_2 nanoparticles (also presented in reference [132]). When the interstitial medium is changed from dry air to humid air or ethylene glycol, measured thermal conductivities are as high as 1.5 and 18 times the phonon value, respectively. Existing NFRHT models do not fully explain the results, but a new scaling relation is developed that suggests a strong dependence on the density of states. An examination of other heat transfer mechanisms shows that these are unlikely sources for the observed thermal conductivities, suggesting that NFRHT mediated by SPhPs plays an observable role in SiO_2 nanoparticle bed heat transfer properties.

3.1 Spectroscopic Evidence for Surface Polaritons

To show that SPhPs are active in this system, Fourier transform infrared attenuated total reflection (FTIR-ATR) measurements are performed on 10-20 nm and 60-70 nm diameter packed SiO_2 nanoparticle beds, and the results are shown in Figure 3.2. The methods are described in detail in Appendix A.1.

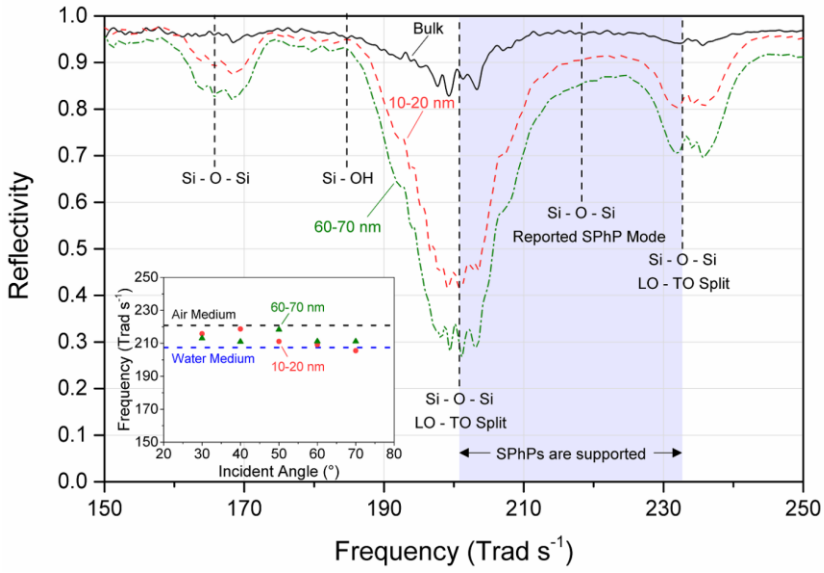

Figure 3.2. FTIR-ATR measurements of SiO_2 packed particles and a bulk film at an incident angle of 70° and fitted Gaussian peak locations (inset).

Any crystal lattice vibration that is sustained by mid-infrared light can be observed as minima, or 'dips', in the FTIR-ATR spectrum. Observation of a SPhP resonance localized to a metal tip near a SiO_2 sample [133] has shown the resonance frequency, ω_{SPhP}, to be in agreement with theory that predicts a SPhP resonance will be observed in the frequency range between the transverse optical (TO) and longitudinal optical (LO) phonon frequencies $\omega_{TO} < \omega_{SPhP} < \omega_{LO}$. The transverse-polarized FTIR-ATR spectroscopy analysis of the nanoparticle bed shows dips in the spectrum that agree, not only with expected values of the second resonance ω_{TO} and ω_{LO} for SiO_2 [134-136], but for all expected surface vibrations [137] in a system comprised of an SiO_2 interface coated with an atomic-scale thick layer of water [138]. To resolve the SPhP resonance dip that overlaps the two broad optical phonon dips, Gaussian curves are fit to the spectrum assuming five dips that correspond to the known surface vibrations within the region examined. The

Gaussian determined ω_{SPhP} (Figure 3.2 inset) is consistent with recent experiments [133] and the expected Fröhlich resonance frequency for localized surface modes [139].

3.2 Thermal Conductivity Measurements

3.2.1 Humid Air Interstitial Medium

A standard commercial technique using a Hot Disk measurement system is used to measure temperature dependent thermal conductivity of SiO_2 packed nanoparticle beds. Details of the experimental methods are presented in Appendix A.1. Two different methods of varying interstitial material or coating are used: adsorption of water in a humid environment and coating with ethylene glycol. The as-received SiO_2 nanoparticles contain significant amounts of adsorbed -OH species (evidenced by the FTIR-ATR results in Figure 3.2), indicating the presence of adsorbed water [138]. In the first method, the samples are dried and measured in an environmental chamber to remove surface water and control its return, and the results are shown in Figure 3.3.

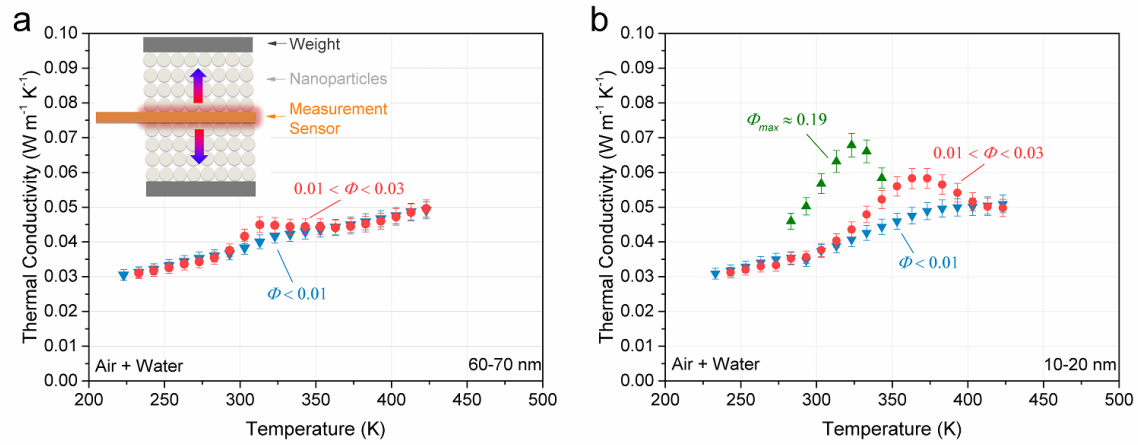

Figure 3.3. Thermal conductivity of (a) 60-70 nm and (b) 10-20 nm diameter SiO_2 particle beds in an air environment with various humidity ratios.

Samples tested in a dry environment (humidity ratio Φ less than 1.0%$\pm$0.3%) show measured thermal conductivities with a linear trend from about 0.03 to 0.05 W m^{-1} K^{-1} from $-$50 °C to 150 °C for both 10-20 and 60-70 nm diameter particles. These values are consistent with prior measurements [140] of small diameter packed nanoparticle beds where heat conduction is dominated by thermal boundary resistance [9], and they do not give any indication of thermal conduction by SPhPs. However, when the humidity in the chamber is allowed to rise as temperature is increased (measured humidity ratios between 1.0% and 3.0%$\pm$0.3%), leading to water adsorption on the nanoparticle surfaces [138], measured thermal conductivities depart from the linear trend and rise to approximately 1.21 (1.13) times the phonon value for the 10-20 (60-70) nm particles. These results are confirmed from at least three reproduced experiments (see Appendix A.2). Continued temperature increase then drives the water from the nanoparticle surfaces, and thermal conductivities return to the measured phonon values. When the same tests are performed for Si nanoparticles (see Appendix A.3), no increase in thermal conductivity above the linear phonon trend is observed, suggesting that adsorbed water does not contribute to other modes of heat transfer (additional discussion on this topic is provided in Section 3.2.3). The effect of adsorbed water contributing to SPhP thermal conductivity is tested further by placing a dish of water in the environmental chamber during a test of the 10-20 nm particles to increase the humidity, resulting in humidity ratios up to 18.7%$\pm$2.7%. In this case, measured thermal conductivities are as high as 1.51 times the phonon value as shown in Figure 3.3(b). Measured specific heats (see Appendix A.4) show trends with adsorbed water that are similar to the thermal conductivity data, indicating that SPhPs may increase specific heat in addition to the contributions from the adsorbed water.

3.2.2 Ethylene Glycol Interstitial Medium

In the second modification technique, the as-received nanoparticles are coated with ethylene glycol through a solution chemistry process described in Appendix A.1. The measured thermal conductivities are shown in Figure 3.4. The particles in Figure 3.4(a) were solution processed with approximately 50% water by volume, which was removed by baking after processing. The particles in Figure 3.4(b) were solution processed in pure ethylene glycol.

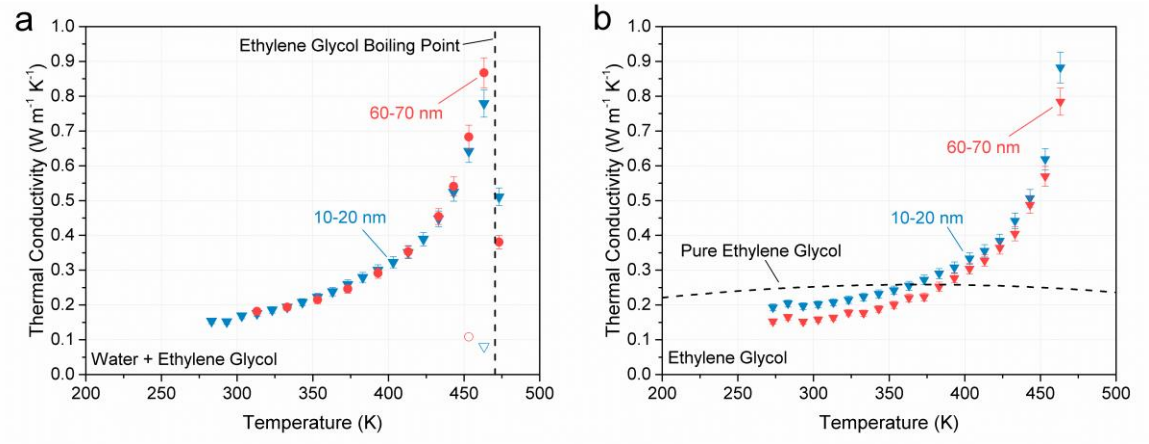

Figure 3.4. Thermal conductivity of SiO_2 particle beds coated with ethylene glycol prepared in (a) a water/glycol solution and (b) pure ethylene glycol.

The measured thermal conductivity from 0 to 200 °C shows a dramatic increase from approximately 0.15 W m^{-1} K^{-1} to greater than 0.8 W m^{-1} K^{-1} for both the 10-20 and 60-70 nm coated particles. In every test, the thermal conductivity drops sharply from its maximum value to less than 0.1 W m^{-1} K^{-1} at 190 or 200 °C, indicating loss of ethylene glycol (boiling point ~197 °C). The open symbols in Figure 3.4(a) are data taken after the maximum temperature is reached to show that the thermal conductivity is low after ethylene glycol is lost. The maximum measured thermal conductivity varies with the

specific sample but is typically near 0.8 W m^{-1} K^{-1} for both the 10-20 and 60-70 nm particles, representing a thermal conductivity of up to 18 times the measured phonon value and more than 3.5 times the thermal conductivity of pure ethylene glycol [141]. The thermal conductivity of pure ethylene glycol is shown in Figure 3.4(b) for comparison.

3.2.3 Other Heat Transfer Mechanisms

To have confidence that the high measured thermal conductivities are attributable to SPhP activity, it is important to consider the possible influence of other heat transfer mechanisms for both the ethylene glycol coated and adsorbed water nanoparticle beds. For the ethylene glycol coated nanoparticles, the maximum thermal conductivity is more than 3.5 times the bulk value of ethylene glycol. If the interstitial medium were primarily responsible for the enhancements to thermal conductivity, the measurements should not exceed the thermal conductivity of the bulk medium. To show that phase-change of the ethylene glycol is not responsible for the increases in thermal conductivity, additional tests are performed on 50-70 nm Si nanoparticles coated with ethylene glycol, processed under the same procedure as the SiO_2 nanoparticles (see Appendix A.1 for methods). The results, shown in Figure 3.5, demonstrate that although ethylene glycol is present (as indicated by the higher thermal conductivities than those seen for dry Si nanoparticle beds in Appendix A.3), there is no significant enhancement similar to that observed with SiO_2 nanoparticle beds.

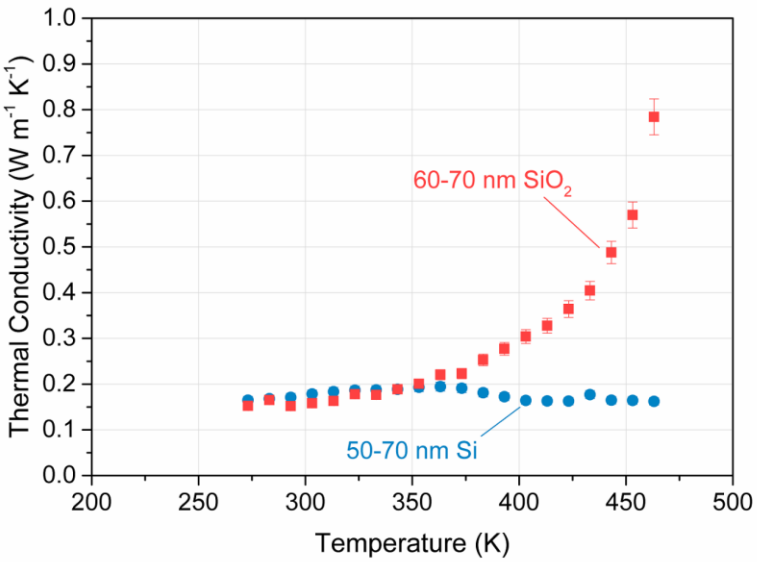

Figure 3.5. Measured thermal conductivity of packed Si nanoparticles for comparison to the results for SiO_2.

To further show that there is no influence of phase change on the thermal conductivity measurements, and to demonstrate that the Hot Disk measurement system can appropriately distinguish between thermal conductivity and specific heat measurements, the measured volumetric specific heat by the Hot Disk is compared with the measured specific heat by differential scanning calorimetry (DSC). The results for 60-70 nm SiO_2 coated with ethylene glycol are shown in Figure 3.6. A linear relationship is seen for both test methods until the loss of ethylene glycol near its boiling point, which is seen in the DSC trace as a sharp increase. The linear trend up to the boiling point is additional evidence that phase change is not dominating the heat transfer properties of the ethylene glycol coated samples, and it gives confidence in the Hot Disk results. Different samples prepared by the same process were used for the two measurements, which is why the ethylene glycol boils at slightly different temperatures.

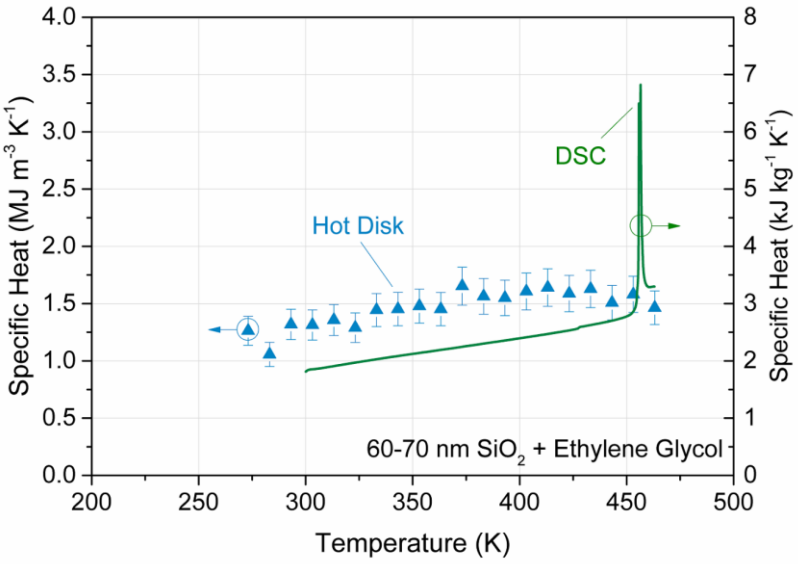

Figure 3.6. Measured specific heat of SiO_2 particles coated with ethylene glycol by the Hot Disk and by differential scanning calorimetry.

For the case of adsorbed water, a comparison can be made to Si nanoparticles. The specific heat of Si nanoparticles, which do not support SPhPs, of similar diameter to the SiO_2 nanoparticles is tested and is shown in Appendix A.5. The peaks indicate the presence of adsorbed water increasing the specific heat. However, the thermal conductivity data for these Si nanoparticles (see Appendix A.3) do not show any corresponding increase. This is strong evidence that adsorbed water only substantially contributes to thermal conduction by SPhPs and not to other modes of heat transfer.

Additionally, the very large internal surface area of packed nanoparticle beds confines adsorbed water to atomic-scale thick layers. The volume of water in the matrix or surrounding medium in a packed spherical nanoparticle bed is $4a^3(2-\pi/3)\cdot\Phi$, where Φ is the percent of water in the air and a is the nanoparticle radius. $4\pi a^2 x$ is the volume of water adsorbed on the nanoparticles, where x is the thickness of the adsorbed layer. Setting the two expressions equal results in $\Phi = x/a\cdot(2/\pi - 1/3)^{-1}$. It is difficult to know the

exact amount of water in the nanoparticle bed in each test, but this expression is useful for understanding an approximation of water coverage on the nanoparticle surfaces in each specific case. For example, if the humidity ratio in between the 10-20 nm particles were 1, this would still only result in a water layer approximately 0.005 nm thick. Therefore, this nanoparticle radius will likely always have a mixture of air and water at the particle-matrix interface. This result also supports the fact that the adsorbed water layers are too thin to substantially contribute to heat conduction directly. For example, to support even a 2 nm coating on all surfaces in a 60-70 nm packed nanoparticle bed, more than 10% of the matrix volume must be water. Smaller diameter nanoparticles, which have a much larger total surface area in a packed bed of the same volume, would require even higher amounts of water. As discussed in Appendix A.1, dry air at 150 °C is blown through the chamber for at least 1 hour to dry the nanoparticles and chamber before testing. Because water re-enters the system only through slow leaks in the test chamber, this makes high concentrations of water in the chamber difficult to produce. Additionally, the measured humidity ratio is less than 3% during the typical temperature increase cycle under these test conditions.

Finally, the measured thermal conductivities for the packed SiO_2 nanoparticle beds (Figure 3.3) at room temperature (0.04-0.05 W m^{-1} K^{-1}) are an order of magnitude lower than that of water (~0.6 W m^{-1} K^{-1}) and similar to the thermal conductivities of typical SiO_2 aerogels [142] (note that the density of SiO_2 in the packed nanoparticle beds is likely higher than that in SiO_2 aerogels, but the weak van der Waals bonds at the nanoparticle contacts produce a more dominate role of thermal boundary resistance [9, 140] in this system). These results further support that there is likely no significant direct role for water in the phonon heat conduction. Taken together, the combination of these factors make it unlikely

that other heat transfer mechanisms can explain the high thermal conductivities seen in Figure 3.3.

3.3 Comparison to Models

3.3.1 Existing Models

In an attempt to understand the physics behind these results, two existing models for NFRHT by SPhPs are applied to this system. In the first model, the KT approach described in Section 2.3.1, a SPhP dispersion relation is calculated by looking for wave solutions to the electric field interactions between nanoparticles in a linear chain. The mode lifetimes and group velocities are then used to relate wave propagation to the SPhP thermal conductivity. The dispersion relations given in Equations (2.10) and (2.11) are solved using several simplifications. The Clausius-Mossotti equation for the nanoparticle polarizability is used, which does not correct for radiation damping but should provide good results for small particles [143]:

$$\alpha^{(\mathrm{CM})} = 3\varepsilon_m V \frac{\varepsilon - \varepsilon_m}{\varepsilon + 2\varepsilon_m} \tag{3.1}$$

The optical properties used for SiO_2 are based on a Lorentz model [8]

$$\varepsilon(\omega) = \varepsilon_\infty \left(1 + \frac{\omega_{LO}^2 - \omega_{TO}^2}{\omega_{TO}^2 - \omega^2 - i\omega\Gamma}\right) \tag{3.2}$$

where ε_∞ is the relative permittivity at infinite frequency, Γ is the damping coefficient or scattering rate, and ω_{TO} and ω_{LO} are the resonance frequencies of transverse optical and

longitudinal optical phonons, respectively. These properties for SiO_2 ($\varepsilon_\infty = 2$, second resonance Γ = 8.92 Trad s^{-1}, ω_{TO} = 207 Trad s^{-1}, and ω_{LO} = 234 Trad s^{-1}) are obtained by fitting to experimental data [144]. A constant $B_0 = \gamma_i a^3/(\varepsilon_m d^3)$ is introduced, where γ_i is a polarization-dependent constant with $\gamma_T = 1$ for the transverse case and $\gamma_L = -2$ for the longitudinal case. Inserting these equations into the dispersion relations and simplifying for the lossless quasi-static case [84], where $\Gamma \to 0$ and $c \to \infty$, yields after some algebraic manipulation the SPhP dispersion relation below. Calculations show (see Appendix A.6) that contributions above $j = 5$ nanoparticles are negligible in the dispersion relation.

$$\omega^2 = \frac{\begin{array}{c} B_0[\varepsilon_\infty \omega_{LO}^2 - \varepsilon_m \omega_{TO}^2)] \sum_{j=1}^{\infty} \frac{2}{j^3} \cos(jkd) \\ +(2\varepsilon_m \omega_{TO}^2 + \varepsilon_\infty \omega_{LO}^2) \end{array}}{B_0(\varepsilon_\infty - \varepsilon_m) \sum_{j=1}^{\infty} \frac{2}{j^3} \cos(jkd) + (\varepsilon_\infty + 2\varepsilon_m)} \tag{3.3}$$

This dispersion relation for a SiO_2 SPhP crystal [145] (a crystal in which the dominant lattice vibrations are SPhPs) in air ($\varepsilon_m = 1$) and in a partial water medium ($\varepsilon_m = 4$) are shown in Figure 3.7 and compared to the dispersion of light propagating in free space. The wave vector is normalized by the width of the first Brillouin zone, $2\pi/d$. The light line intersects the transverse mode SPhP dispersion at 224 Trad s^{-1} in air and 207 Trad s^{-1} in pure water; these are the locations for SPhP coupling to incident infrared light (thermally emitted from the nanoparticle bed in this case) predicted by the model. This result agrees with the FTIR-ATR measurements (Figure 3.2 inset). The SPhP dispersion curve gradients show that the wave can carry energy between nanoparticles, in any direction if the crystal is symmetrical, which motivates the KT model of SPhP conduction by wave propagation.

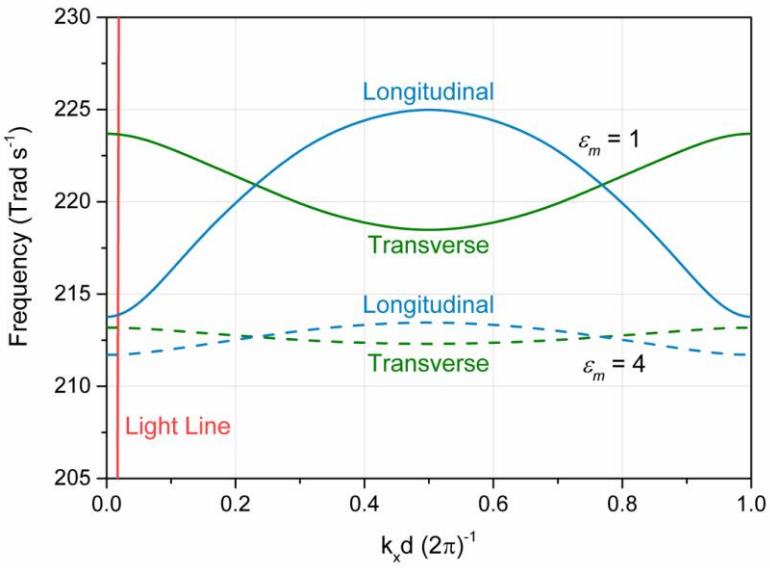

Figure 3.7. SPhP dispersion for a SiO_2 nanoparticle crystal in a background medium of $\varepsilon_m = 1$ (solid lines) and $\varepsilon_m = 4$ (dashed lines).

One-dimensional diffusive thermal conductivity in this framework is described generally in Section 2.3.1, and its application to this specific system is discussed in more detail in Appendix A.7. The resulting thermal conductivity as a function of temperature is shown in Figure 3.8. However, this model does not explain the experimental results. The thermal conductivity in this framework is proportional to the square of the group velocity. Considering the dispersion curves in two different media (Figure 3.7), it can be seen that for a higher permittivity medium, group velocities decrease and cause the calculated thermal conductivity to decrease. The same trend is also predicted by Ordonez-Miranda *et al.* for SiC nanoparticles [109]. The decrease in thermal conductivity with medium permittivity under this model is also shown in Figure 3.8. Furthermore, the calculated propagation lengths (see Appendix A.7) are on the order of the inter-particle spacing, which calls into question the applicability of a KT model for this system. This model therefore

does not explain the experimental results of increased SPhP thermal conductivity with increased medium permittivity.

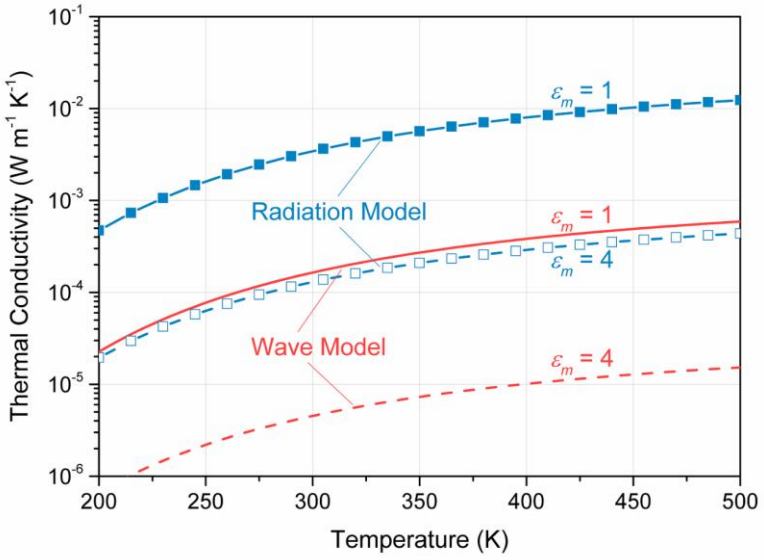

Figure 3.8. Thermal conductivity by wave (KT) and radiation (FE) models for a chain of 65 nm diameter SiO_2 particles in contact.

In the second FE model described in Section 2.3.2, a network of nanoparticles is viewed as a system of discrete electric dipoles interacting through many-body radiation. This provides the thermal conductance between any two particles, and this methodology is extended to calculate thermal conductivity along a chain (see Appendix A.7). Unfortunately, this model also fails to explain the experimental results. The transmission coefficient has a strong dependence on the polarizability of the nanoparticles [114], and the Clausius-Mossotti polarizability of the SiO_2 nanoparticles in this system decreases in a medium with higher permittivity than air (see Appendix A.7). Additionally, a medium with high permittivity results in a longer optical path length. These factors cause the radiative FE model to also predict a reduction in SPhP thermal conductivity with increasing medium permittivity, as shown in Figure 3.8.

3.3.2 New Scaling Relation

The failure of the SPhP conduction models described in the previous section, and an understanding of the long coherence lengths of SPhPs [146], motivates the use of a simplified ballistic model to interpret the experimental observations. This approach is further motivated by the good agreement of the FTIR-ATR measurements with the coupling frequencies predicted by the SPhP dispersion relation and by the ability of the dispersion relation to give information on the change in density of states (DOS) with medium permittivity. The oscillatory nature of the SPhP dispersion in k-space means an almost equivalent dispersion in lattice-space. Since the dispersion extends to all k-space, the wave field is spread across the entire SPhP crystal (the nanoparticle bed can be approximated as a nanoparticle crystal in this framework). Therefore a three-dimensional DOS is used to capture the behavior of a symmetrical crystal, and a Landauer formalism [147] is used to describe the thermal conductance in the system as

$$G = \frac{A_c}{4}\sum_{3}\int_0^{\infty} v_g(\omega) D_{3D}(\omega)\mathcal{T}(\omega)\hbar\omega\frac{\partial f^{(\mathrm{BE})}(\omega,T)}{\partial T}d\omega \tag{3.4}$$

where $A_c, v_g, D_{3D}, \mathcal{T},$ and f_{BE} are the cross-sectional area, group velocity, 3D DOS, probability of transmission, and Bose-Einstein carrier statistics, respectively. The summation is over the two degenerate transverse and one longitudinal polarizations. Equation (3.4) predicts the maximum conductance when $\mathcal{T} = 1$, which is equivalent to $G_0 = \pi^2 k_B^2 T/3h$ (the quantum of thermal conductance) times the total number of modes in the 3D SPhP crystal. The 3D DOS is modeled with the Debye approximation $D_{3D} =$

$\omega^2\left(2\pi^2 v_g^3\right)^{-1}$, the integration is changed to be over k, and the conductance is multiplied by the length d divided by the area to obtain the thermal conductivity as

$$\kappa = \mathcal{T}\frac{\hbar^2 d}{8\pi^2 k_B T^2}\sum_3 \int_0^{Br} \frac{\omega^4(k)}{v_g(k)} \frac{e^{\frac{\hbar\omega}{k_B T}}}{\left(e^{\frac{\hbar\omega}{k_B T}} - 1\right)^2} dk \tag{3.5}$$

The thermal conductance in Figure 3.9(a) and the thermal conductivity in Figure 3.9(b) are calculated for a unit cell of length $d = 2a$ (the inter-particle spacing). The thermal conductance is calculated for an air medium and is normalized by the conductance as temperature approaches infinity, G_∞. The x-axis uses a normalized temperature where ω_{max} is the maximum frequency of the dispersion relation. The vertical black dashed line shows the transition where few SPhP states are populated at lower temperatures. The thermal conductivity used Equation (3.5) fit to the data from Figure 3.4 for different values of medium permittivity and a probability of transmission of $\mathcal{T} = 0.01$.

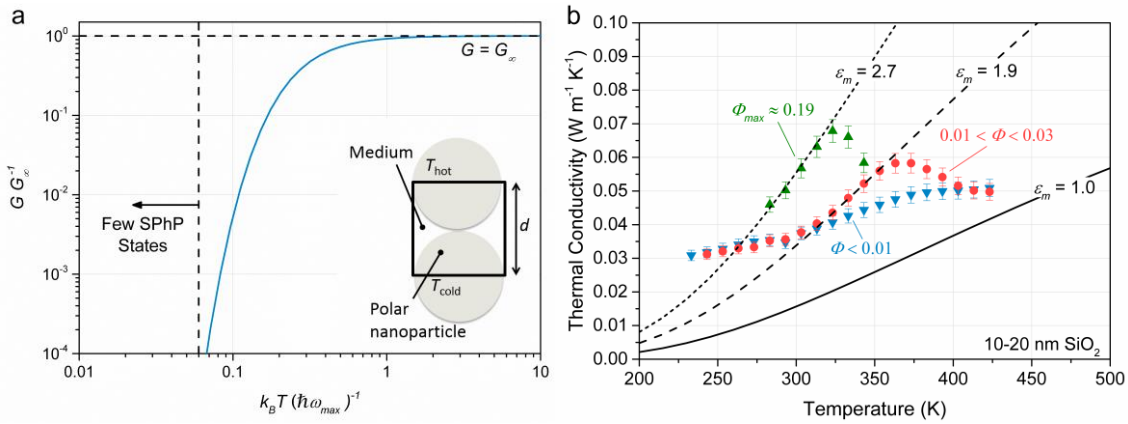

Figure 3.9. (a) Thermal conductance and (b) thermal conductivity of a SiO_2 nanoparticle crystal calculated with new scaling relation.

By comparing with the experimental measurements, an estimate of $\mathcal{T} = 0.01$ is obtained between neighboring particles, which agrees with the range of theoretically determined transmission probabilities for ballistic SPhPs in a chain of spheroidal SiC nanoparticles (reference [109], Figure 12). The factor is kept constant in Equation (3.5) because it is just an estimate, but a more realistic scenario would be a frequency-dependent transmission probability. There is also agreement between Equation (3.5) and the observed trend of a higher thermal conductivity for increased DOS (which results from a higher medium permittivity).

In this system, the SPhPs are self-excited by thermal radiation. This must span about 207 Trad s^{-1}, or 319 K by Wien's law [8], where the transverse optical phonons must be populated to support SPhPs. Because the nanoparticles can act as dipoles when they are small compared to the thermal wavelength [114], the energy of the typical acoustic and optical phonons may be transferred to the resonating optical phonons (and therefore also to the electric field) through inelastic scattering [148] with SPhPs under strong polarization. The scaling relation developed here approximates this effect in its use of the 3D Debye DOS, which allows SPhPs to occupy a continuum of all phonon states in SiO_2. Note that SPhPs can only begin to populate these states at frequencies near the SPhP resonance frequency, as indicated in the conductance trend of Figure 3.9(a). This observation may be unique to SiO_2 nanoparticle beds, however, because of the convenient location of the transverse optical phonon resonance frequency (temperature) near the temperature where conductivity departs from the phonon value.

3.4 Conclusions from Experimental Studies

Several important experimental and theoretical details require further investigation in order to fully understand the effects seen in these experiments. Multipole effects could play a significant role in the near-field interaction and coupling between nanoparticles [92, 109, 149], which are not accounted for in the two models examined here. The many-body radiation model does not include heat exchange between the nanoparticles and the interstitial medium, which could also alter the trends in predicted thermal conductivity. The scaling relation presented here, although it predicts trends with changing medium permittivity, does not fully capture the microscopic physics, and it under-predicts the high temperature conductivity of the ethylene glycol coated samples. Additionally, geometric effects such as water or ethylene glycol bridging between adjacent particles [150-153] could substantially alter both the phonon and radiation transport in these systems. However, these types of nonhomogeneous environments cannot be analyzed with the models presented here.

Despite the work remaining, these results demonstrate that SPhPs in nanoparticle beds may be capable of enhancing thermal transport over macroscopic length scales by an order of magnitude. When the interstitial medium around the particles is a high permittivity material, significant increases in the thermal conductivity are measured that cannot be explained by other heat transfer mechanisms. The high surface area to volume ratio and high thermal contact resistance between adjacent particles play an important role in enabling the observation of NFRHT in these systems. Importantly, these factors are inherent to packed nanoparticle beds, and they could be utilized in other types of nanostructure arrays with better control over materials and geometry. In contrast to

macroscale planar parallel surfaces, which are very difficult to fabricate, the nanoparticle beds studied here (and other possible types of nanostructure arrays) are fabricated and assembled quite easily without the need to maintain a small vacuum gap over a large area. This could lead to a new class of materials in which NFRHT is a heat transfer mechanism comparable to or exceeding contributions from phonon/electron conduction and convection.

CHAPTER 4. KINETIC THEORY FOR CHAINS OF POLARITONIC RESONATORS

One possible reason that a KT model did not match the experimental data in the previous chapter is that the environment around the nanoparticles could be nonhomogeneous, such as if water or ethylene glycol bridges form between adjacent particles. Nonhomogeneous environments are commonplace in practical situations, for the simple reason that it is very difficult to suspend an array of nanostructures in a uniform medium. For example, a substrate is usually needed to provide a platform to fabricate nanostructures of interest. Unfortunately, both the KT and FE models presented in Section 2.3 rely on source-field relations (dyadic Green's functions) for a uniform background medium. Determining the Green's functions for a nonhomogeneous medium is quite challenging, as evidenced by the limited number of exact solutions for NFRHT in simple geometries (described in Section 2.1.2). An alternative approach that doesn't require resorting to numerical methods would therefore be quite useful.

Another reason to pursue a NFRHT model for nonhomogeneous environments is that these environments may improve the electromagnetic coupling and energy exchange between nanostructures. For example, the predicted waveguide performance and NFRHT for nanoparticle chains in homogeneous surroundings has been limited due to inherent losses in metal-based SPPs [123] and strong dispersions (corresponding to low group velocities) for SPhPs in polar dielectrics [22]. However, for doped Si plasmonic resonators embedded in an intrinsic Si nanowire, the near-field coupling strength between two resonators is enhanced by four to five times compared to the same resonators in isotropic

vacuum or in isotropic intrinsic Si [154]. This behavior is caused by the combination of the anisotropic structure of the nanowire and intrinsic Si's large infrared permittivity, which focuses the electric field along the nanowire and suppresses transverse modes. If the resonators are repeated along the wire to create a chain, they could exhibit good waveguide performance and high radiative thermal conductivities due to the improved coupling strength. This structure is shown schematically in Figure 4.1(a) and Figure 4.1(b). A nanowire of diameter D containing many resonators is considered, such that any radiative thermal transport is diffusive. The resonators have length L and are separated by distance S or center-to-center spacing $d = L + S$. These structures may be grown very precisely [155, 156] with the bottom-up vapor-liquid-solid method [157], which could facilitate low-cost production of macroscale composites containing many nanowires, as depicted in Figure 4.1(c). Doped plasmonic resonators also offer the potential for tunability via optical pumping or electrostatic gating of the adjacent intrinsic regions [11, 158], which could lead to actively-modulated thermal transport.

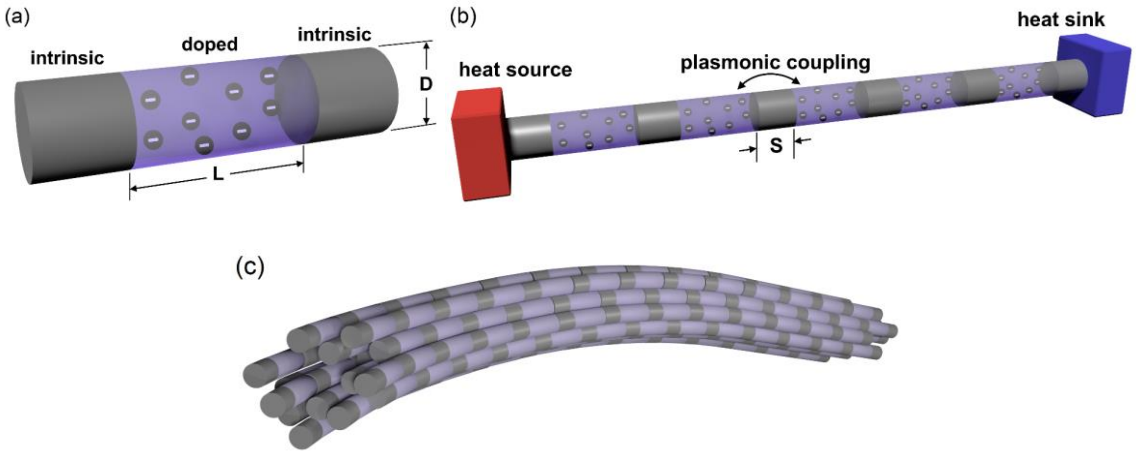

Figure 4.1. Schematics of (a) a doped plasmonic resonator in an intrinsic nanowire which can be (b) repeated along the nanowire and (c) organized into bundles.

In this chapter (also presented in references [89] and [113]), a new "absorption spectra" method is developed to calculate the dispersion relation for SPs propagating along a chain of resonators from common far-field spectral response data. The method is used to predict the waveguide performance and to calculate the radiative thermal conductivity of doped plasmonic resonators embedded in intrinsic semiconductor nanowires. Due to the enhanced near-field coupling between resonators, the group velocities and propagation lengths can be increased by up to an order of magnitude compared to the case of isotropic vacuum surroundings. This leads to radiative thermal conductivities up to about 1 W m^{-1} K^{-1} at 500 K, which is comparable to the phononic and electronic contributions to thermal conductivity.

4.1 Absorption Spectra Model

4.1.1 Dispersion Relation

Consider a chain of identical plasmonic resonators modeled as dipoles with center-to-center spacing d. If the resonators are SPP- or SPhP-supporting spherical nanoparticles, then the dipolar assumption is valid when d is approximately greater than or equal to three times the particle radius [78, 83]. For doped Si plasmonic resonators embedded in semiconductor nanowires, the transverse modes are strongly suppressed and longitudinal oscillatory behavior remains dipolar even at very close resonator spacings [154, 155, 159]. Following the example of Brongersma *et al.* [81], the dipolar resonators are modeled as harmonic oscillators [160] with displacement $\mathbf{x}$, restoring force spring constant K, effective mass m, and damping coefficient ζ. A polarized dipole in the chain will create an electric field at the neighboring dipoles that exerts a force proportional to the dipole displacement

$F = Bx$, where the vector notation for **x** is dropped because only 1D longitudinal polarization is considered. This leads to an equation of motion for the nth resonator in the chain:

$$\sum_{j=1}^{N} \omega_{c,j}^2 \left(p_{n-j} + p_{n+j}\right) = \frac{d^2 p_n}{dt^2} + \xi \frac{dp_n}{dt} + \omega_1^2 p_n \tag{4.1}$$

where N is the number of neighboring resonators considered and t is time. Also introduced are the coupling strength of the jth neighbors with the nth resonator $\omega_{c,j} = \sqrt{B_j/m}$, the dipole moment $p = qx$ where q is the charge, the damping ratio $\xi = \zeta/m$, and the natural frequency $\omega_1 = \sqrt{K/m}$. The left side of Equation (4.1) represents the force on the nth resonator due to the polarization of all other resonators, and the right side encompasses the motion and forces associated with the oscillation of the nth resonator. The form of a complex frequency $\tilde{\omega} = \omega + i\Gamma$ is assumed such that ω is the angular frequency and Γ is the damping rate [85], and propagating wave solutions to Equation (4.1) are sought of the form $p_{n\pm j} = P\mathrm{e}^{-\Gamma t - i[k(n\pm j)d - \omega t]}$ where P is the amplitude and k is the wavevector. After inserting this into Equation (4.1), simplifying, and separating the real and imaginary parts, the dispersion relation is obtained:

$$\begin{aligned} 0 &= \omega^2 - \Gamma(\Gamma - \xi) - \omega_1^2 + 2\sum_{l=1}^{N} \omega_{c,l}^2 \cos(kld) \ \text{(Real)} \\ 0 &= 2\Gamma - \xi \ \text{(Imaginary)} \end{aligned} \tag{4.2}$$

A more detailed derivation of the dispersion relation is provided in Appendix B.1. Equation (4.2) provides a relation between k, ω, and Γ that depends only on the spacing d, the coupling strength $\omega_{c,j}$ for each term in the summation, the natural frequency ω_1, and the damping ratio ξ. The imaginary part of the solution verifies the typical relationship between the damping rate and the damping ratio, $\Gamma = \xi/2$.

The dispersion relation is the key to defining waveguide performance with the following steps. The parameters in Equation (4.2) are first determined, as described in the following section, through spectral response measurements or numerical simulations. Once the inputs have been specified, k is varied from zero to the first Brillouin zone π/d to find the corresponding values of ω. With the dispersion then determined, the group velocity $v_g = \frac{d\omega}{dk}$ and the amplitude propagation length (1/e length) $\Lambda_a = v_g/\Gamma$ or energy propagation length (1/e length) $\Lambda = v_g/(2\Gamma)$ are calculated to evaluate spectral waveguide performance [85]. These parameters can then serve as inputs to the KT formalism to calculate the radiative thermal conductivity.

4.1.2 Damping Ratio, Natural Frequency, and Coupling Strength

The first two inputs, ξ and ω_1, are associated with the oscillation of single resonator. These inputs are therefore determined from the absorption spectrum of an isolated resonator in the background material being considered for the waveguide or thermal transport (e.g., a nanowire). Because a localized SPP or SPhP can be modeled as a damped harmonic oscillator driven by the incident light, ξ is simply the full-width at half maximum [8] and ω_1 is the absorption peak frequency for the isolated resonator [160]. To determine the coupling strength between two resonators, ω_c, the coupled equation of

motion is considered for two particles, designated a and b, driven longitudinally by the incident light:

$$\frac{2F_0}{m}\mathrm{e}^{i\omega t} + \omega_c^2 z = \frac{d^2z}{dt^2} + \xi\frac{dz}{dt} + \omega_1^2 z \tag{4.3}$$

Here $z = x_a + x_b$ is the sum of the displacement of the oscillators, the sinusoidal driving force $F(t)$ is represented by $F_0\mathrm{e}^{i\omega t}$, and the real part of the solution $z(t) = C\mathrm{e}^{i\omega t}$ represents the physical motion. The absorption peak frequency for the two-resonator system, ω_2, which can be experimentally measured or simulated, corresponds to the frequency at which the average power delivered to the resonators is maximized. After solving for C in the solution $z(t)$, this average power is given by

$$\langle F(t)\frac{dz}{dt}\rangle = \frac{F_0^2}{\xi m}\cdot\frac{\xi^2\omega^2}{\xi^2\omega^2 + (\omega_1^2 - \omega_c^2 - \omega^2)^2} \tag{4.4}$$

The absorption peak frequency is found by setting the derivative of Equation (4.4) with respect to ω equal to zero and solving for ω. This leads to the relation

$$\omega_2 = \sqrt{\omega_1^2 - \omega_c^2} \tag{4.5}$$

The coupling strength between two resonators may, therefore, be determined knowing only the natural frequency (which is the same as the absorption peak frequency for an isolated resonator) and the absorption peak frequency of the two resonators in proximity to each other. A more detailed derivation of this relation is provided in Appendix B.2.

Instead of performing measurements or simulations to obtain the absorption peak shift for all N resonator spacings in Equation (4.2), it is more efficient to only do so for a few spacings and then interpolate the others. The shift in absorption peak position with spacing for two plasmonic resonators is correlated by the empirical plasmon ruler equation [161], which is known to be valid for coupled resonators in both isotropic [162-166] and anisotropic [154, 161, 167-169] environments:

$$\frac{\omega_1 - \omega_2}{\omega_1} = A_0 \exp\left(-\frac{S/L}{\tau}\right) \tag{4.6}$$

where A_0 is a dimensionless constant, S is the separation distance between the resonators, L is the length of the resonators, and τ is the decay length scaling factor. τ indicates the rate at which the electric field decays away from the resonator, so larger values of τ are linked to stronger near-field coupling. Once absorption peak locations have been obtained for several different resonator spacings, the data may be fit to Equation (4.6) to obtain values for A_0 and τ. Despite its empirical nature, the exponential behavior of the shift in absorption peak may also be explained by a dipolar coupling model: as the resonators move closer or exert stronger fields on each other due to changes in geometry or material properties, the coupling strength between them also increases [161].

4.1.3 Summary of Method

For clarity, the steps in the absorption spectra method to calculate the dispersion relation are summarized here. First, measurements or simulations of the far-field absorption peak of an isolated resonator in the background medium of interest provide ω_1 and ξ. Additional far-field measurements or simulations for two coupled resonators at several

different spacings then provide several values for ω_2. For example, representative absorption efficiencies for intrinsic InAs [144] nanowires with n-type InAs resonators of doping concentration $N_e = 3.25\times10^{19}$ cm^{-3} [170] are shown in Figure 4.2(a). These data are fit to Equation (4.6) to obtain A_0 and τ, which allows the calculation of ω_2 for any resonator spacing. This fitting process is depicted for the same InAs structure in Figure 4.2(b). Second, Equation (4.6) and Equation (4.5) are used repeatedly to calculate N values of ω_c for N neighboring resonators. The coupling strength decays rapidly with increased spacing, so typically $N < 10$ is sufficient. The requirement for N will vary with material, geometry, and environment, so this should be checked for any specific application. Finally, k is varied from 0 to π/d and Equation (4.2) is solved for each value of k, which provides the dispersion relation. The dispersion for the same InAs structure is shown in Figure 4.2(c). With the dispersion, the mode v_g and Λ may be calculated to evaluate waveguide performance or to serve as inputs to find the KT radiative thermal conductivity.

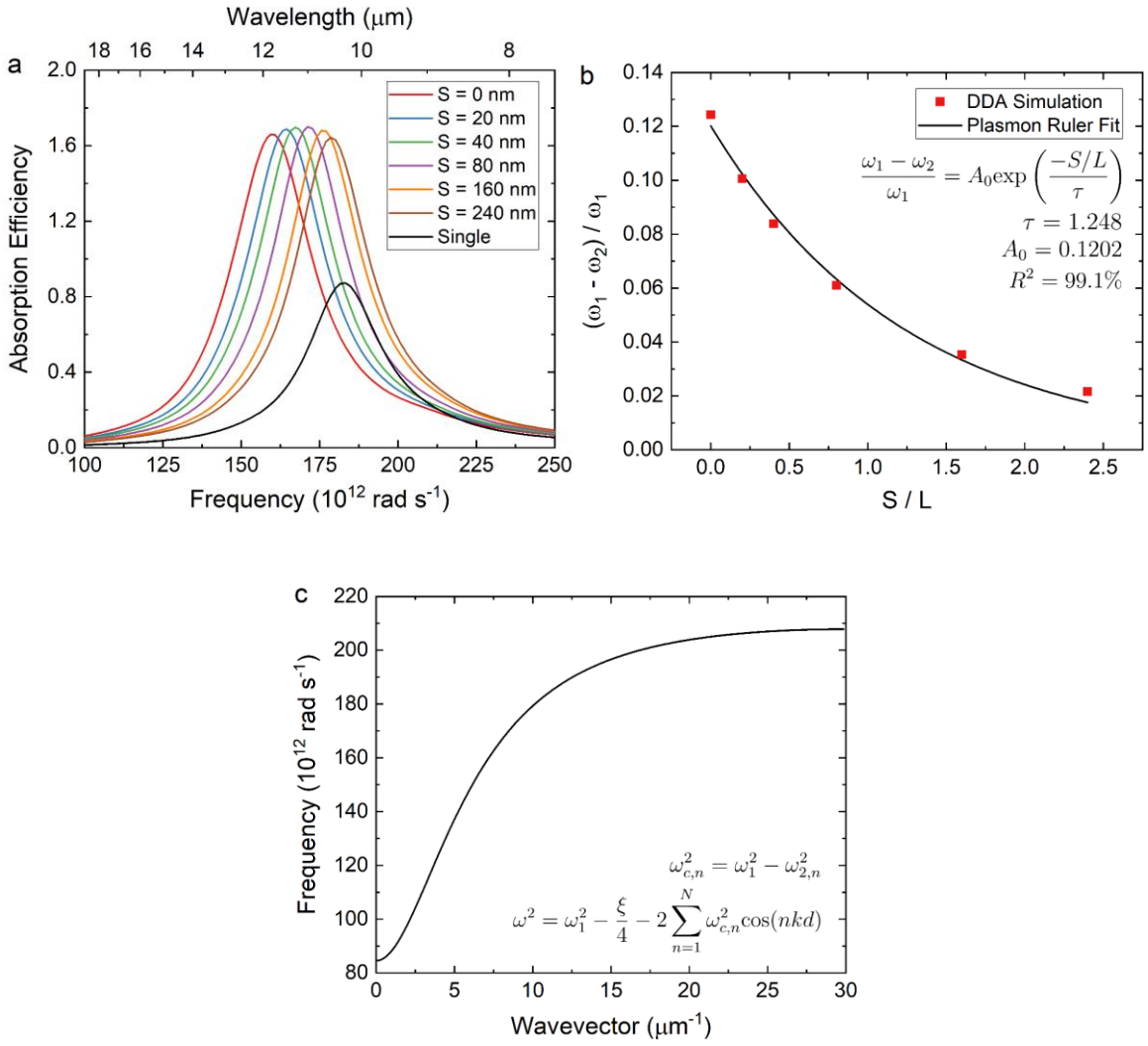

Figure 4.2. Representative (a) absorption spectra, (b) fit to the plasmon ruler equation, and (c) resulting dispersion for an InAs wire and resonators.

4.1.4 Validation

To verify that this method provides a good prediction of the dispersion, its results for spherical nanoparticle chains in homogeneous dielectric environments are compared to analytical solutions for the same materials and geometries. Absorption spectra for 12 nm diameter nanoparticles are calculated using the DDA with the well-established DDSCAT code [97]. The spectra for SiC particles and SiO_2 particles in background permittivities of

ε_m = 1 and ε_m = 4, respectively, are shown in Appendix B.3. For both materials, a Lorentz oscillator model for relative permittivity is fit to the optical constants [144] in the SPhP resonance spectral region, and this model is used to describe the particle permittivity for all scattering and dispersion calculations. The absorption spectra for a single nanoparticle provides the full-width at half maximum or damping ratio (ξ = 1.06×10^{12} rad/s for SiC; ξ = 1.62×10^{12} rad/s for SiO_2) as well as the absorption peak frequency or natural frequency (ω_1 = 1.75×10^{14} rad/s for SiC, ω_1 = 2.09×10^{14} rad/s for SiO_2). The DDA results for a single nanoparticle are also shown to be consistent with Mie theory in Appendix B.3 [78, 171]. The absorption peak frequencies for two particles separated by distances of 4, 6, 8, and 10 nm are then used to fit the values of τ and A_0 in the plasmon ruler Equation (4.6) (τ = 0.422, A_0 = 0.0143, R^2 = 99.2% for SiC; τ = 0.471, A_0 = 0.00881, R^2 = 99.5% for SiO_2). With the plasmon ruler equation, the peak absorption frequency for two resonators at an arbitrary separation distance can be specified, which allows the calculation of the coupling strength for N neighboring resonators with the repeated use of Equation (4.6) and Equation (4.5). Once all inputs are determined, Equation (4.2) is solved using a custom MATLAB code using d = 18 nm and N = 15 to find the dispersion relations and propagation lengths for SiC and SiO_2 nanoparticle chains, shown by the solid lines in Figure 4.3(a) and Figure 4.3(b). The corresponding analytical solutions are obtained from the longitudinal dispersion relation for a chain of point dipoles given by Equation (2.11). These are solved numerically in MATLAB and the results are shown by the dashed lines in Figure 4.3(a) and Figure 4.3(b). The dispersion relations provide the relationship between the wavevector and frequency for the allowed propagating modes. The

propagation lengths reach a maximum where the group velocity (slope of the dispersion) is largest.

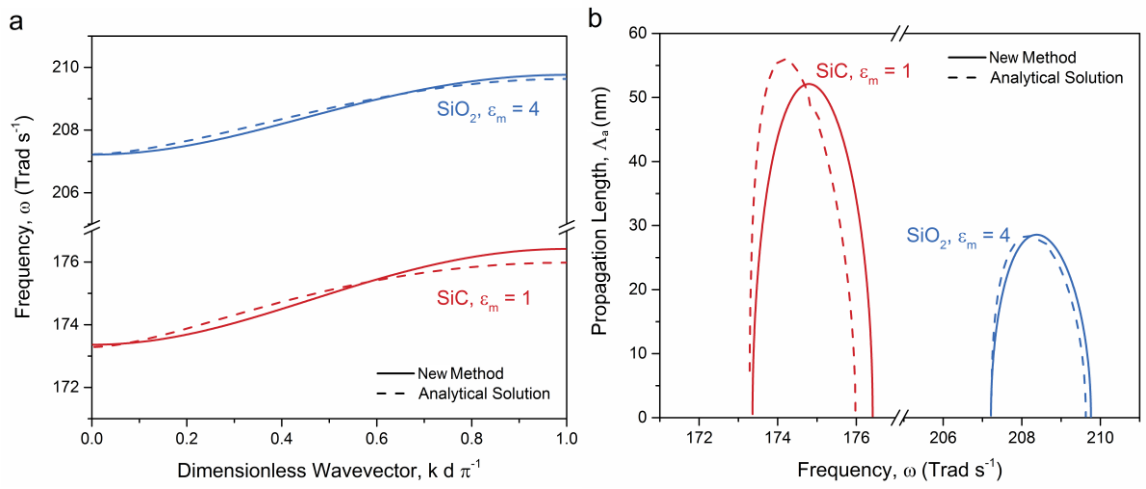

Figure 4.3. (a) Dispersion relations and (b) amplitude propagation lengths for SiO_2 nanoparticles from the new absorption spectra method and the analytical solution.

Both the dispersion relations and the propagation lengths calculated with the absorption spectra method agree well with the analytical solutions. The dispersion relations differ from the analytical solutions within 0.23%, and the maximum propagation lengths differ from the analytical solutions by 6.8% for SiC and 0.8% for SiO_2. The consistent shapes of the dispersions and close accuracy to the analytical solutions regardless of material or background permittivity show that the new method can account for these variations.

4.2 Waveguiding by Plasmonic Resonators in Nanowires

The proposed absorption spectra method is first used to predict the waveguide performance of chains of doped Si plasmonic resonators embedded in intrinsic Si nanowires. DDA simulations from prior work [154] are used as inputs to evaluate how the nanowire medium affects the group velocities and propagation lengths when compared to

a homogeneous vacuum environment. Waveguide performance modeled from experimental spectral response measurements is compared to performance modeled from the DDA simulations to determine how a real system differs from idealized simulations. Finally, new DDA simulation results are used to investigate the impact of resonator size, spacing, and dopant concentration.

4.2.1 Impact of the Nanowire Environment

DDA simulations for doped Si plasmonic resonators with a doping concentration N_e of 2.7×10^{20} cm^{-3} [172], diameter of 130 nm, and aspect ratio of 0.77 provide values for ω_1, ξ, and ω_2 for both isotropic vacuum and intrinsic Si nanowire environments [154]. The resulting dispersion relations, group velocities, and propagation lengths for this nanowire structure are shown in Figure 4.4(a), (b), and (c), respectively, for N = 15 nearest neighbours and a separation distance of 10 nm between adjacent resonators.

The anisotropic nanowire environment, as expected [154], alters the coupling between resonators and the waveguide characteristics significantly compared to the isotropic vacuum environment. Figure 4.4(a) shows that the nanowire dispersion exhibits steeper slopes and covers a broader frequency range, which translates to much higher group velocities in Figure 4.4(b). Because the damping does not change significantly between the two environments ($\xi = 1.16\times10^{14}$ rad/s for the nanowire case and $\xi = 1.24\times10^{14}$ rad/s for the vacuum case), higher group velocities directly lead to greater propagation lengths as shown in Figure 4.4(c). The maximum propagation length for the nanowire geometry is about eight times higher than that for the vacuum environment, but different resonator geometries or dopant concentrations can exhibit even larger waveguide performance

enhancements. For example, based on additional DDA calculations, a maximum propagation length of 1.01 μm is found for resonators with N_e = 1×10^{21} cm^{-3}, diameter of 150 nm, aspect ratio of 0.8, and separation distance of 10 nm. This represents an order of magnitude increase over the case of the same resonators in a vacuum environment.

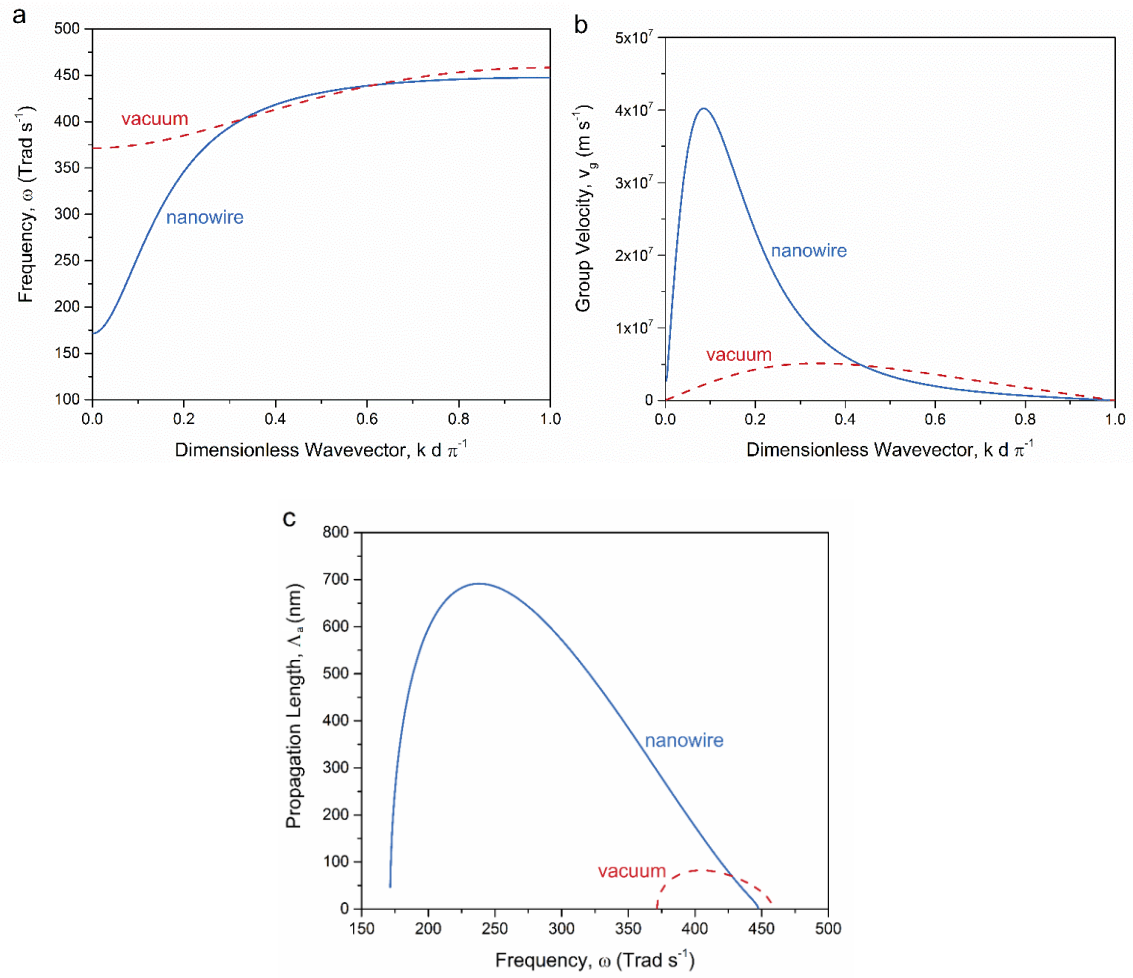

Figure 4.4. (a) Dispersion relations, (b) group velocities, and (c) amplitude propagation lengths for doped Si resonators in vacuum and in a nanowire.

4.2.2 Inputs from Measurement vs. Simulation

A significant advantage of the absorption spectra method is that it can use experimental measurements to predict dispersion relations. Such spectral response

measurements capture the effects of nonidealities such as defects and dopant concentration gradients, and they give a better indication of real-world coupling strength than numerical simulations may provide. To illustrate how measurements may lead to different results than DDA simulations, waveguide predictions using experimental Fourier-transform infrared (FTIR) spectroscopy measurements are compared to predictions using DDA simulations for the same resonator properties and geometries as discussed in the previous section [154]. The resulting dispersion relations and propagation lengths are shown in Figure 4.5(a) and Figure 4.5(b), respectively.

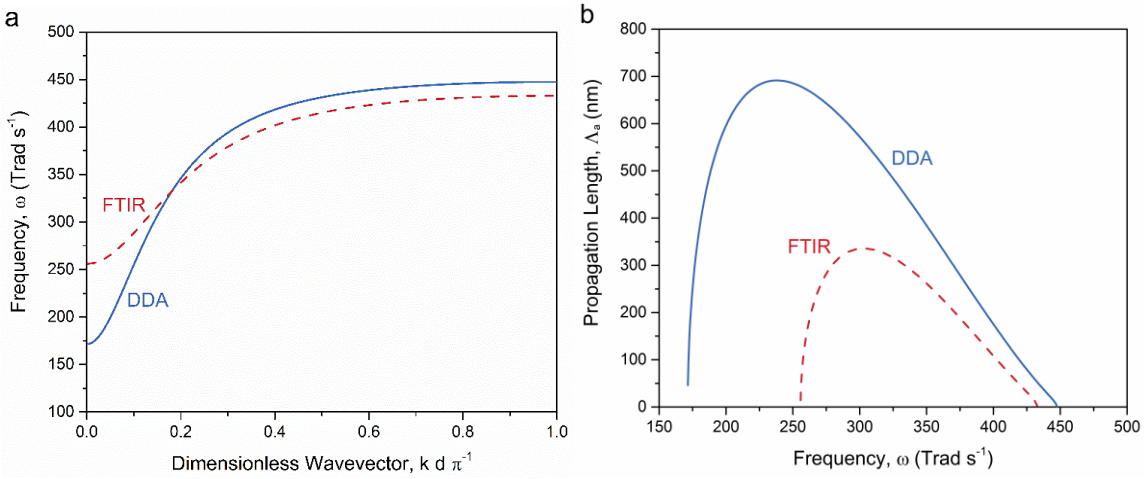

Figure 4.5. (a) Dispersion relations and (b) amplitude propagation lengths using inputs from FTIR spectroscopy measurements and from DDA simulations.

Although measurements and simulations yield similar inputs for the dispersion model (τ = 1.34, A_0 = 0.0886, ω_1 = 3.93×10^{14} rad/s, ξ = 1.16×10^{14} rad/s from FTIR measurements and τ = 1.70, A_0 = 0.106, ω_1 = 4.01×10^{14} rad/s, ξ = 1.16×10^{14} rad/s from DDA simulations), Figure 4.5 demonstrates that the differences are enough to cause substantial variation in waveguide properties. Stronger coupling in the DDA case causes a steeper dispersion and a maximum propagation length about double that predicted from the

FTIR case. Because the input parameters for the DDA calculations are selected to match the experiments, the differences in Figure 4.5 suggest that nonidealities in the growth or measurement processes (e.g., inhomogeneous broadening due to a distribution of nanowire diameters and thus resonator aspect ratios) are responsible for about a 50% reduction in peak propagation length. These differences highlight the importance and usefulness of utilizing experimental spectral response measurements, when possible, to predict the waveguide properties.

4.2.3 Dependence on Resonator Properties and Spacing

DDA simulations are useful to quickly evaluate different materials, geometries, and properties of resonator waveguides, even though they may not capture the nonidealities that exist in real devices. DDA simulations are performed on resonators with different dopant concentrations, aspect ratios, and spacings to elucidate the impacts of these parameters on waveguide performance. Starting with the baseline properties of N_e = 3×10^{20} cm^{-3}, AR = 0.8, and a diameter of 150 nm, the spacing is varied for different values of N_e and AR while holding other properties constant. The resulting maximum propagation lengths are shown in Figure 4.6(a) for different aspect ratios and Figure 4.6(b) for different dopant concentrations.

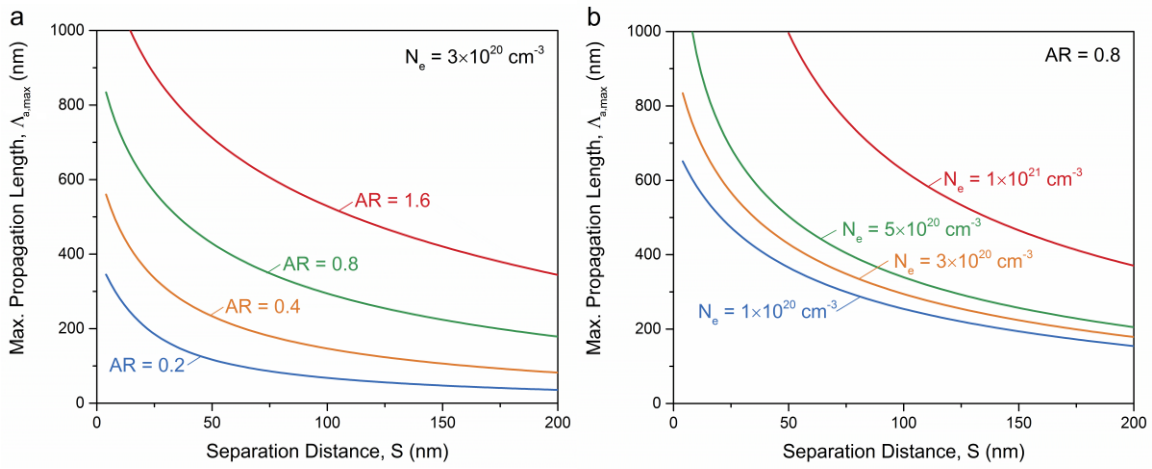

Figure 4.6. Impact of resonator separation distance on amplitude propagation length for differet (a) aspect ratios and (b) dopant concentrations.

Several interesting trends can be seen by examining Figure 4.6. First, the known effect that a larger spacing between resonators results in lower propagation lengths regardless of the other resonator properties is observed. This is because the benefits of lower loss with larger spacing are always outweighed by a the exponentially decreasing coupling strength with larger spacing [161]. However, the anisotropic nanowire environment shifts all curves to longer propagation lengths than would be obtained in an isotropic environment. Second, Figure 4.6(a) shows that higher aspect ratios lead to longer propagation lengths for the same resonator spacing. This is somewhat surprising, considering low aspect ratios result in high decay length scaling factors, which is typically associated with high coupling strength [154]. Larger aspect ratios are also associated with a substantial increase in A_0 and a decrease in S/L in the plasmon ruler equation, which together drive a large absorption peak shift corresponding to a high coupling strength. Third, Figure 4.6(b) shows that a higher dopant concentration causes larger propagation lengths for the same resonator spacing. In this case, the higher charge density results in stronger electric fields associated with the plasmon oscillation. This increases both τ and

A_0 in the plasmon ruler equation, and the enhanced coupling strength is enough to outweigh the negative effects of stronger damping with increased dopant concentration. A final important feature of Figure 4.6(b) to note is that the curve for the highest dopant concentration, $N_e = 1\times10^{21}$ cm^{-3}, has a lower limit for spacing of about 50 nm, while the other cases all contain data down to about 10 nm spacing. This is because, for this dopant concentration, below 50 nm the dispersion curve becomes so steep that group velocities exceed the speed of light in intrinsic Si, as shown in Appendix B.3. These steep portions of the dispersion are removed from the data to avoid inflated propagation lengths, but they should be examined carefully in future work to determine their origin and significance.

4.2.4 Discussion of Model and Waveguiding Results

The proposed absorption spectra method to predict dispersion characteristics offers two opportunities to advance sub-diffractional waveguide performance. First, the ability to quickly simulate absorption and scattering spectra with readily available code such as DDSCAT, in conjunction with the new model, means that different resonators and environments may be efficiently tested and optimized for desired waveguide properties. This process may be performed for arbitrarily complex resonator geometries and environments, with the only limitation being computation of the absorption and scattering from pairs of resonators. Second, the ability to use experimental spectral response data for two coupled resonators to calculate the dispersion allows any nonidealities or other physical system effects to be captured in the model. Using both experimental and simulation data may allow researchers to quantify the impact of experimental defects or other features not included in simulations.

A future area of improvement for the model is to develop a better understanding of dispersion behavior for resonators with very strong coupling. As discussed in the previous section, this results in excessively steep dispersion relations at small frequencies and wavevectors. It is difficult to analyze the model in these regions because analytical comparisons are not available. The system used for validation of the model, nanoparticle chains in the dipolar limit, does not have strong enough coupling to create these very steep dispersions. More complex electromagnetic numerical simulations may be able to address this open question.

The resonators investigated here, plasmonic doped semiconductors, may present interesting opportunities to tune and control waveguide behavior due to their many adjustable characteristics. In addition to the role of aspect ratio and spacing examined here, more complex geometric features can be investigated [154, 173]. In the case of semiconductors, it is also possible to actively tune plasmon resonances via electric field [158, 174] or light illumination [11], which could allow active modulation of waveguide performance. While doped Si is examined here, resonators made from other III-V semiconductors with lower damping rates [175] could significantly increase waveguide propagation lengths [176], and polar III-V semiconductors could offer waveguiding by SPhPs instead of SPPs [22]. Additionally, the potential for high fabrication throughput via bottom-up synthesis holds promise for much simpler and lower-cost waveguides than top-down synthesized waveguides may allow. Bottom-up synthesis also provides access to structures that may not be fabricated through top-down methods, such as hybrid III-V/IV nanowires [177].

4.3 Heat Transfer by Plasmonic Resonators in Nanowires

Thermal transport in a nanoscale material or composite is typically dominated by electronic contributions in metals and phononic contributions in insulators [8]. Photonic effects, on the other hand, are rarely considered for thermal transport within a material due to their low far-field energy density and tendency towards fast absorption in most media [178]. The nanowire structures examined in in this chapter, however, offer an opportunity to change this paradigm. Previous research on thermal conduction by coupled polaritonic modes has several limitations. One is the assumption of ballistic propagation [110, 111], which is only applicable to repeated particles of nanoscale array lengths due to typical propagation lengths on the order of tens to hundreds of nanometers. Another limitation is choosing optimized particle shapes and orientations [109-111], which may be difficult to fabricate or assemble. Even for optimized geometries, predicted maximum thermal conductivities in nanostructure arrays due to the photonic component are relatively limited, as discussed in Section 2.3.1.

In this section, the nanowire structures are investigated for their ability to address these limitations and achieve significant radiative thermal transport. Details of the materials being analyzed, and the methods used to calculate photonic thermal conductivity are provided. Results are presented on the effects of nanowire geometry in order to optimize the photonic component. It is found that small diameter nanowires with long resonators can achieve photonic thermal conductivities up to about 1 W m^{-1} K^{-1} at 500 K.

4.3.1 Calculation Methods

To use a KT formalism to calculate thermal conductivity, the dispersion for propagating plasmons along the chain must first be obtained. The absorption spectra method described in the previous section is used because it is valid for plasmonic resonators in arbitrary nonhomogeneous environments such as nanowires, and it allows the dispersion of a long chain to be calculated from absorption characteristics of just two resonators.

The DDA with the DDSCAT software [97] using the FLTRCD method is used to obtain infrared absorption efficiency, defined as the absorption cross section divided by the cross-sectional area of an equivalent volume sphere, for a single resonator as well as two resonators embedded in a nanowire with varying S. The materials and optical properties are taken as either intrinsic Si [144] with n-type doped 3×10^{20} cm^{-3} Si resonators [172] or intrinsic InAs [144] with n-type doped 3.25×10^{19} cm^{-3} InAs resonators [170], which are experimentally achievable. It is important to verify the applicability of optical data or models over the entire frequency range to be examined, which has been done for these materials. Si is an attractive material for its low cost and scalability, while InAs provides an interesting comparison because of its low loss and good carrier mobility, which has motivated studies of InAs for plasmonic devices [179]. Once the absorption data has been obtained, the dispersion relations are calculated according to the methods described in Section 4.1. All calculations are performed for $N = 15$ nearest neighbors, which is sufficient for the calculations to converge.

The dispersion provides the inputs needed to calculate thermal conductivity, namely the group velocity $v_g = \partial\omega/\partial k$ and the energy propagation length $\Lambda = v_g(4\xi)^{-1}$. A KT formalism is then used to calculate radiative thermal conductivity with Equation (2.16). All calculations are performed for $T = 500$ K. This equation assumes that all the resonators are near thermal equilibrium, so the temperature gradient is small. Large temperature differences along the nanowire could lead to effects such as nonlinear temperature gradients, and the effective thermal conductivity would have to be calculated with a different method [114, 115].

4.3.2 Radiative Thermal Conductivity of Nanowire Systems

The effect of the nanowire environment is first evaluated by comparing the nanowire system shown in Figure 4.1(b) to the same chain of plasmonic resonators immersed in an isotropic vacuum. For this latter case, the geometry and spacing of the resonators is unchanged, but the intrinsic regions illustrated in Figure 4.1(b) are replaced by vacuum such that the resonators are 'floating' in space. These calculations are performed for both Si and InAs, and the results are shown in Figure 4.7 for $D = 100$ nm and $S = 5$ nm. These dimensions are used as a starting point because nanowires of this diameter have been grown previously [154, 155] and small separation distances exhibit good electromagnetic coupling [89]. For both materials, the spectral thermal conductivity in Figure 4.7(a) and (b) is an order of magnitude higher when the resonators are embedded in the nanowire, resulting in thermal conductivities of 1.1×10^{-3} (1.56×10^{-4}) W m^{-1} K^{-1} in vacuum and 1.46×10^{-2} (1.29×10^{-2}) W m^{-1} K^{-1} in the nanowire for InAs (Si). Because ξ does not change appreciably with the resonator environment [89], the increase in thermal

conductivity is a direct result of stronger coupling. This leads to higher group velocities as seen in Figure 4.7(c) and (d) and longer propagation lengths as shown in Figure 4.7(e) and (f). Propagation length clearly plays a significant role in determining the total thermal conductivity, as illustrated in Equation (2.16), but the spectral region where the surface plasmons propagate also influences the results through the $\hbar\omega$ and $\partial f^{(\mathrm{BE})}/\partial T$ factors. Higher frequencies carry more energy, but those states also have a lower thermal population of carriers as given by the Bose-Einstein distribution. The combined $\hbar\omega\,\partial f^{(\mathrm{BE})}/\partial T$ is plotted in Appendix B.4, which shows that from a thermal transport perspective it is always preferable to have lower frequency modes if this does not adversely affect the coupling strength.

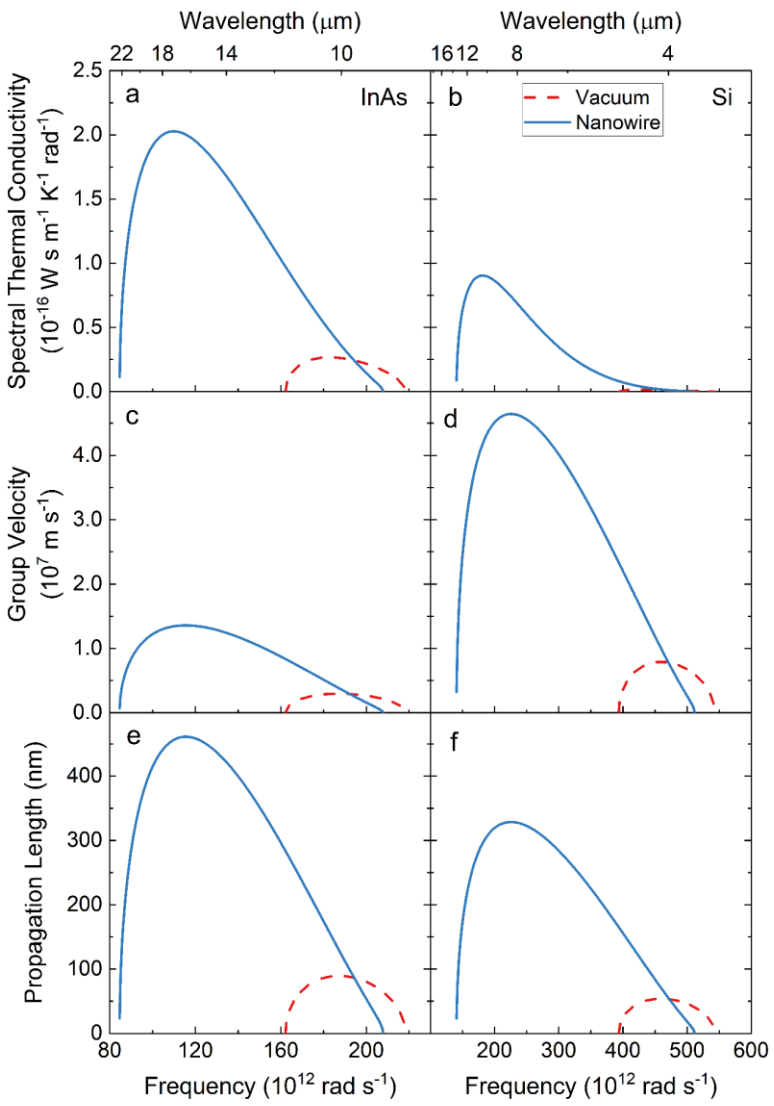

Figure 4.7. Spectral thermal conductivity, group velocity, and propagation lengths for InAs and Si material systems in a nanowire and in vacuum.

To optimize photonic thermal transport in these nanowire systems, the impact of nanowire and resonator geometry are investigated by varying D and L. Figure 4.8(a) shows the total photonic thermal conductivity for InAs and Si versus nanowire diameter for $S =$ 5 nm, either fixing $L =$ 100 nm or $AR = LD^{-1} = 1$. Diameters down to 10 nm are examined, because $D =$ 10 nm has been experimentally demonstrated [180] and smaller D requires more computational resources because of the finer discretization needed with the

DDA simulations. S is kept at 5 nm because this is an attainable separation distance for the resonators [155, 156], and because smaller S will lead to stronger coupling [89] and therefore higher photonic thermal conductivity (for example, see Appendix B.4). At smaller separation distances, the radiation formalism employed may break down as transport transitions from thermal radiation to conduction [181-183]. When AR is constant, a 3.8 times increase in κ is observed for InAs and no increase for Si as D decreases from 100 to 10 nm. These results are due to competing effects. κ is proportional to D^{-2}, which tends to increase κ with decreasing D. The plasmon ruler equation parameters τ, A_0, and ω_1 are not strongly affected, as illustrated in Appendix B.4. However, the constant AR means that L decreases with smaller D. Decreasing L hampers coupling between resonators because the coupling strength decreases with the exponential of $-S/L$ as shown by Equations (4.5) and (4.6). This reduces the propagation lengths for both materials, as illustrated in Appendix B.4, which partially counteracts the $\kappa \propto D^{-2}$ effect for InAs and completely counteracts this effect for Si, as shown in Figure 4.8 and Appendix B.4. The coupling strength and propagation lengths are reduced more for Si than InAs because Si has a higher resonance frequency, which requires a larger change in coupling strength for the same change in L as shown by Equation (4.6). Doping InAs to the level of that for Si would increase its resonance frequency and the trend in thermal conductivity vs. diameter for constant AR would be closer to the trend for Si.

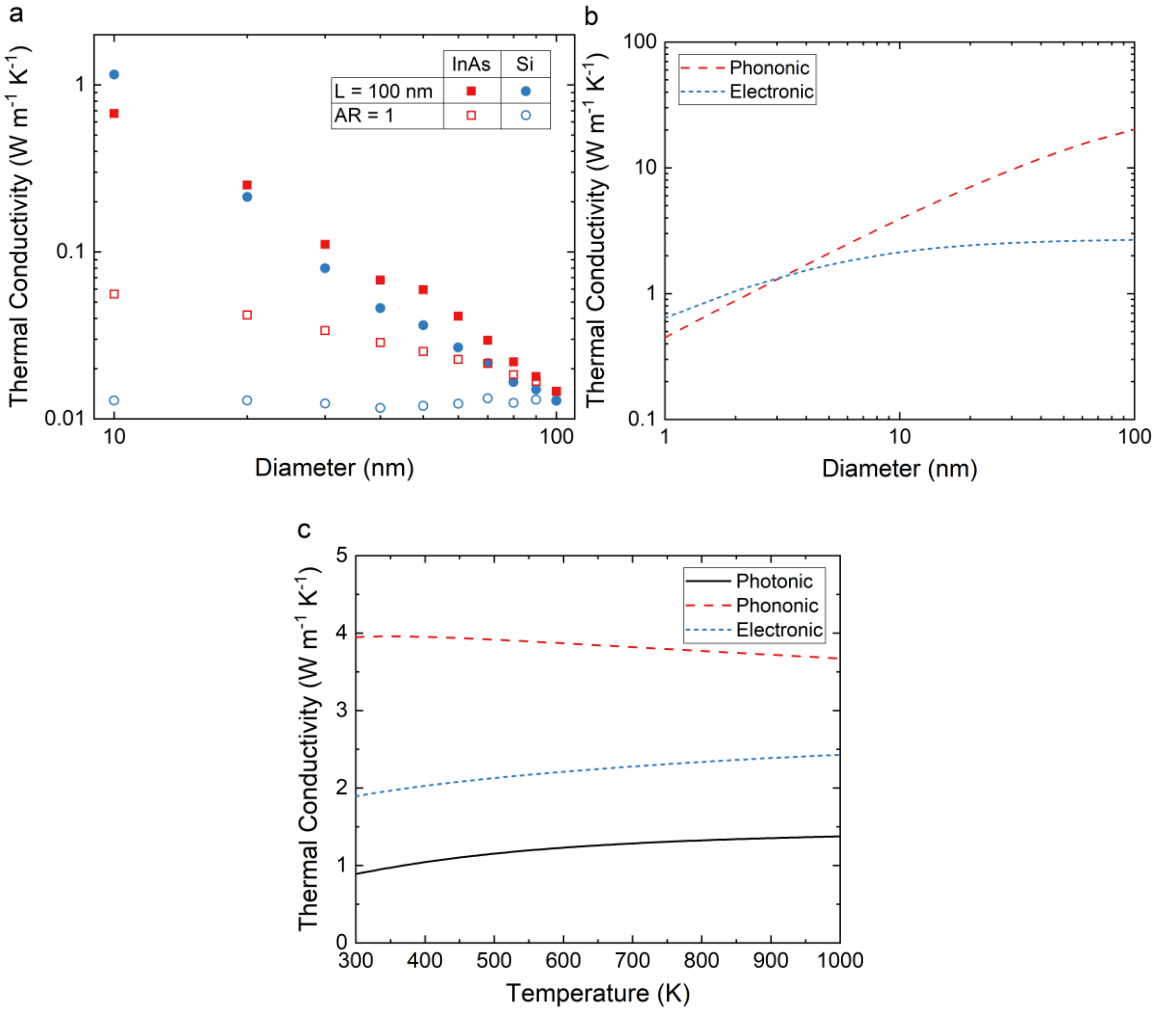

Figure 4.8. Contributions to thermal conductivity from (a) radiation with S = 5 nm, (b) phonons and electrons in a Si nanowire, and (c) all modes in a Si nanowire.

When L is constant, significant increases in κ with decreasing D are observed for both InAs and Si, resulting in the largest calculated $\kappa = 1.15$ W m^{-1} K^{-1} for Si at $D = 10$ nm. The increase in κ is largely driven by its proportionality to D^{-2}, but other factors must also be considered. In the plasmon ruler equation, A_0 increases, τ substantially decreases, and ω_1 decreases as the diameter is reduced with nearly identical trends for InAs and Si, shown in Appendix B.4. Decreasing τ reduces the coupling strength, which is partially counteracted by the increase in A_0, which increases the coupling strength. This results in

reduced propagation lengths as shown in Appendix B.4, although the reductions are not as drastic as when AR is held constant. In addition to these impacts on the coupling strength and propagation lengths, the dispersions redshift with reduced diameter as illustrated in Appendix B.4. This moves the $\omega\,\partial f^{(\mathrm{BE})}/\partial T$ term of Equation (2.16) to higher values as indicated in Appendix B.4 and increases the thermal conductivity. Slightly different enhancements between InAs and Si result from this shift, which can be understood by comparing several of the figures in Appendix B.4. As the InAs dispersion shifts, it moves from a steep portion of the $\omega\,\partial f^{(\mathrm{BE})}/\partial T$ curve to a shallower portion at lower frequencies. Si, on the other hand, begins at a higher frequency and the majority of the dispersion remains on a steep portion of the $\omega\,\partial f^{(\mathrm{BE})}\partial T$ curve as the dispersion redshifts. This difference is responsible for the higher thermal conductivity of the Si nanowire at 10 nm diameter, indicating the potential of this common semiconductor.

The photonic thermal conductivity is comparable to that expected for the electronic and phononic contributions in small nanowires. For comparison, plotted in Figure 4.8(b) and (c) are the estimated phonon and electron thermal conductivity of a single-crystal n-type silicon nanowire with phosphorus concentration of 3×10^{20} cm^{-3}. The bulk phonon and electron conductivities are calculated with the Boltzmann transport equation in the relaxation-time approximation [184-186] using input data from Ohishi *et al*. [187], which provides good agreement with experimental data for high dopant concentrations. Effective carrier mean free paths are calculated following the method of Dames and Chen [188], which are used to calculate thermal conductivity of the nanowire with a Boltzmann transport equation approach [189] assuming diffuse boundary scattering [8]. The photonic and phononic/electronic thermal conductivities have opposite trends with diameter, which

suggests that small diameter nanowires may be an ideal platform to experimentally resolve photonic contributions to thermal transport. The decreasing phononic and electronic contributions are due to a decreasing effective mean free path as the diameter is reduced. At diameters less than 10 nm, the photonic component may even exceed the phononic and electronic components. The photonic and phononic contributions also have opposite trends with temperature, which suggests that elevated temperature or temperature-dependent tests may permit the measurement of photonic thermal conduction. The phonon contribution decreases due to the increased phonon scattering rate, while the photon part increases according to the thermal population of states as illustrated in Appendix B.4. It is important to note that temperature-independent optical properties are used here. For highly-doped semiconductors with moderate temperature increases from 300 K to 500 K, this is a reasonable assumption because increasing carrier-lattice scattering and decreasing carrier-impurity scattering tend to offset each other [190, 191]. If the resonators were polar dielectric materials supporting SPhPs such as SiC, the phonon-phonon scattering would increase with temperature, although this has been experimentally shown to have a small effect at temperatures up to 500 K [192]. The alternating doped/intrinsic regions of these nanowires may also introduce additional scattering events for phonons and electrons, or the structure could be engineered with defects or geometric features [173] to further decrease the phonon and electron thermal conductivities.

4.4 Conclusions from Kinetic Theory Modeling

The new absorption spectra model provides a method to determine the dispersion of chains of SP-supporting nanoscale resonators in arbitrary nonhomogeneous environments using experimental or simulated spectral response data. This allows the

analysis of materials and geometries which were not previously accessible with analytical methods. Using this approach, an experimentally practical nanoscale material structure is proposed that is capable of achieving substantial photonic thermal conduction. The photonic thermal conductivities can reach about 1 W m^{-1} K^{-1} for 10 nm diameter nanowires at 500 K, which is a higher thermal conductivity at a lower temperature than previous predictions for particle chains. Because the phononic and electronic contributions to thermal transport decrease with decreasing nanowire diameter and increasing temperature, the photonic effects are non-negligible in this regime and present an opportunity to experimentally observe photonic conduction by surface plasmons.

These results demonstrate a pathway towards significant photonic thermal transport in nanoengineered structures, but additional work is needed to identify ideal materials, geometries, and operating conditions for this transport mechanism. Future analytical work should focus on further optimization of coupling between resonators, including investigating the impact of dopant concentration [193] and nonuniform/noncircular nanowire cross-sections, to increase the photonic thermal transport beyond that predicted in this work. Future experimental efforts such as thermal conductivity measurements of single nanowires [194] could confirm the predictions provided here.

CHAPTER 5. FLUCTUATIONAL ELECTRODYNAMICS FOR PARTICLES OR SUBVOLUMES

A FE approach to NFRHT between nanostructures provides some advantages over a KT approach. One of the most significant of these is that FE directly describes all thermal-electromagnetic interactions, not just the propagating resonant modes (coupled SPs) captured by KT. As described in Section 2.3.1, other interactions such as propagating photons, frustrated evanescent waves, or magnetic effects can be strong for certain materials and thus lead to underpredictions by KT of the NFRHT. Furthermore, the applicability of KT is questionable when the modal propagation lengths are small compared to the nanostructure spacing as described in Chapter 3, which has led to broader criticism of KT by Kathmann *et al.* [124] and is addressed in detail in Chapter 6. These factors motivate the use and development of FE methods for NFRHT in nanostructure arrays.

As described in Section 2.3.2, exact FE solutions for systems of many nanostructures are mostly unavailable due to the complexity of determining system Green's functions, with the notable exception of a linear chain of spheres [33]. Instead, structures such as nanoparticles are commonly approximated as point dipoles in the "many-body" theory. This approach was introduced in the early 2010s for spherical nanoparticles by Ben-Abdallah *et al.* [114] and Messina *et al.* [115], and subsequent research has adapted the theory for anisotropic particles [117], magnetic polarization [53, 119], core-shell particles [121], and point multipoles [122]. A similar approach has been developed by Edalatpour and Francoeur [50-52] for a numerically exact method of describing radiative transfer

between arbitrary volume-discretized bodies, known as the T-DDA. However, a key difference exists between the many-body theory and the T-DDA: the many-body method uses an *exciting* field formalism, where the induced dipole moments are related to the incident external electric fields, while the T-DDA uses an *actual* field formalism, where the induced dipole moments are related to the total macroscopic electric fields. This in turn requires different forms of the fluctuation-dissipation theorem, which describes the fluctuating thermal currents [15, 24, 195-197]. The distinction between the two approaches is similar to that between two numerical methods for classical electromagnetic scattering, the coupled dipole method (*exciting* field formalism) and the method of moments (*actual* field formalism), which have been shown to be mathematically equivalent [107]. However, the relationship between the two methods for NFRHT has not been examined.

The many-body and T-DDA methods allow the calculation of radiation exchange between pairs of dipoles or total power absorbed by individual dipoles. However, in some circumstances, these quantities may not be very useful by themselves, such as when comparing modes of heat transfer in nanoparticle beds or arrays of plasmonic resonators [112, 113, 126, 132]. In these situations, an effective thermal conductivity due to thermal radiation would permit direct comparison against phonon thermal conduction in addition to providing a more familiar figure of merit for thermal applications.

A significant limitation of both the many-body theory and the T-DDA is their computational requirements. They are formulated such that the calculation of NFRHT involves the inversion of a large $3N \times 3N$ interaction matrix (as shown in Section 2.3.2), where N is the number of particles or subvolumes. Matrix inversion is most commonly accomplished by lower-upper decomposition, which uses $\mathcal{O}[(3N)^3]$ operations and storage

of $\mathcal{O}[(3N)^2]$, because the entire interaction matrix must be stored [94, 97]. For large N, the computational time and memory requirements quickly become prohibitive, even with high-performance computing resources. The DDA for scattering calculations has managed to circumvent these limitations, however, by casting the equations in the form $\mathbb{A} \cdot \mathbf{x} = \mathbf{b}$ where $\mathbf{x}$ is the unknown vector, which admits iterative numerical solutions that can be much faster than inverting $\mathbb{A}$. A similar approach for the T-DDA and many-body methods would significantly improve their capabilities and usefulness.

This chapter (also partly presented in reference [198]) demonstrates that the many-body method and T-DDA are mathematically equivalent, unifying the two theoretical approaches and clarifying the appropriate use of the fluctuation-dissipation theorem. It is shown that when an actual field formalism is used (T-DDA approach), the fluctuation-dissipation theorem may be used directly, in contrast to an exciting field formalism (many-body approach) that requires the correlation function to be determined from the emitted thermal fields [115]. A computational method to calculate the effective diffusive radiative thermal conductivity of large arbitrary systems of dipoles is also developed. The method is applied to ordered and disordered arrays of SiC and SiO_2 nanoparticles and validated against the exact solution for linear chains of spherical particles [33]. Finally, a theoretical approach is developed for NFRHT between many particles or subvolumes that avoids the requirement of inverting an interaction matrix. This approach finds the system Green's functions between dipoles that account for all scattering interactions in the form $\mathbb{A}\mathbb{G} = \mathbb{B}$, which admits iterative solutions. The system Green's functions are then used to derive expressions for the power exchange between particles or subvolumes.

5.1 Equivalence of Many-Body and T-DDA Methods

5.1.1 Fluctuating and Induced Dipole Moments

Consider a system of N nonmagnetic nanoparticles or subvolumes modeled as electric point dipoles immersed in a transparent background medium of relative permittivity ε_m. The total electric field at location $\mathbf{r}$ and frequency ω is then given by both the many-body method [115] and the T-DDA [51] as

$$\mathbf{E}(\mathbf{r},\omega) = \frac{k^2}{\varepsilon_m \varepsilon_0} \sum_i \mathbb{G}^{(0)}(\mathbf{r},\mathbf{r}_i,\omega) \cdot \mathbf{p}(\mathbf{r}_i,\omega) \tag{5.1}$$

where $k^2 = \varepsilon_m \omega^2/c^2$ with c the speed of light in vacuum, ε_0 is the vacuum permittivity, $\mathbf{p}(\mathbf{r}_i,\omega)$ is the total dipole moment of the ith dipole, and the summation runs over all dipoles. $\mathbb{G}^{(0)}(\mathbf{r},\mathbf{r}_i,\omega)$ is the dyadic Green's function for the background medium given by

$$\mathbb{G}^{(0)}(\mathbf{r},\mathbf{r}_i,\omega) = \frac{\mathrm{e}^{ikR}}{4\pi R}\left[\left(1 + \frac{ikR-1}{k^2R^2}\right)\mathbb{I} + \frac{3(1-ikR)-k^2R^2}{k^2R^2}\hat{\mathbf{R}}\otimes\hat{\mathbf{R}}\right] \tag{5.2}$$

where $\mathbb{I}$ is the identity matrix, $\mathbf{R} = \mathbf{r} - \mathbf{r}_i$, $R = |\mathbf{R}|$, and $\hat{\mathbf{R}} = \mathbf{R}/R$. Here the field arising from an external bath as considered in reference [115] has been neglected for simplicity and correspondence with the T-DDA [51]. Modeling a particle or subvolume as a point dipole requires that the electric field and dyadic Green's function are constant throughout the volume of each object, which in practice means that its size must be much smaller than the wavelengths and decay lengths of the electric fields under consideration [51]. The total

dipole moment is split into a fluctuating part due to fluctuating thermal currents and an induced part due to electric fields:

$$\mathbf{p}_i = \mathbf{p}_i^{(\mathrm{fl})} + \mathbf{p}_i^{(\mathrm{ind})} \tag{5.3}$$

where $\mathbf{p}(\mathbf{r}_i, \omega)$ is written as $\mathbf{p}_i$ for compactness.

At this point the many-body and T-DDA methods diverge, using different definitions for the fluctuating and induced dipole moments. The many-body method expresses $\mathbf{p}_i^{(\mathrm{ind,MB})} = \varepsilon_0 \alpha_i^{(\mathrm{d})} \mathbf{E}_i^{(\mathrm{exc})}$ with $\mathbf{E}_i^{(\mathrm{exc})}$ described by Equation (5.1) in terms of the *exciting* field or the fields from all other dipoles as [115]

$$\mathbf{p}_i^{(\mathrm{ind,MB})} = \alpha_i^{(\mathrm{d})} \frac{k^2}{\varepsilon_m} \sum_{j \neq i} \mathbb{G}_{ij}^{(0)} \cdot \mathbf{p}_j \tag{5.4}$$

where the summation runs over all dipoles *except* the ith dipole, and $\alpha_i^{(\mathrm{d})}$ is the dressed polarizability, which accounts for radiation damping and is written as

$$\alpha_i^{(\mathrm{d})} = \left(\frac{1}{\alpha_i^{(\mathrm{CM})}} - \frac{ik^3}{6\pi\varepsilon_m} \right)^{-1} \tag{5.5}$$

Here, $\alpha_i^{(\mathrm{CM})}$ is the Clausius-Mossotti polarizability defined as

$$\alpha_i^{(\mathrm{CM})} = 3\varepsilon_m V_i \frac{\varepsilon_i - \varepsilon_m}{\varepsilon_i + 2\varepsilon_m} \tag{5.6}$$

where V_i is the volume of the ith particle or subvolume and ε_i is its complex relative permittivity. Equation (5.5) is specific to spherical or cubical volumes, and Equation (5.6) is for spherical volumes, but these may be modified for other shapes [78, 199]. The definition in Equation (5.4) is consistent with the coupled dipole method commonly used in the discrete dipole approximation for electromagnetic scattering calculations [97, 107]. It is important to note, however, that $\mathbf{p}_i^{(\mathrm{ind,MB})}$ does not include the parts of the dipole moment due to its own thermal fluctuations nor due to the fields produced by its own thermal fluctuations. These parts must, therefore, both be included in $\mathbf{p}_i^{(\mathrm{fl})}$ in order to obtain the correct total dipole moment $\mathbf{p}_i$.

The T-DDA on the other hand expresses $\mathbf{p}_i^{(\mathrm{ind,TDDA})} = \varepsilon_0 \alpha_i^{(0)} \mathbf{E}_i^{(\mathrm{act})}$ with $\mathbf{E}_i^{(\mathrm{act})}$ described by Equation (5.1) in terms of the *actual* total field at the ith dipole as [51]

$$\mathbf{p}_i^{(\mathrm{ind,TDDA})} = \alpha_i^{(0)} \frac{k^2}{\varepsilon_m} \sum_j \mathbb{G}_{ij}^{(0)} \cdot \mathbf{p}_j \tag{5.7}$$

where the summation runs over all dipoles *including* the ith dipole, and $\alpha_i^{(0)}$ is the bare polarizability defined as

$$\alpha_i^{(0)} = V_i(\varepsilon_i - \varepsilon_m) \tag{5.8}$$

A derivation of Equation (5.7) from Maxwell's equations is provided in Appendix C.1 for completeness. This definition is consistent with the method of moments [107]. Since $\mathbf{p}_i^{(\mathrm{ind,TDDA})}$ includes the effects of all fields on the dipole moment, including those produced by its own fluctuating currents, the $\mathbf{p}_i^{(\mathrm{fl})}$ term must only include the part directly

due to fluctuating currents in order to obtain the correct total dipole moment $\mathbf{p}_i$. This allows a more straightforward use of the fluctuation-dissipation theorem, as will be seen in the following sections. The remainder of this derivation will use the T-DDA's definition of the induced dipole moment, but the same final equation for heat transfer derived via the many-body method will still be recovered.

5.1.2 Expressions for Total Dipole Moments and Electric Fields

Combining Equations (5.3) and (5.7) yields a set of N self-consistent equations:

$$\mathbf{p}_i = \mathbf{p}_i^{(\mathrm{fl})} + \alpha_i^{(0)} \frac{k^2}{\varepsilon_m} \sum_j \mathbb{G}_{ij}^{(0)} \cdot \mathbf{p}_j \tag{5.9}$$

When $j = i$, the dyadic Green's function has a singularity, so this value must be treated separately. $\mathbb{G}_{ii}^{(0)}$ may be evaluated for V_i using the principal value method, assuming V_i is spherical or may approximated by a sphere of equivalent volume [51, 199, 200]. For a spherical or cubical volume, this results in

$$\mathbb{G}_{ii}^{(0)} = \left(-\frac{1}{3V_i k^2} + \frac{ik}{6\pi} \right) \mathbb{I} \tag{5.10}$$

Separating the $\mathbb{G}_{ii}^{(0)}$ term from the summation in Equation (5.9) and rearranging yields

$$\left(\frac{1}{\alpha_i^{(0)}} - \frac{k^2}{\varepsilon_m} \mathbb{G}_{ii}^{(0)} \right) \mathbf{p}_i = \frac{1}{\alpha_i^{(0)}} \mathbf{p}_i^{(\mathrm{fl})} + \frac{k^2}{\varepsilon_m} \sum_{j \neq i} \mathbb{G}_{ij}^{(0)} \cdot \mathbf{p}_j \tag{5.11}$$

The term in parenthesis on the left-hand side is identical to the inverse of the dressed polarizability [116] (given by Equations (5.5) and (5.6) for spherical volumes):

$$\frac{1}{\alpha_i^{(\mathrm{d})}} = \frac{1}{\alpha_i^{(0)}} - \frac{k^2}{\varepsilon_m}\mathbb{G}_{ii}^{(0)} \tag{5.12}$$

Equation (5.11) is the same as the main equation derived in the T-DDA [51], except with a different form of the dressed polarizability due to a different treatment of $\mathbb{G}_{ii}^{(0)}$.

The approach of the many-body method [115] is now followed to find explicit expressions for $\mathbf{p}_i$ and $\mathbf{E}_i$ in terms of the fluctuating parts of the dipole moments. Rearranging Equation (5.11) with the use of Equation (5.12) and writing it in matrix form results in the relation

$$\begin{pmatrix} \mathbf{p}_1 \\ \vdots \\ \mathbf{p}_N \end{pmatrix} = \mathbb{A}^{-1} \begin{pmatrix} \frac{\alpha_1^{(\mathrm{d})}}{\alpha_1^{(0)}}\mathbf{p}_1^{(\mathrm{fl})} \\ \vdots \\ \frac{\alpha_N^{(\mathrm{d})}}{\alpha_N^{(0)}}\mathbf{p}_N^{(\mathrm{fl})} \end{pmatrix} \tag{5.13}$$

This equation is similar to that derived in reference [115] with the same $3N \times 3N$ interaction matrix, but the vector of fluctuating thermal currents has additional $\alpha_j^{(\mathrm{d})}/\alpha_j^{(0)}$ coefficients here. $\mathbb{A}$ is defined by its N^2 3×3 submatrices with $i, j = 1 \ldots N$:

$$\mathbb{A}_{ij} = \delta_{ij}\mathbb{I} - \left(1 - \delta_{ij}\right)\alpha_i^{(\mathrm{d})}\frac{k^2}{\varepsilon_m}\mathbb{G}_{ij}^{(0)} \tag{5.14}$$

where δ_{ij} is the Kronecker delta function. Inserting Equation (5.13) into Equation (5.1) provides an expression for the local fields:

$$\begin{pmatrix} \mathbf{E}_1 \\ \vdots \\ \mathbf{E}_N \end{pmatrix} = \mathbb{D}\mathbb{A}^{-1} \begin{pmatrix} \frac{\alpha_1^{(\mathrm{d})}}{\alpha_1^{(0)}} \mathbf{p}_1^{(\mathrm{fl})} \\ \vdots \\ \frac{\alpha_N^{(\mathrm{d})}}{\alpha_N^{(0)}} \mathbf{p}_N^{(\mathrm{fl})} \end{pmatrix} \tag{5.15}$$

which once again is similar to that derived in reference [115] except for the coefficients on $\mathbf{p}_j^{(\mathrm{fl})}$. $\mathbb{D}$ is defined by its submatrices as

$$\mathbb{D}_{ij} = \frac{k^2}{\varepsilon_m \varepsilon_0} \mathbb{G}_{ij}^{(0)} \tag{5.16}$$

As will be seen later, it is helpful to express $\mathbb{D}\mathbb{A}^{-1}$ in the same form as reference [115]:

$$\begin{aligned} \mathbb{D}\mathbb{A}^{-1} = (\mathbb{B}\mathbb{A}^{-1} - \mathbb{C}^{-1}), \mathbb{B}_{ij} &= \delta_{ij} \left(\frac{1}{\varepsilon_0 \alpha_i^{(\mathrm{d})}} \mathbb{I} + \frac{k^2}{\varepsilon_m \varepsilon_0} \mathbb{G}_{ii}^{(0)} \right), \mathbb{C}_{ij} \\ &= \delta_{ij} \varepsilon_0 \alpha_i^{(\mathrm{d})} \mathbb{I} \end{aligned} \tag{5.17}$$

5.1.3 Energy Exchange and the Fluctuation-Dissipation Theorem

With the expressions for total dipole moment and local electric field in hand, the energy exchange can now be examined. Using the convention for the Fourier transform $f(t) = \int \frac{d\omega}{2\pi} f(\omega) \mathrm{e}^{-i\omega t}$, the power absorbed by the ith dipole in the time domain is [53, 115]

$$Q_i(t, T_1, \ldots, T_N) = 2\int_0^\infty \frac{d\omega}{2\pi}\omega \int_0^\infty \frac{d\omega'}{2\pi} \mathrm{Im}\left[\langle \mathbf{p}_i(\omega) \cdot \mathbf{E}_i^*(\omega')\rangle \mathrm{e}^{-i(\omega-\omega')t}\right] \quad (5.18)$$

where T_i is the temperature of the ith dipole, and the angled brackets represent the ensemble average. Focusing on this correlation function and inserting Equations (5.13) and (5.15) yields

$$\begin{aligned} &\langle \mathbf{p}_i(\omega) \cdot \mathbf{E}_i^*(\omega')\rangle \\ &= \sum_\beta \sum_{jj'} \sum_{\gamma\gamma'} \Bigg[(A^{-1})_{ij,\beta\gamma} (BA^{-1} \\ &- C^{-1})'^*_{ij',\beta\gamma'} \frac{\alpha_j^{(\mathrm{d})} \alpha_{j'}'^{(\mathrm{d})*}}{\alpha_j^{(0)} \alpha_{j'}'^{(0)*}} \langle p_{j,\gamma}^{(\mathrm{fl})} p_{j',\gamma'}'^{(\mathrm{fl})*} \rangle \Bigg] \end{aligned} \quad (5.19)$$

Here the primes indicate that the variables are a function of ω', and the Greek subscripts are indices 1, 2, 3 representing the Cartesian components of vector quantities. For example, $(A^{-1})_{ij,\beta\gamma}$ is the $[\beta, \gamma]$ element of the 3 × 3 matrix $\mathbb{A}_{ij}^{-1}$. The correlation function $\langle p_{j,\gamma}^{(\mathrm{fl})} p_{j',\gamma'}'^{(\mathrm{fl})*} \rangle$ is provided by the fluctuation-dissipation theorem [15, 24, 195-197]. For a dipole moment with a polarizability defined by $\mathbf{p}_j = \varepsilon_0 \alpha_j \mathbf{E}_j$, the theorem is [15, 197]

$$\langle p_{j,\gamma}^{(\mathrm{fl})}(\omega) p_{j',\gamma'}^{(\mathrm{fl})*}(\omega')\rangle = 4\pi\hbar\varepsilon_0 f^{(\mathrm{BE})}\left(\omega, T_j\right) \mathrm{Im}\left(\alpha_j\right) \delta_{jj'} \delta_{\gamma\gamma'} \delta(\omega - \omega') \quad (5.20)$$

where $f^{(\mathrm{BE})}\left(\omega, T_j\right)$ is the Bose-Einstein distribution function. However, care must be taken to use this relation appropriately. In the present case, the bare polarizability $\alpha_j^{(0)}$ satisfies $\mathbf{p}_j = \varepsilon_0 \alpha_j \mathbf{E}_j$ for α_j, and $\mathbf{p}_j^{(\mathrm{fl})}$ was defined to only include the part of the dipole moment

due to thermal fluctuations. This means $\alpha_j^{(0)}$ may be used directly for the polarizability in the fluctuation-dissipation theorem. Equation (5.20) used with $\alpha_j^{(0)}$ may also be derived directly from the fluctuation-dissipation theorem for thermal currents as done in reference [51] and shown in Appendix C.1. In the many-body theory [115], $\mathbf{p}_j^{(\mathrm{fl})}$ was defined to include the parts of the dipole moment due to fluctuating thermal currents as well as the fields produced by those fluctuations, as described in Section 5.1.1. Furthermore, the many-body derivation uses only the dressed polarizability, which does not satisfy $\mathbf{p}_j = \varepsilon_0 \alpha_j \mathbf{E}_j$ because $\mathbf{E}_j$ is the actual field instead of the exciting field. For these reasons, the appropriate fluctuation-dissipation theorem in the many-body approach must instead be derived by considering the fields emitted by a single dipole in equilibrium with a thermal bath, as described by Messina *et al.* [115] and Sääskilahti *et al.* [116]. The resulting fluctuation-dissipation theorem contains a reduced absorption factor $\chi_j = \mathrm{Im}\left(\alpha_j^{(\mathrm{d})}\right) - \frac{k^3}{6\pi\varepsilon_m}\left|\alpha_j^{(\mathrm{d})}\right|^2$ used in place of $\mathrm{Im}(\alpha_j)$ in Equation (5.20). This factor was first derived by Manjavacas and de Abajo [197, 201]. It is important to stress that this factor is not inherent to the fluctuation-dissipation theorem but arises due to the definition of the fluctuating and induced dipole moments. That the bare polarizability may instead be used directly with the same results (if $\mathbf{p}_j^{(\mathrm{ind})}$ and $\mathbf{p}_j^{(\mathrm{fl})}$ are defined appropriately) is a key result.

Using the fluctuation-dissipation theorem with $\alpha_j^{(0)}$ as the polarizability, applying the definitions of $\mathbb{B}$ and $\mathbb{C}$ from Equation (5.17), and reverting to matrix notation, Equation (5.19) can be rewritten as

$$\begin{aligned}\langle \mathbf{p}_i(\omega)\cdot\mathbf{E}_i^*(\omega')\rangle &= 4\pi\hbar\varepsilon_0\delta(\omega-\omega')\\ &\times\left[\sum_j \frac{\left|\alpha_j^{(\mathrm{d})}\right|^2 \mathrm{Im}\left(\alpha_j^{(0)}\right)}{\left|\alpha_j^{(0)}\right|^2} f^{(\mathrm{BE})}\left(\omega,T_j\right)\right.\\ &\times\left(\frac{1}{\varepsilon_0\alpha_i^{(\mathrm{d})}}+\frac{k^2}{\varepsilon_m\varepsilon_0}\mathbb{G}_{ii}^{(0)}\right)^* \mathrm{Tr}\left(\mathbb{A}_{ij}^{-1}\mathbb{A}_{ij}^{-1\dagger}\right)\\ &\left.-\frac{\left|\alpha_i^{(\mathrm{d})}\right|^2 \mathrm{Im}\left(\alpha_i^{(0)}\right)}{\left|\alpha_i^{(0)}\right|^2} f^{(\mathrm{BE})}(\omega,T_i)\frac{1}{\varepsilon_0\alpha_i^{(\mathrm{d})*}}\mathrm{Tr}(\mathbb{A}_{ii}^{-1})\right]\end{aligned} \tag{5.21}$$

where the $\delta(\omega-\omega')$ function has been used to eliminate the dependence on ω' but is still retained here as it affects other parts of Equation (5.18). Only the imaginary part is important as shown in Equation (5.18). The integrand can be simplified by using the definition of dressed polarizability from Equation (5.12) and becomes

$$\begin{aligned}\mathrm{Im}\left[\langle \mathbf{p}_i(\omega)\cdot\mathbf{E}_i^*(\omega')\rangle \mathrm{e}^{-i(\omega-\omega')t}\right] &= 4\pi\hbar\delta(\omega-\omega')\\ &\times\left[\sum_j \frac{\left|\alpha_j^{(\mathrm{d})}\right|^2 \mathrm{Im}\left(\alpha_j^{(0)}\right)}{\left|\alpha_j^{(0)}\right|^2}\frac{\mathrm{Im}\left(\alpha_i^{(0)}\right)}{\left|\alpha_i^{(0)}\right|^2} f^{(\mathrm{BE})}\left(\omega,T_j\right)\mathrm{Tr}\left(\mathbb{A}_{ij}^{-1}\mathbb{A}_{ij}^{-1\dagger}\right)\right.\\ &\left.-\frac{\left|\alpha_i^{(\mathrm{d})}\right|^2 \mathrm{Im}\left(\alpha_i^{(0)}\right)}{\left|\alpha_i^{(0)}\right|^2}\frac{\mathrm{Im}\left(\alpha_i^{(\mathrm{d})}\right)}{\left|\alpha_i^{(\mathrm{d})}\right|^2} f^{(\mathrm{BE})}(\omega,T_i)\mathrm{Tr}(\mathbb{A}_{ii}^{-1})\right]\end{aligned} \tag{5.22}$$

At thermal equilibrium when all temperatures are equal, the net power absorbed must be zero for each frequency. This provides the condition [115]

$$0 = \sum_j \frac{\left|\alpha_j^{(\mathrm{d})}\right|^2 \mathrm{Im}\left(\alpha_j^{(0)}\right)}{\left|\alpha_j^{(0)}\right|^2} \frac{\mathrm{Im}\left(\alpha_i^{(0)}\right)}{\left|\alpha_i^{(0)}\right|^2} \mathrm{Tr}\left(\mathbb{A}_{ij}^{-1}\mathbb{A}_{ij}^{-1\dagger}\right) - \frac{\left|\alpha_i^{(\mathrm{d})}\right|^2 \mathrm{Im}\left(\alpha_i^{(0)}\right)}{\left|\alpha_i^{(0)}\right|^2} \frac{\mathrm{Im}\left(\alpha_i^{(\mathrm{d})}\right)}{\left|\alpha_i^{(\mathrm{d})}\right|^2} \mathrm{Tr}\left(\mathbb{A}_{ii}^{-1}\right) \tag{5.23}$$

Equation (5.23) is used to arrive at a final expression for the net radiation heat transfer to the ith dipole in terms of the exchanges with all other dipoles:

$$Q_i(t, T_1, \ldots, T_N) = \int_0^\infty \frac{d\omega}{2\pi} \hbar\omega \sum_{j \neq i} \frac{4\left|\alpha_j^{(\mathrm{d})}\right|^2 \mathrm{Im}\left(\alpha_j^{(0)}\right) \mathrm{Im}\left(\alpha_i^{(0)}\right)}{\left|\alpha_j^{(0)}\right|^2 \left|\alpha_i^{(0)}\right|^2} \mathrm{Tr}\left(\mathbb{A}_{ij}^{-1}\mathbb{A}_{ij}^{-1\dagger}\right) f_{ji}^{(\mathrm{BE})}(\omega) \tag{5.24}$$

where $f_{ji}^{(\mathrm{BE})}(\omega) = f^{(\mathrm{BE})}\left(\omega, T_j\right) - f^{(\mathrm{BE})}(\omega, T_i)$.

As expected, Equation (5.24) is very similar in form to the net heat transfer equation derived in the many-body theory [115] because their procedures have been followed for the latter part of the derivation. An advantage of Equation (5.24), however, is that it does not prescribe a treatment to correct for radiation damping since it is written in terms of the dressed polarizability. To demonstrate that this result is identical to that in reference [115], the relation of the reduced absorption factor to the bare and dressed polarizabilities can be used:

$$\chi_i = \frac{\left|\alpha_i^{(\mathrm{d})}\right|^2 \mathrm{Im}\left(\alpha_i^{(0)}\right)}{\left|\alpha_i^{(0)}\right|^2} \tag{5.25}$$

A proof of the equivalence of Equation (5.25) to the reduced absorption factor used in the many-body theory [115] is provided in Appendix C.3. Equation (5.25) allows Equation (5.24) to be rewritten as

$$Q_i(t, T_1, \ldots, T_N) = \int_0^\infty \frac{d\omega}{2\pi} \hbar\omega \sum_{j \neq i} \frac{4\chi_i \chi_j}{\left|\alpha_i^{(\mathrm{d})}\right|^2} \mathrm{Tr}\left(\mathbb{A}_{ij}^{-1} \mathbb{A}_{ij}^{-1\dagger}\right) f_{ji}^{(\mathrm{BE})}(\omega) \tag{5.26}$$

When the dipoles are near thermal equilibrium, this may be written as the thermal conductance between two particles in a Landauer-like form [126]:

$$G_{ij}(T) = \int_0^\infty \frac{d\omega}{2\pi} \frac{\partial \Theta(\omega, T)}{\partial T} \mathcal{T}_{ij}(\omega) \tag{5.27}$$

where $\Theta(\omega, T_i) = \hbar\omega / f^{(\mathrm{BE})}(\omega, T_i)$ is the mean energy of a harmonic oscillator and the transmission coefficient $\mathcal{T}_{ij}(\omega)$ is

$$\mathcal{T}_{ij}(\omega) = \frac{4\chi_i \chi_j}{\left|\alpha_i^{(\mathrm{d})}\right|^2} \mathrm{Tr}\left(\mathbb{A}_{ij}^{-1} \mathbb{A}_{ij}^{-1\dagger}\right) \tag{5.28}$$

This is the same equation for many-dipole radiation as obtained in the many-body method [115], but it was derived using the definitions of fluctuating and induced dipole moments used in the T-DDA [51], demonstrating their mathematical equivalence. Furthermore, the derivation was performed with a straightforward use of the fluctuation-dissipation theorem

without the need to derive the correlation function from the interactions of a dipole with a thermal bath. Although the choice of methodology may be a purely formal one, this derivation highlights some of the subtleties encountered when considering thermal-electromagnetic interactions, and it should clarify appropriate uses of the fluctuation-dissipation theorem in future research.

5.2 Radiative Thermal Conductivity of Particle Arrays

5.2.1 Radiative Thermal Conductivity Model

Although the previous equations provide energy absorption by a dipole or exchanges between pairs of dipoles, these quantities alone may not be particularly useful for very large systems containing many nanostructures, such as packed nanoparticle beds or nanofluids. In these cases, it is often desirable to compare the radiative contribution with the phonon contribution to the thermal transport [132]. When the systems are large enough that the spatial dimensions exceed modal propagation lengths, the thermal transport is diffusive and the most commonly used property is the thermal conductivity.

Consider a collection of nanoparticles modeled as point dipoles at locations $\mathbf{r}_i$ with the same assumptions as discussed in Section 5.1. An example of a portion of an ordered three-dimensional array is shown in Figure 5.1, but the particles may also be disordered. All particles are assumed to be near thermal equilibrium such that the thermal conductance between any two particles may be calculated with Equation (5.27). A small, linear temperature gradient is assumed to exist in the direction of interest for mathematical purposes, which is taken as the x direction here. Note that if the particles are disordered or anisotropic, then different directions may exhibit different radiative thermal conductivities.

In the center of the particle array, perpendicular to the temperature gradient, a fictitious plane is constructed to separate the array into two halves.

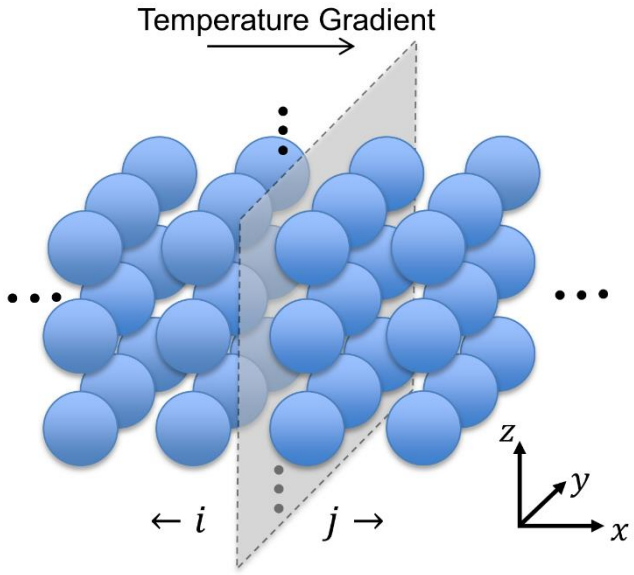

Figure 5.1. Example of an ordered array of nanoparticles for the calculation of diffusive radiative thermal conductivity.

In this scenario, the total heat transfer crossing the plane can be written in terms of the thermal conductance between all pairs of particles on opposing sides of the plane as

$$Q_{tot} = \sum_i \sum_j G_{ij}(T) \frac{dT}{dx} (\mathbf{r}_j - \mathbf{r}_i) \cdot \hat{x} \tag{5.29}$$

where the summation over i runs over one side of the plane, the summation over j runs over the other side, T is the equilibrium temperature of all the particles, and dT/dx is the temperature gradient. The $dT/dx\ (\mathbf{r}_j - \mathbf{r}_i) \cdot \hat{x}$ term provides a mathematical temperature difference which scales the thermal conductance appropriately with separation distance. Using Fourier's law $Q_{tot} = \kappa\ A_c\ dT/dx$, the effective radiative thermal conductivity is

$$\kappa(T) = \frac{1}{A_c}\sum_i \sum_j G_{ij}(T)\left(\mathbf{r}_j - \mathbf{r}_i\right) \cdot \hat{x} \tag{5.30}$$

where A_c is the cross-sectional area of the array perpendicular to the temperature gradient. This equation for thermal conductivity has two important limitations. First, the assumption that all particles are near thermal equilibrium means that this approach is not valid for large temperature gradients through the array. Due to both the nonlinear nature of thermal radiation with temperature and superdiffusive effects that can exist for polaritonic particles [126], large temperature differences result in nonlinear temperature gradients. Second, the placement of the separating plane and direction of the temperature gradient may affect the results if there is significant spatial variation in particle arrangements or properties. For example, if the particles are closely packed on the left side of the array and become very sparse towards the right side, the arrangement is highly asymmetrical, and results will be influenced by the location of the plane. For this reason, the approach is best suited to ordered arrays or disordered arrays with a consistent packing density.

Because the bulk radiative thermal conductivity is sought, a sufficient number of particles must be included in the array to be representative of the larger system. Contributions to the radiative thermal conductivity from individual pairs of particles decrease as the distance between them increases. This allows one to begin with a small number of particles on each side of the plane and add additional particles while repeating the thermal conductivity calculation. As particles are added in all directions, the influence of boundary effects becomes smaller and the array becomes more representative of a larger system, causing the calculation to eventually converge. This process is simpler, of course,

for an ordered array; for a disordered array, a representative particle arrangement must be used, and multiple representative arrangements should be checked.

One remaining important point is that for certain ordered arrays, symmetry may be exploited to reduce the computational burden. For example, if all particles are isotropic, consist of the same material, and are organized in an ordered cubic structure as illustrated in Figure 5.1, then the thermal conductance calculation in Equation (5.30) would be highly redundant. By recognizing repeated terms and lumping them with an appropriate multiplicative factor, the number of terms in the double summation can be substantially reduced.

5.2.2 Materials and Geometry

Arrays of spherical SiC and SiO_2 nanoparticles of radius $a = 25$ nm are examined in a transparent background medium of $\varepsilon_m = 4$ for SiC and $\varepsilon_m = 1$ for SiO_2. The background permittivity for SiC is chosen because this maximizes electromagnetic coupling as shown in reference [202] and discussed further in Chapter 6. Additionally, it has been shown that under these conditions with a center-to-center spacing of $d = 3a$, SiC chains support propagating surface polaritons that dominate the heat transfer, while SiO_2 chains do not support these propagating surface modes [202, 203]. This difference is discussed further in Chapter 6, and it allows a comparison between the two systems to investigate the role of propagating modes in many-particle arrays. The particles are at temperature $T = 500$ K. The relative permittivity of SiC is described with a Lorentz model [144]:

$$\varepsilon(\omega) = \varepsilon_\infty \left(1 + \frac{\omega_{LO}^2 - \omega_{TO}^2}{\omega_{TO}^2 - \omega^2 - i\omega\Gamma}\right) \tag{5.31}$$

where $\varepsilon_\infty = 6.7$, $\omega_{LO} = 1.82\times10^{14}$ rad s^{-1}, $\omega_{TO} = 1.49\times10^{14}$ rad s^{-1}, and $\Gamma = 8.92\times10^{11}$ rad s^{-1}. The relative permittivity of SiO_2 is taken from Palik's data [144] with piecewise cubic interpolation. The geometries examined are ordered one-, two-, and three-dimensional arrays of particles in a cubic lattice structure, as well as one-dimensional disordered chains. For the disordered chains, the particles are randomly perturbed in the $\hat{z}$ direction (assuming the ordered chain lies on the x axis) by a distance on the interval $[-L_p, L_p]$ where L_p is randomly selected as $0 \leq L_p \leq d$. This allows the generation of many chain arrangements with varying degrees of disorder. These geometries are illustrated in Figure 5.2. In order to obtain results representative of a larger system, particles are added repeatedly to the arrays and the thermal conductivity is calculated until a 1% convergence criterion is reached.

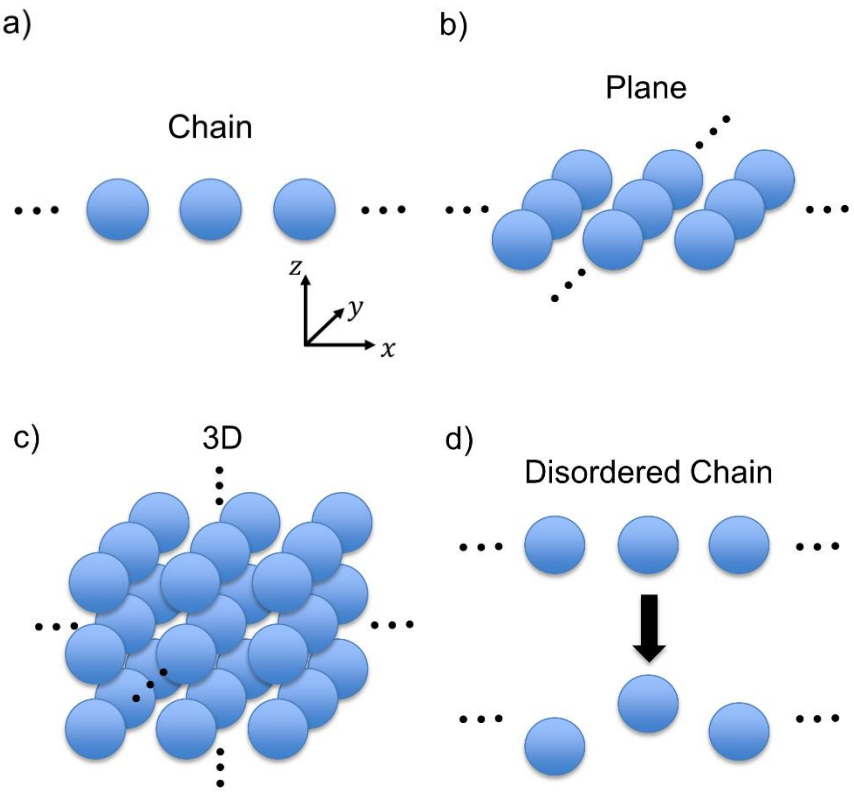

Figure 5.2. Schematics of ordered (a) one-dimensional, (b) two-dimensional, and (c) three-dimensional arrays of nanoparticles as well as (d) disordered chains.

5.2.3 Comparison to Exact Solution for Ordered Chains

To validate the many-dipole radiation methodology and to investigate its regime of validity, the radiative thermal conductivity of ordered SiO_2 particle chains with varying d is compared to the exact solution derived by Czapla and Narayanaswamy [33]. Their solution is based on numerically exact vector spherical wave expansions of the dyadic Green's functions for particles in a linear chain. Their code is used to calculate the thermal conductance between every pair of particles in the chain, and these conductance values are transformed to a radiative thermal conductivity as described in Section 5.2.1. For spacings $d < 3a$, a chain of 14 particles is used based on convergence at the minimum spacing of $d = 2a$. For spacings $d \geq 3a$, a chain of 10 particles is used based on convergence at a

spacing of $d = 3a$. For these calculations, the area in the thermal conductivity calculation is taken as $A_c = \pi a^2$. The resulting radiative thermal conductivities are shown in Figure 5.3.

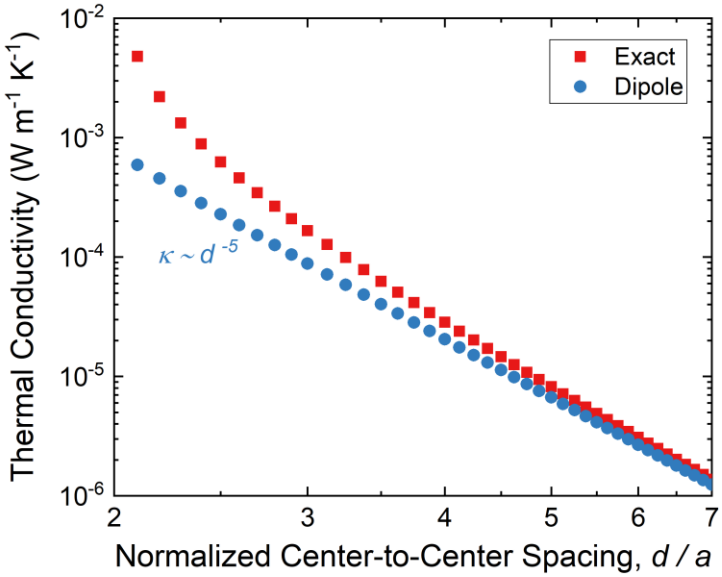

Figure 5.3. Radiative thermal conductivity calculated via the many-dipole method and the exact solution.

For the dipole method, a typical monomial dependence on the spacing is observed of $\kappa \sim d^{-n}$ with $n = 5$. This is consistent with the thermal conductance for dipole-dipole interactions [31] multiplied by distance when obtaining thermal conductivity. The dipole method and exact solution agree well for large separation distances, but the dipole method greatly underpredicts the exact solution at small spacings. This is a well-known effect, and typically researchers consider the dipole approximation to be valid for $d \gtrsim 3a$ [31, 78, 83, 92]. The comparison of the exact and many-dipole methods provides two important results: it validates the theoretical formalism of the many-body radiative heat transfer theory, and it demonstrates that the dipole approximation may be used as a conservative baseline estimate of thermal radiation among closely spaced particles. The results from the exact

method also show that near-field thermal radiation could be a significant contributor to thermal transport among very closely-spaced or packed particle arrays; for the case shown in Figure 5.3, the exact radiative thermal conductivity is approaching values similar to those expected for phonon conduction between particles in contact [9].

5.2.4 Ordered Particle Arrays

For a spacing of $d = 3a$, the spectral radiative thermal conductivity of SiO_2 and SiC particles in ordered chain, plane, and three-dimensional arrays is calculated, and the results are shown in Figure 5.4. 10 particles for the SiO_2 chain and 22 particles for the SiC chain are used based on a 1% convergence criterion. These dimensions are extended to the plane and three-dimensional systems, resulting in $10^2 = 100$ ($22^2 = 484$) particles for the plane and $10^3 = 1{,}000$ ($22^3 = 10{,}648$) particles for the three-dimensional SiO_2 (SiC) cases. To fairly compare the three different geometries, cross-sectional areas are used for the radiative thermal conductivity in each calculation of $A_c = N_y N_z d^2$ where N_y and N_z are the lengths of the array in number of particles in the y and z directions. This results in lower thermal conductivities for the plane and chain than would be obtained considering the area as the physical extent of the system, but it allows the different cases to be compared directly to each other without differences due to the area.

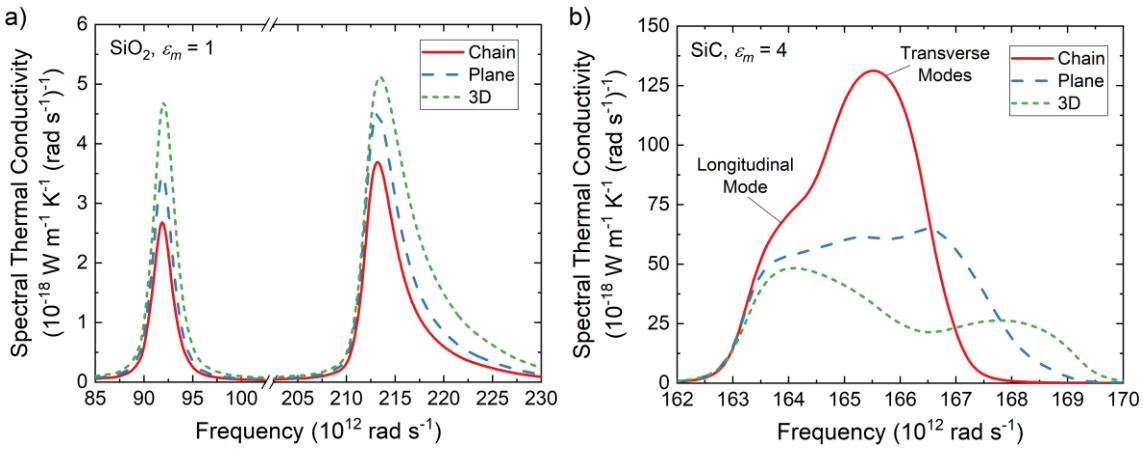

Figure 5.4. Spectral radiative thermal conductivity of ordered chains, planes, and three-dimensional arrays of (a) SiO_2 particles and (b) SiC particles.

For the SiO_2 particles, an increase in radiative thermal conductivity is observed as dimensions are added to the particle chain. On the other hand, the SiC particles show a decrease in radiative thermal conductivity as dimensions are added to the array. These results reflect the predicted trends for thermal emission from ordered particle arrays [202], which will be discussed further in Chapter 6. The dissimilar behaviors are likely due to the existence or absence of propagating surface modes in the particle arrays. The SiO_2 particles do not support propagating modes [202, 203], so the radiative thermal transport is due to the summation of particle-particle interactions in the array. Adding dimensions to the array increases the number of interactions and so increases the total thermal transport. The SiC particles do support propagating modes, which for a chain include a longitudinal mode corresponding to the shoulder in Figure 5.4(b) and two degenerate transverse modes corresponding to the peak in Fig. Figure 5.4 (b) [202, 203]. As dimensions are added to the SiC chain, transverse polarization can now couple to adjacent particles in that direction, creating a mode propagating perpendicular to the temperature gradient which is not a strong contributor to the radiative thermal conductivity. This may explain why the contribution of

the longitudinal mode is relatively invariant while those of the transverse modes sharply decrease in Figure 5.4(b) with increasing number of dimensions.

The results in Figure 5.4 also have important implications for the general understanding of many-body effects in thermal radiation. Researchers have previously found that collective behavior tends to enhance thermal transport for systems containing a few particles [114, 119] and to either enhance or suppress thermal transport for larger systems of particles depending on their number, positions, and optical properties [121]. The results shown here are consistent with the latter finding but provide physical insight into one mechanism by which many-body effects enhance or suppress thermal radiation. The ordered SiC arrays considered here enable coherence of the fluctuating thermal fields expressed through the collective behavior of propagating SPhPs, which is one reason why the spectral thermal conductivities are so much higher than for SiO_2. These modes can clearly be disrupted by controlling the placement of neighboring particles as shown in Figure 5.4(b). Other methods of disrupting the propagating modes are by introducing disorder, which is examined in Section 5.2.5, and by controlling the interparticle spacing, which is shown in Figure 5.5. Here the total radiative thermal conductivity of the SiO_2 and SiC systems as is plotted as a function of the normalized center-to-center spacing d/a. For $d/a \geq 3$, the same numbers of particles are used as described for Figure 5.4. For $d/a < 3$ a 1% convergence criteria is used for a chain at $d = 2a$ to obtain 14 (62) particles in a chain, $14^2 = 196$ ($62^2 = 3{,}844$) particles in a chain, and $14^3 = 2{,}744$ ($62^3 = 238{,}328$) particles in a three-dimensional array for the SiO_2 (SiC) cases. It should be noted that the dipole approximation used here is expected to underpredict the thermal conductivity for $d/a < 3$

(indicated by the gray shaded region), as discussed in Section 5.2.3. As before a cross-sectional area of $A_c = N_y N_z d^2$ is used for all cases for fair comparison across geometries.

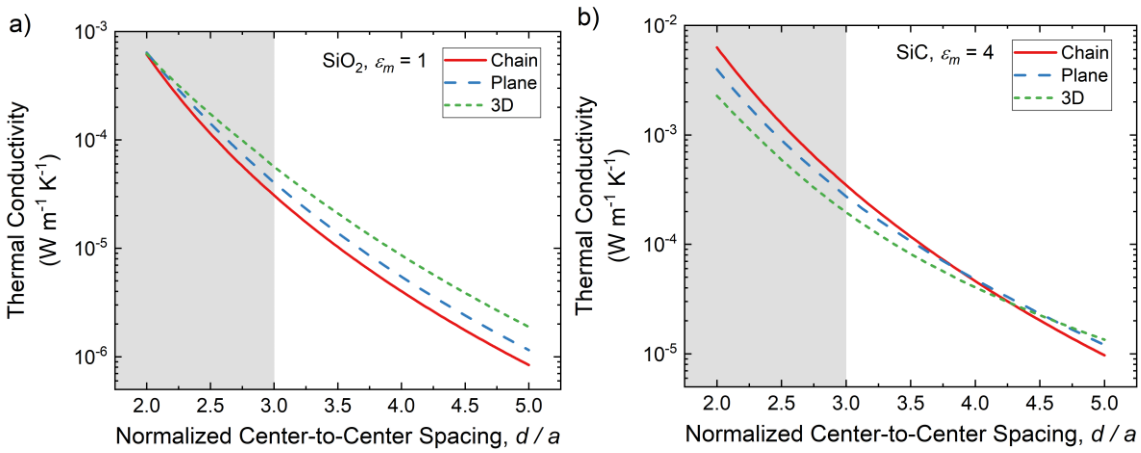

Figure 5.5. Dependence of radiative thermal conductivity on spacing for (a) SiO_2 particles and (b) SiC particles in three different geometric arrangements.

At a spacing $d = 3a$, the total thermal conductivities reflect the differences between Figure 5.4(a) and (b), with the highest κ for SiO_2 being the three-dimensional case and the highest κ for SiC being the chain case. As the spacing changes, however, the thermal conductivities for the different geometries become the same at about $d = 2a$ for SiO_2 and about $d = 4.25a$ for SiC. At larger spacings for SiC, the relative values of κ switch for different geometries, with the highest being a three-dimensional array and the lowest being a chain. This change is likely due to a shift from collective, propagating modes being the dominant heat carriers to individual particle-particle exchanges being the dominant heat transfer mechanism. At larger spacing the particles cannot couple as strongly, reducing the contributions from propagating modes. Similarly for SiO_2, propagating modes are not supported at most spacings but begin to emerge as the particles are brought close to contact.

These results reinforce the finding that many-body effects may enhance or suppress thermal radiation, but they are strongly dependent on the geometry of the particle array.

5.2.5 Disordered Particle Arrays

Although only ordered particle arrays have been examined so far, in practice these are more difficult to assemble than disordered particle arrays. Disordered arrays are also more challenging to analyze, as they lack the symmetry of ordered arrays and additional steps are needed to determine realistic packing arrangements [204]. Nevertheless, the effect of disorder on radiative thermal conductivity can begin to be examined with a simplified case for a chain of particles. Chains of SiO_2 and SiC particles are considered with spacing $d = 3a$, and disorder is introduced as illustrated in Figure 5.2(d) and described in Section 5.2.2. This spacing is selected for its reasonable accuracy with the dipole approximation. By only perturbing particles in a direction perpendicular to the axis chain, the separation distance between any two particles after randomization is $d \geq 3a$. The same numbers of particles are used as described for Figure 5.4, and a cross-sectional area of $A_c = d^2$ is used again to permit fair comparison to the ordered chain. For both material systems, 1,000 random chain arrangements are generated, and the resulting thermal conductivities are shown in Figure 5.6 as a fraction of the thermal conductivity of a perfectly ordered chain. These results are plotted as a function of the weighted standard deviation of the particle displacements, where the particles closer to the dividing plane (as depicted in Figure 5.1) are weighted more heavily than the particles further away. This type of weighting is used because the nearby particles have a much stronger influence on the calculated thermal conductivity, as shown by Equation (5.30). Because dipole contributions to the thermal conductivity tend to fall off as d^{-5} as demonstrated in Figure 5.3, the weighting function

selected for the standard deviation is $[d/(d + |\mathbf{r}_j - \mathbf{r}_p|)]^{-5}$, where $\mathbf{r}_p$ is the location of the particle next to the dividing plane and $\mathbf{r}_j$ is the location of a particle further from the dividing plane. This function provides a weight of 1 for the particles adjacent to the plane and lower weights for particles further away.

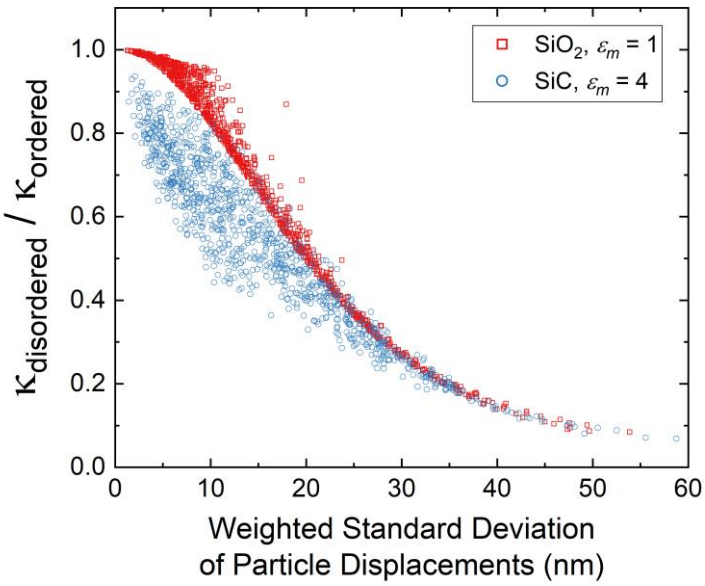

Figure 5.6. Thermal conductivities of disordered SiO_2 and SiC particle chains as a fraction of the thermal conductivity of an ordered chain.

An important observation from the results is that in no case does the thermal conductivity of a disordered chain exceed that of an ordered chain. Although this is not surprising, it clearly demonstrates that ordered arrays are the best-case scenario when seeking to maximize radiative thermal transport. For both materials, dipole-dipole interactions become weaker as disorder increases because individual pairs of particles are further apart. For SiC, an additional effect is the disruption of propagating modes; when the SiC particles are no longer regularly spaced, coherence of the thermal fields is lost. This causes a more substantial decrease in the thermal conductivity at low levels of disorder when compared to SiO_2. The results shown here are likely to extend to disorder in two- and

three-dimensional arrays of particles, especially for SiC or other materials that support propagating SPs. For material systems like SiO_2 where particle pair interactions dominate the heat transfer, additional multipolar effects or electromagnetic screening effects may exist for disordered two- and three-dimensional arrays, which is a topic for future investigation.

5.3 Systems Green's Function Approach

The equations developed in Section 5.1 require the calculation and inverse of a large interaction matrix, as discussed in the introduction to this chapter, which can become very computationally burdensome. In this section, the theoretical formalism is re-developed to find the system Green's functions $\mathbb{G}(\mathbf{r}_i, \mathbf{r}_j, \omega)$ between subvolumes or nanoparticles that account for all multiple scattering interactions. An equation of the form $\mathbb{A}\mathbb{G} = \mathbb{B}$ is developed where $\mathbb{A}$ and $\mathbb{B}$ are known, such that numerical methods may be used to find $\mathbb{G}$. Then, equations are derived for power absorbed by a subvolume or particle and conductance between sub-volumes or particles in terms of the system Green's functions.

5.3.1 Derivation of System Green's Functions

Consider N small, nonmagnetic dipoles of complex relative permittivity $\varepsilon(\omega)$ immersed in perfect dielectric (nonabsorbing, conductivity $\sigma = 0$) background medium of relative permittivity $\varepsilon_m(\omega)$. These dipoles may represent individual spherical nanoparticles provided they are much smaller than the characteristic thermal wavelength and their center-to-center spacing d is greater than or equal to three times their radius a [31, 78, 83, 92]. They also may be cubical or spherical subvolumes assembled to form

larger structures as has done in past implementations of the T-DDA [50, 51]. In either case, the electric field at a location $\mathbf{r}$ due to the ith dipole moment is

$$\mathbf{E}(\mathbf{r},\omega) = \mu_0\omega^2\mathbb{G}^{(0)}(\mathbf{r},\mathbf{r}_i,\omega)\cdot\mathbf{p}(\mathbf{r}_i,\omega) \tag{5.32}$$

Here $\mathbb{G}^{(0)}(\mathbf{r},\mathbf{r}',\omega)$ is the Green's function for the background medium and $\mathbf{p}(\mathbf{r}_i,\omega)$ is the total dipole moment. Using Equation (5.3) to split the dipole moment into fluctuating and induced parts and Equation (5.7) for the definition of the induced part, Equation (5.32) can be written as a sum of the fields at all dipoles and fluctuating parts of all dipole moments:

$$\mathbf{E}_i = \mu_0\omega^2\sum_j \mathbb{G}_{ij}^{(0)}\cdot\left(\varepsilon_0\alpha_j^{(0)}\mathbf{E}_j + \mathbf{p}_j^{(\mathrm{fl})}\right) \tag{5.33}$$

It is important to note that when $j = i$ the dyadic Green's function has a singularity and may be evaluated with the principal value method as discussed in Section 5.1.2.

It is assumed that there exist system Green's functions $\mathbb{G}_{ij}$ such that

$$\mathbf{E}_i = \mu_0\omega^2\sum_j \mathbb{G}_{ij}\cdot\mathbf{p}_j^{(\mathrm{fl})} \tag{5.34}$$

Equation (5.34) is used to eliminate the electric field terms in Equation (5.33). Writing the result in matrix form yields

$$
\begin{aligned}
&(\mathbb{G}_{i1},\dots,\mathbb{G}_{iN})\begin{pmatrix}\mathbf{p}_1^{(\mathrm{fl})}\\ \vdots \\ \mathbf{p}_N^{(\mathrm{fl})}\end{pmatrix} = \left(\mathbb{G}_{i1}^{(0)},\dots,\mathbb{G}_{iN}^{(0)}\right)\begin{pmatrix}\mathbf{p}_1^{(\mathrm{fl})}\\ \vdots \\ \mathbf{p}_N^{(\mathrm{fl})}\end{pmatrix} \\
&+\varepsilon_0\mu_0\omega^2\left(\mathbb{G}_{i1}^{(0)},\dots,\mathbb{G}_{iN}^{(0)}\right)\begin{pmatrix}\alpha_1^{(0)} & 0 & 0\\ 0 & \ddots & 0\\ 0 & 0 & \alpha_N^{(0)}\end{pmatrix}\begin{pmatrix}\mathbb{G}_{11} & \cdots & \mathbb{G}_{1N}\\ \vdots & \ddots & \vdots\\ \mathbb{G}_{N1} & \cdots & \mathbb{G}_{NN}\end{pmatrix}\begin{pmatrix}\mathbf{p}_1^{(\mathrm{fl})}\\ \vdots \\ \mathbf{p}_N^{(\mathrm{fl})}\end{pmatrix}
\end{aligned}
\tag{5.35}
$$

Equation (5.35) can be expressed not just from all N particles to i, but rather from all N particles to all N particles. Doing so changes Equation (5.35) to

$$
\begin{aligned}
&\begin{pmatrix}\mathbb{G}_{11} & \cdots & \mathbb{G}_{1N}\\ \vdots & \ddots & \vdots\\ \mathbb{G}_{N1} & \cdots & \mathbb{G}_{NN}\end{pmatrix} = \begin{pmatrix}\mathbb{G}_{11}^{(0)} & \cdots & \mathbb{G}_{1N}^{(0)}\\ \vdots & \ddots & \vdots\\ \mathbb{G}_{N1}^{(0)} & \cdots & \mathbb{G}_{NN}^{(0)}\end{pmatrix} \\
&+\frac{\omega^2}{c^2}\begin{pmatrix}\mathbb{G}_{11}^{(0)} & \cdots & \mathbb{G}_{1N}^{(0)}\\ \vdots & \ddots & \vdots\\ \mathbb{G}_{N1}^{(0)} & \cdots & \mathbb{G}_{NN}^{(0)}\end{pmatrix}\begin{pmatrix}\alpha_1^{(0)} & 0 & 0\\ 0 & \ddots & 0\\ 0 & 0 & \alpha_N^{(0)}\end{pmatrix}\begin{pmatrix}\mathbb{G}_{11} & \cdots & \mathbb{G}_{1N}\\ \vdots & \ddots & \vdots\\ \mathbb{G}_{N1} & \cdots & \mathbb{G}_{NN}\end{pmatrix}
\end{aligned}
\tag{5.36}
$$

Now, combining the terms with matrices of $\mathbb{G}_{ij}$ yields an equation for the system Green's functions in the desired form:

$$
\begin{aligned}
&\left[\begin{pmatrix}\mathbb{I} & 0 & 0\\ 0 & \ddots & 0\\ 0 & 0 & \mathbb{I}\end{pmatrix}-\frac{\omega^2}{c^2}\begin{pmatrix}\mathbb{G}_{11}^{(0)} & \cdots & \mathbb{G}_{1N}^{(0)}\\ \vdots & \ddots & \vdots\\ \mathbb{G}_{N1}^{(0)} & \cdots & \mathbb{G}_{NN}^{(0)}\end{pmatrix}\begin{pmatrix}\alpha_1^{(0)} & 0 & 0\\ 0 & \ddots & 0\\ 0 & 0 & \alpha_N^{(0)}\end{pmatrix}\right] \\
&\cdot\begin{pmatrix}\mathbb{G}_{11} & \cdots & \mathbb{G}_{1N}\\ \vdots & \ddots & \vdots\\ \mathbb{G}_{N1} & \cdots & \mathbb{G}_{NN}\end{pmatrix} = \begin{pmatrix}\mathbb{G}_{11}^{(0)} & \cdots & \mathbb{G}_{1N}^{(0)}\\ \vdots & \ddots & \vdots\\ \mathbb{G}_{N1}^{(0)} & \cdots & \mathbb{G}_{NN}^{(0)}\end{pmatrix}
\end{aligned}
\tag{5.37}
$$

Equation (5.37) can be written in simpler matrix notation as

$$\mathbb{A}\mathbb{G} = \mathbb{G}^{(0)} \tag{5.38}$$

where each term is a $3N\times3N$ matrix consisting of N^2 3×3 submatrices. The submatrices of $\mathbb{G}$ are simply the system Green's functions $\mathbb{G}_{ij}$, and the submatrices of $\mathbb{G}^{(0)}$ are similarly the Green's functions for the background medium $\mathbb{G}_{ij}^{(0)}$. The submatrices of $\mathbb{A}$ are defined as

$$\mathbb{A}_{ij} = \delta_{ij}\mathbb{I} - \frac{\omega^2}{c^2}\mathbb{G}_{ij}^{(0)}\alpha_j^{(0)} \tag{5.39}$$

Equation (5.37) can also be written for just one column of the system Green's functions using the notation above to obtain

$$\mathbb{A}\begin{pmatrix}\mathbb{G}_{1j}\\ \vdots \\ \mathbb{G}_{Nj}\end{pmatrix} = \begin{pmatrix}\mathbb{G}_{1j}^{(0)}\\ \vdots \\ \mathbb{G}_{Nj}^{(0)}\end{pmatrix} \tag{5.40}$$

This represents a final equation for system Green's functions in the form $\mathbb{A}\cdot\mathbf{x} = \mathbf{b}$, which admits iterative numerical solutions. The first matrix ($\mathbb{A}$) is a full, completely defined $3N \times 3N$ interaction matrix. The second matrix ($\mathbb{G}_{ij}$) is an unknown $3N \times 3$ matrix, containing $N \times 1$ unknown system Green's functions from all particles to particle j. The right side is a $3N \times 3$ matrix consisting of known Green's functions for the background medium. By the property $\mathbb{G}_{ij} = \mathbb{G}_{ji}$, the system Green's functions from particle j to all N particles can also be obtained.

This equation is also very similar to that developed by Ben-Abdallah *et al.* in the many-body radiative heat transfer theory [114], except that they use the dressed polarizability instead of the bare polarizability and they set $\mathbb{G}_{ii}^{(0)} = 0$ because they are working in terms of the exciting field instead of the actual field. Their approach is also valid, but the energy transfer equation and the form of the fluctuation dissipation that must then be used are different than what is used here.

5.3.2 Energy Transfer with System Green's Functions

Once the system Green's functions have been determined, they can be used to calculate the NFRHT between particles or subvolumes. The equations to do so are developed here. The net power absorbed by the ith dipole is [53, 115, 116]

$$Q_i(t, T_1, \ldots, T_N) = 2\int_0^\infty \frac{d\omega}{2\pi}\omega \int_0^\infty \frac{d\omega'}{2\pi} \mathrm{Im}\left[\langle \mathbf{p}_i(\omega) \cdot \mathbf{E}_i^*(\omega')\rangle \mathrm{e}^{-i(\omega-\omega')t}\right] \quad (5.41)$$

Using Equations (5.3) and (5.8) to replace the $\mathbf{p}_i(\omega)$ term results in

$$Q_i(t, T_1, \ldots, T_N) = 2\int_0^\infty \frac{d\omega}{2\pi}\omega \int_0^\infty \frac{d\omega'}{2\pi} \mathrm{Im}\left[\left\langle \left(\varepsilon_0 \alpha_i^{(0)} \mathbf{E}_i(\omega) + \mathbf{p}_i^{(\mathrm{fl})}(\omega)\right) \cdot \mathbf{E}_i^*(\omega')\right\rangle \mathrm{e}^{-i(\omega-\omega')t}\right] \quad (5.42)$$

Then, using Equation (5.34) to replace the electric field terms, this becomes

$$Q_i(t, T_1, \ldots, T_N) = 2\int_0^\infty \frac{d\omega}{2\pi}\omega \int_0^\infty \frac{d\omega'}{2\pi} \mathrm{Im}\left[\left\langle\left(\varepsilon_0\mu_0\alpha_i^{(0)}\omega^2 \sum_j \mathbb{G}_{ij}\cdot \mathbf{p}_j^{(\mathrm{fl})} + \mathbf{p}_i^{(\mathrm{fl})}\right)\cdot \mu_0\omega'^2 \sum_k \mathbb{G}_{ik}'^{*}\cdot \mathbf{p}_k^{(\mathrm{fl})'*}\right\rangle \mathrm{e}^{-i(\omega-\omega')t}\right] \tag{5.43}$$

where the primes indicate that the variables are functions of ω'. After some manipulation and changing to cartesian index notation, the following equation is obtained:

$$\begin{aligned} &Q_i(t, T_1, \ldots, T_N) \\ &= 2\int_0^\infty \frac{d\omega}{2\pi}\omega \int_0^\infty \frac{d\omega'}{2\pi} \mathrm{Im}\left[\left(\varepsilon_0\mu_0^2\alpha_i^{(0)}\omega^2\omega'^2 \sum_{jk} G_{ij,\alpha\beta}G_{ik,\alpha\gamma}'^{*}\langle p_{j,\beta}^{(\mathrm{fl})}p_{k,\gamma}^{(\mathrm{fl})'*}\rangle \right.\right. \\ &\left.\left. + \mu_0\omega'^2 \sum_k G_{ik,\alpha\gamma}'^{*}\langle p_{i,\alpha}^{(\mathrm{fl})}p_{k,\gamma}^{(\mathrm{fl})'*}\rangle\right)\mathrm{e}^{-i(\omega-\omega')t}\right] \end{aligned} \tag{5.44}$$

Using the fluctuation-dissipation theorem from Equation (5.20), reverting back to standard notation, and simplifying, the net power absorbed is

$$
\begin{aligned}
&Q_i(t, T_1, \ldots, T_N) \\
&= 2\int_0^\infty \frac{d\omega}{\pi}\hbar\varepsilon_0\mu_0\omega^3\left[\varepsilon_0\mu_0\mathrm{Im}\left(\alpha_i^{(0)}\right)\omega^2\sum_j \mathrm{Tr}\left(\mathbb{G}_{ij}\mathbb{G}_{ij}^\dagger\right)f_j^{(\mathrm{BE})}\mathrm{Im}\left(\alpha_j^{(0)}\right)\right. \\
&\left.+\,\mathrm{Im}(\mathrm{Tr}[\mathbb{G}_{ii}^*])f_i^{(\mathrm{BE})}\mathrm{Im}\left(\alpha_i^{(0)}\right)\right]
\end{aligned}
\tag{5.45}
$$

At thermal equilibrium, the net power absorbed by every particle must be zero. Using this fact, the following condition is obtained [115]:

$$
0 = \varepsilon_0\mu_0\mathrm{Im}\left(\alpha_i^{(0)}\right)\omega^2\sum_j \mathrm{Tr}\left(\mathbb{G}_{ij}\mathbb{G}_{ij}^\dagger\right)\mathrm{Im}\left(\alpha_j^{(0)}\right) + \mathrm{Im}(\mathrm{Tr}[\mathbb{G}_{ii}^*])\mathrm{Im}\left(\alpha_i^{(0)}\right) \tag{5.46}
$$

Inserting Equation (5.46) into Equation (5.45) and recognizing that $\mathrm{Im}\left(\alpha_i^{(0)}\right) = V_i\mathrm{Im}(\varepsilon_i)$ results in the net power absorbed written as a sum of exchanges with other particles:

$$
\begin{aligned}
&Q_i(t, T_1, \ldots, T_N) \\
&= 2\int_0^\infty \frac{d\omega}{\pi}\hbar\varepsilon_0^2\mu_0^2\omega^5 V_i\mathrm{Im}(\varepsilon_i)\sum_{j\neq i}\mathrm{Tr}\left(\mathbb{G}_{ij}\mathbb{G}_{ij}^\dagger\right)f_{ji}^{(\mathrm{BE})}V_j\mathrm{Im}\left(\varepsilon_j\right)
\end{aligned}
\tag{5.47}
$$

Rearranging this into a Landauer-like form provides a final equation for net power absorption by particle i:

$$
Q_i(t, T_1, \ldots, T_N) = \int_0^\infty \frac{d\omega}{2\pi}\sum_{j\neq i}\hbar\omega f_{ji}^{(\mathrm{BE})}\mathcal{T}_{ij}(\omega) \tag{5.48}
$$

where $\mathcal{T}_{ij}(\omega)$ is a transmission coefficient from j to i given by

$$\mathcal{T}_{ij}(\omega) = 4k_0^4 V_i V_j \mathrm{Im}(\varepsilon_i)\mathrm{Im}\left(\varepsilon_j\right)\mathrm{Tr}\left(\mathbb{G}_{ij}\mathbb{G}_{ij}^{\dagger}\right) \tag{5.49}$$

where $k_0^2 = \varepsilon_0\mu_0\omega^2$. These final equations are nearly identical to those presented by Ben-Abdallah *et al.* [114] except that they use the imaginary parts of the particle polarizabilities instead of the $V_i V_j \mathrm{Im}(\varepsilon_i)\mathrm{Im}\left(\varepsilon_j\right)$ factor, and the system Green's functions here are defined to include the self terms. In a T-DDA formalism where a subset of particles constitutes a single body V_A, the net heat transfer to that body is simply the summation of power absorption by all $i \in V_A$. Additionally, Equation (5.48) separates the power absorption by i into contributions from every other particle. Thus, the net heat transfer directly between particle i and another particle j can be written as

$$Q_{j\to i}(t) = \int_0^\infty \frac{d\omega}{2\pi}\, \hbar\omega f_{ji}^{(\mathrm{BE})} \mathcal{T}_{ij}(\omega) \tag{5.50}$$

It follows that the conductance between particles i and j is

$$G_{ij}(t) = \int_0^\infty \frac{d\omega}{2\pi}\, \frac{\partial\Theta(\omega, T_i)}{\partial T} \mathcal{T}_{ij}(\omega) \tag{5.51}$$

5.3.3 Validation of System Green's Function Approach

Implementation of the system Green's function approach to NFRHT between many particles in an efficient, open-source manner (like existing DDA codes [99, 205]) is a research task that will take considerable time. However, as an initial step, the approach is validated against two other codes: a MATLAB implementation of the T-DDA [51] and the many dipole results for nanoparticles presented in Section 5.2.

First, the system Green's function approach is compared to the T-DDA [51] for NFRHT between two cubes of SiO_2 with different numbers of subvolumes. The cubes are 0.5 μm long on a side and are also separated by 0.5 μm. Custom MATLAB scripts are developed for both methods, and the resulting spectral thermal conductance between the cubes is shown in Figure 5.7.

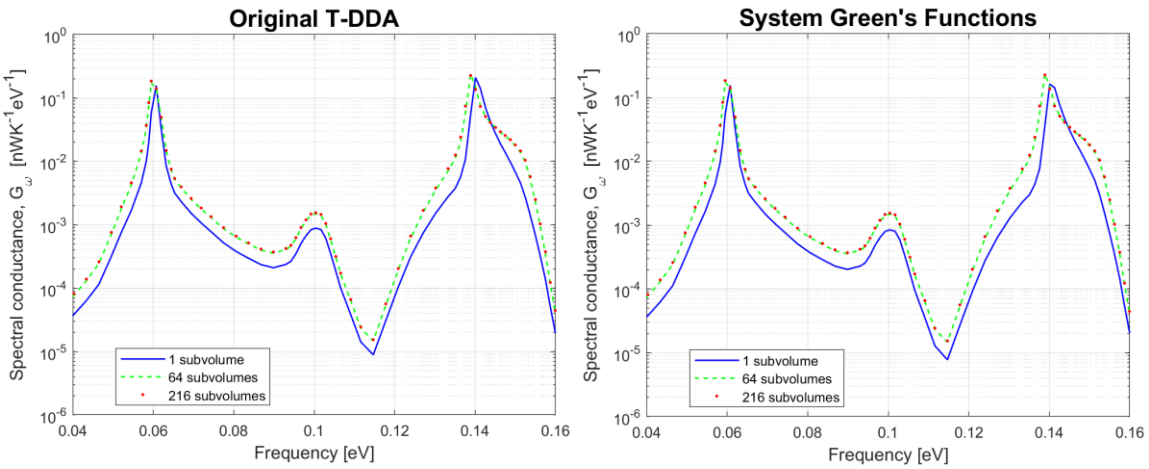

Figure 5.7. Spectral thermal conductance between two SiO_2 cubes calculated via the original T-DDA and the system Green's functions approach.

As shown by the figure, these two calculation methods give identical results, thereby validating the system Green's function formalism. Because the two approaches share common fundamental theory, the fact that they produce identical results is not surprising and gives confidence that the derivations of the system Green's function approach are free of errors.

The system Green's function approach is compared to the results shown in Figure 5.4(b) for the radiative thermal conductivity of ordered arrays of SiC particles. Chains and planes of 50 nm diameter particles with $d = 75$ nm in background $\varepsilon_m = 1$ are analyzed. A

custom MATLAB script was written for the system Green's function approach, and the results are shown in Figure 5.8.

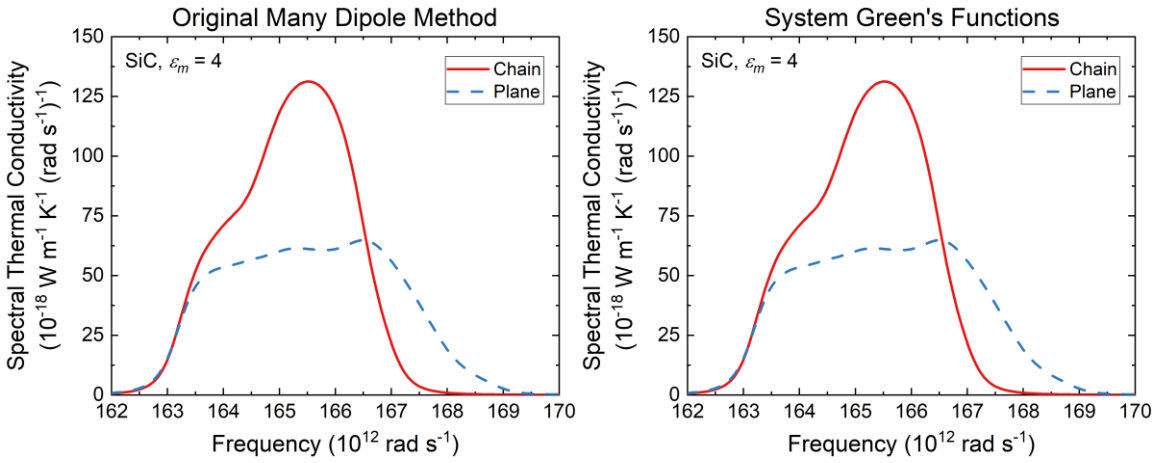

Figure 5.8. Spectral thermal conductivity in ordered SiC arrays calculated via the original many dipole method and the system Green's functions approach.

Once again, the figure shows that the two methods give identical results, even for different geometric arrangements of the nanoparticles. As when comparing the T-DDA results, this is not surprising since the two methods share the same fundamental framework. However, these results do validate the system Green's function approach and allow future research to focus on computational efficiency.

5.4 Conclusions from Fluctuational Electrodynamics Studies

When nanostructures or subvolumes are modeled as point dipoles, two theoretical formalisms (the many-body method and the T-DDA) have emerged that use different forms of the fluctuation-dissipation theorem. This chapter shows that these two formalisms are mathematically equivalent. Furthermore, it demonstrates that a straightforward use of the fluctuation-dissipation theorem is appropriate with the T-DDA approach, and the reduced

absorption factor used with the many-body method is needed due to its definition of the induced and fluctuating dipole moments. These clarifications should assist future researchers in using correct forms of the fluctuation-dissipation theorem.

To compare results from radiation calculations to other forms of heat transfer in large nanoparticle arrays, a method to calculate the effective radiative thermal conductivity from particle-particle thermal conductance is developed. This method is used to analyze ordered chains, planes, and three-dimensional arrays of SiO_2 and SiC nanoparticles. Comparison of the two material systems demonstrates that the radiative transport is strongly influenced by whether the materials support propagating surface polariton modes. Additionally, it is shown that many-body effects may enhance or suppress radiative transport depending on the geometry, spacing, and optical properties of the materials. These results can help in the design of systems that utilize thermal radiation as a significant form of heat transfer. It is also found that ordered nanoparticle chains always exhibit higher radiative thermal conductivities than disordered particle chains due to disruption of propagating modes or increased distance between particles. Additional studies should focus on the impact of multipolar effects at small spacing and in disordered arrays, the effects of nonuniform size distribution in particle arrays [206], and methods to enhance thermal radiation in nanostructure arrays such as the use of nonhomogeneous environments [113].

These existing methods have significant computational limitations for large numbers of particles or subvolumes due to the need to store and invert a large interaction matrix. Inspired by DDA codes which use iterative numerical methods to avoid this requirement, a system Green's function formalism for NFRHT is developed that should enable similar improvements in computational efficiency. The system Green's functions are derived in

the form $\mathbb{AG} = \mathbb{B}$, which admits iterative numerical solutions for $\mathbb{G}$. Relations for energy exchange using these system Green's functions are also derived, and the methodology is validated against the T-DDA and the formalism for thermal radiation between many dipoles. This approach should enable the development of fast, efficient, open-source programs for NFRHT between many nanostructures or arbitrary bodies to aid researchers in a variety of applications.

CHAPTER 6. CORRESPONDANCE OF KINETIC AND FLUCTUATIONAL APPROACHES

KT approaches to NFRHT were used in Chapters 3 and 4, and FE approaches were used in Chapters 3 and 5. Both methods provide their own advantages and disadvantages. For example, KT provides insight into collective behavior and is very similar to common descriptions of phonon and electron transport, but it only describes delocalized SPs that propagate through a nanostructure array, and it neglects other radiative transport. FE, on the other hand, is an exact method (as long as the dipole assumption holds) that describes all electromagnetic interactions, but it can be computationally intensive for large numbers of particles.

Even in some situations that may favor the use of KT, its validity is questionable when propagation lengths are very short. This has led to broader questions about the overall applicability of KT. In particular, Kathmann *et al.* [124] examined chains of hBN and Au nanoparticles via KT and FE, and they found significant disagreement between the two methods. The majority of the cases they examined, however, had propagation lengths shorter than the particle center-to-center spacing. Because KT can be a useful tool to analyze NFRHT (as shown by its use throughout this dissertation), it is important to understand its validity and any applicable regimes of validity for future use.

In this chapter (also presented in references [202] and [207]), the correspondence of KT and FE is examined in two ways. First, the spectral thermal emission from ordered particle arrays is calculated by FE and compared to the density of states predicted by the

dispersion relation (KT). Agreement between these two quantities demonstrates that collective effects dictated by the dispersion govern NFRHT, which is shown to be the case when propagation lengths exceed the particle spacing. Second, the radiative thermal conductivity predicted by both KT and FE is compared. KT also provides a choice between the use of a complex frequency or a complex wavevector, as discussed in Section 2.2.1, and both of these options are examined. It is shown that for the choice of a complex frequency when the propagation lengths exceed the particle spacing, there is excellent agreement between KT and FE.

6.1 Thermal Emission from Ordered Particle Arrays

KT models exist not only for nanostructure arrays, but also for SPs propagating along a planar interface. In 2000 Shchegrov *et al.* [208] demonstrated that these propagating SPs determine the spectrum of near-field thermal emission calculated by FE. No such studies, however, have been performed for nanoparticle systems, and it remains unclear how collective effects may influence near-field emission from collections of nanoparticles. To better understand the interaction between propagating SPs and NFRHT, the spectrum of near-field thermal emission from ordered arrays of polaritonic nanoparticles is calculated and compared to the density of states found from dispersion relations. Contrary to planar materials, it is shown that propagating modes lower and broaden the resonant peak in thermal emission and the emission characteristics are very different when propagating modes are present (in SiC systems) or absent (in SiO_2 systems).

6.1.1 Calculation Methods

Consider N nonmagnetic spherical nanoparticles of radius a much smaller than the characteristic thermal wavelength and center-to-center spacing $d \geq 3a$, such that they may be modeled as electric dipoles [31, 78, 83, 92]. The nanoparticles are immersed in a transparent medium with relative permittivity ε_m. Using the framework of the many-body theory developed by Messina *et al.* [115], the induced part of the dipole moment can be written as

$$\mathbf{p}_j^{(\mathrm{ind})} = \varepsilon_0 \alpha_j^{(\mathrm{d})} \mu_0 \omega^2 \sum_{k \neq j} \mathbb{G}_{jk}^{(0)} \mathbf{p}_k \tag{6.1}$$

By combining this with Equation (5.3) and rewriting in matrix form, the total dipole moments of all particles can be expressed as

$$\begin{pmatrix} \mathbf{p}_1 \\ \vdots \\ \mathbf{p}_N \end{pmatrix} = \mathbb{A}^{-1} \begin{pmatrix} \mathbf{p}_1^{(\mathrm{fl})} \\ \vdots \\ \mathbf{p}_N^{(\mathrm{fl})} \end{pmatrix} \tag{6.2}$$

The $3N \times 3N$ matrix $\mathbb{A}$ has $N \times N$ elements $\mathbb{A}_{jk}$ with $j, k = 1, \ldots, N$ and each $\mathbb{A}_{jk}$ consisting of a 3×3 tensor defined by

$$\mathbb{A}_{jk} = \delta_{jk} \mathbb{1} - \left(1 - \delta_{jk}\right) \frac{\omega^2}{c^2} \alpha_j^{(\mathrm{d})} \mathbb{G}_{jk}^{(0)} \tag{6.3}$$

Inserting Equation (6.2) into Equation (5.1) yields the electric field produced by a collection of nanoparticles in terms of the fluctuating part of their dipole moments

$$\mathbf{E}_{\mathbf{r}} = \sum_{j} \mathbb{B}_{\mathbf{r}j} \mathbf{p}_{j}^{(\mathrm{fl})} \tag{6.4}$$

where

$$\left(\mathbb{B}_{\mathbf{r}\,1} \quad \ldots \quad \mathbb{B}_{\mathbf{r}\,N}\right) = \mu_0 \omega^2 \left(\mathbb{G}_{\mathbf{r}\,1}^{(0)} \quad \ldots \quad \mathbb{G}_{\mathbf{r}\,N}^{(0)}\right) \mathbb{A}^{-1} \tag{6.5}$$

The quantity of interest, the spectral density of emitted energy by the collection of nanoparticles, can now be written as

$$u = \frac{\varepsilon_m \varepsilon_0}{2} \langle \mathbf{E}_{\mathbf{r}} \cdot \mathbf{E}_{\mathbf{r}}^{\star} \rangle = \frac{\varepsilon_m \varepsilon_0}{2} \sum_{jk} \sum_{\beta\gamma} \mathbb{B}_{\mathbf{r}j,\alpha\beta} \, \mathbb{B}_{\mathbf{r}k,\alpha\gamma}^{\star} \, \langle p_{j,\beta}^{(\mathrm{fl})} p_{k,\gamma}^{(\mathrm{fl})\star} \rangle \tag{6.6}$$

Here the Greek letters are indices 1, 2, 3 and represent the Cartesian components of the vector quantities. A simplified form of the fluctuation-dissipation theorem gives the relation between the fluctuating dipole moments [114]

$$\langle p_{j,\beta}^{(\mathrm{fl})} p_{k,\gamma}^{(\mathrm{fl})\star} \rangle = 2 \frac{\varepsilon_0}{\omega} \mathrm{Im}\left(\alpha_j^{(\mathrm{d})}\right) \Theta(\omega, T_j) \delta_{jk} \delta_{\beta\gamma} \tag{6.7}$$

The fluctuation-dissipation theorem is used to obtain a final expression for the spectral density of emitted energy

$$u(\mathbf{r}, \omega) = \frac{\varepsilon_m \varepsilon_0^2}{\omega} \sum_{j} \left[\mathrm{Tr}\left(\mathbb{B}_{\mathbf{r}j} \mathbb{B}_{\mathbf{r}j}^{\dagger}\right) \mathrm{Im}\left(\alpha_j^{(\mathrm{d})}\right) \Theta(\omega, T_j) \right] \tag{6.8}$$

This equation provides an explicit analytical method of calculating the fields at any location produced by arbitrarily arranged groups of nanoparticles knowing only their dielectric

functions (expressed through the polarizability), temperatures, and the permittivity of the medium.

6.1.2 Materials and Geometry

Nanoparticle arrays of SiO_2 and SiC in four different arrangements, as shown in Figure 6.1, are analyzed. Single particles, chains, planes, and simple cubic three-dimensional systems are considered. The radius and spacing of all nanoparticles are $a =$ 25 nm and $d = 75$ nm, and all particles are at a constant temperature of 500 K. The location for the calculated local energy density is one diameter above the middle of the center-top nanoparticle as indicated by the stars in Figure 6.1.

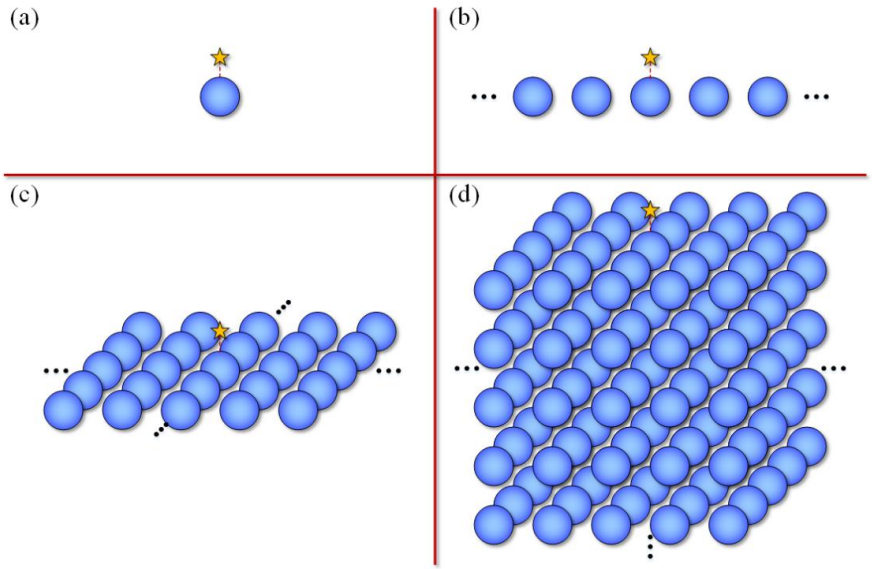

Figure 6.1. Nanoparticle arrangements used for calculating near-field thermal emission including (a) single particles, (b) chains, (c) planes, and (d) 3D arrays.

To select the number of particles used for each material and geometry, particles are repeatedly added to the system until the resulting spectra change by less than 1% for every frequency. Both SiO_2 and SiC support SPhPs with resonances in the Reststrahlen band

between the transverse and longitudinal optical phonon frequencies. For amorphous SiO_2 there are two Reststrahlen bands, and the dielectric function is modeled using data from Palik [144] with $\omega_{TO,1} = 87$ Trad/s, $\omega_{LO,1} = 95$ Trad/s, $\omega_{TO,2} = 202$ Trad/s, and $\omega_{LO,2} = 234$ Trad/s. For SiC, the dielectric function is well-described by the Lorentz model

$$\varepsilon(\omega) = \varepsilon_\infty \left(1 + \frac{\omega_{LO}^2 - \omega_{TO}^2}{\omega_{TO}^2 - \omega^2 - i\omega\Gamma}\right) \tag{6.9}$$

with $\varepsilon_\infty = 6.7$, $\omega_{TO} = 149$ Trad/s, $\omega_{LO} = 182$ Trad/s, and $\Gamma = 0.892$ Trad/s [144]. With the dielectric function and the permittivity of the surrounding medium, each nanoparticle's polarizability can be expressed with the dressed polarizability in Equation (5.5). The quadrupole contributions to polarizability [209] have also been checked and found to be negligible for all systems considered here.

6.1.3 Comparison of Thermal Emission and Propagating Density of States

With these geometries and dielectric functions in hand, the spectral energy density of emitted near-field thermal radiation is calculated with Equation (6.8) and shown in Figure 6.2 for particles in a medium with $\varepsilon_m = 4$, which is selected by maximizing the emission in the SiC case. For SiO_2 nanoparticles, resonances are seen in the two Reststrahlen bands, and the peaks rise as dimensions are added to the nanoparticle arrays. The increase and broadening of the peaks suggest additive effects and the absence of long-range coupling as more particles are added around the central location, which is further supported by low convergence requirements: the spectra converged for a 5-particle chain, 7 × 7-particle plane, and a 7 × 7 × 4-particle 3D array. In contrast, the thermal emission from SiC nanoparticles changes significantly as the system is changed from a single

particle to a chain, plane, or 3D array of particles. The peak height reduces by about 1/2 of its single-particle value and splits to form multiple peaks covering a broader spectral region. Additionally, SiC has much higher convergence requirements: 15 particles in a chain, 17 × 17 particles in a plane, and 17 × 17 × 9 particles in a 3D array. This indicates long-range coupling and dispersive type behavior that is absent in the SiO_2 nanoparticle systems.

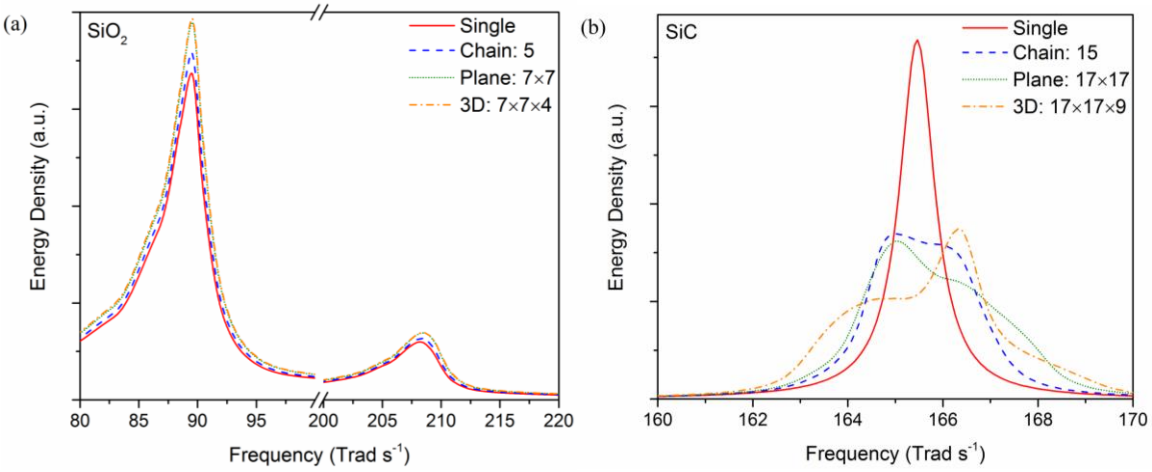

Figure 6.2. Spectral thermal emission from (a) SiO_2 nanoparticle arrays and (b) SiC nanoparticle arrays.

To better understand the differences between these materials and confirm that the emission characteristics of many-particle SiC systems are due to dispersive effects, these spectra are compared to the SPhP dispersion relations for nanoparticle chains given by Equations (2.10) and (2.11). The wavevector is taken as complex, so the imaginary part yields the propagation length (1/e length) $\Lambda = [2\Im(\tilde{k})]^{-1}$ of the SPhP waves traveling along the chain. The dispersion relations are solved numerically with a custom script in MATLAB, and the resulting dispersions and propagation lengths for chains of 50 nm diameter SiO_2 and SiC with $d = 75$ nm in $\varepsilon_m = 4$ are plotted in Figure 6.3.

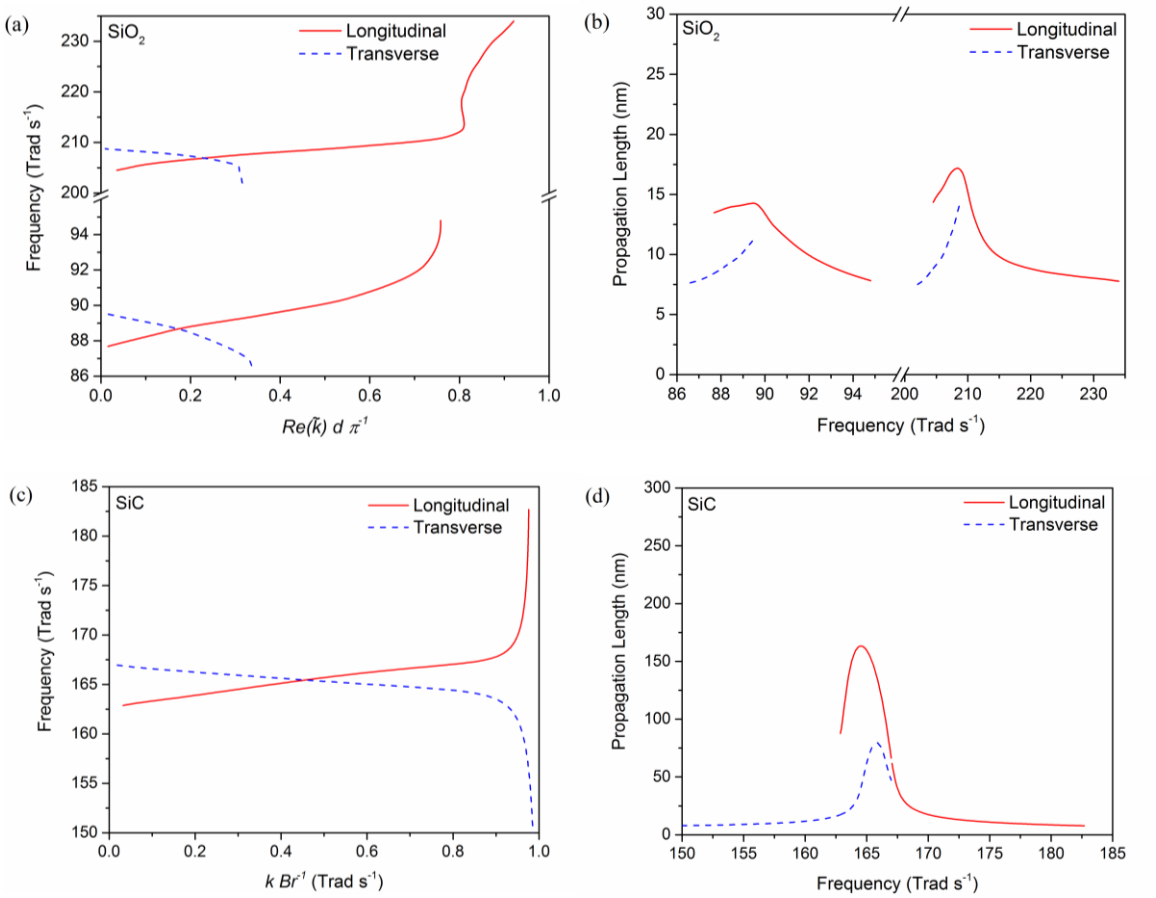

Figure 6.3. (a, c) Dispersion relations and (b, d) propagation lengths for (a, b) SiO_2 and (c, d) SiC nanoparticle chains.

The dispersions for SiO_2 in Figure 6.3(a) and SiC in Figure 6.3(c) do not immediately indicate a strong difference between these materials, but their propagation lengths differ significantly. For SiO_2 as shown in Figure 6.3(b), propagation lengths are shorter than the center-to-center particle spacing, demonstrating that these modes cannot exist because they do not propagate along the chain. For SiC as shown in Figure 6.3(d), however, the longest propagation lengths span multiple particles. The difference in propagation lengths is due to the higher damping (shorter lifetime) of SiO_2 compared to SiC [144, 210]. This confirms that chains of SiC particles do indeed display dispersive SPhP behavior as indicated by the calculations of near-field thermal emission.

To further investigate the relation between the spectral energy density of thermal emission and propagating SPhPs in SiC particle systems, the density of states (DOS) calculated from the dispersion relation, which represents only the propagating SPhP modes, is compared to the thermal emission spectrum, which represents the propagating SPhP modes and all other modes present. Because the DOS describes the number of modes supported at a certain frequency, one would expect a high DOS where there is a peak in thermal emission if propagating SPhPs drive the emission characteristics. The one-dimensional DOS is calculated directly from the dispersion relation as $D_{1D} = [\pi\, \partial\omega/\partial Re(\tilde{k})]^{-1}$. There are two degenerate transverse modes and one longitudinal mode, so $D_{1D} = 2\left(D_{1D,trans}\right) + D_{1D,long}$ is used. This and the spectral energy density of thermal emission from Equation (6.8) are plotted in Figure 6.4 for SiC particle chains. Three different medium permittivities are compared to see if the thermal emission tracks changes in the DOS. Excellent agreement is seen in both the peak shapes and locations, which strongly supports that the emission from SiC particle arrays is dominated by propagating SPhP modes.

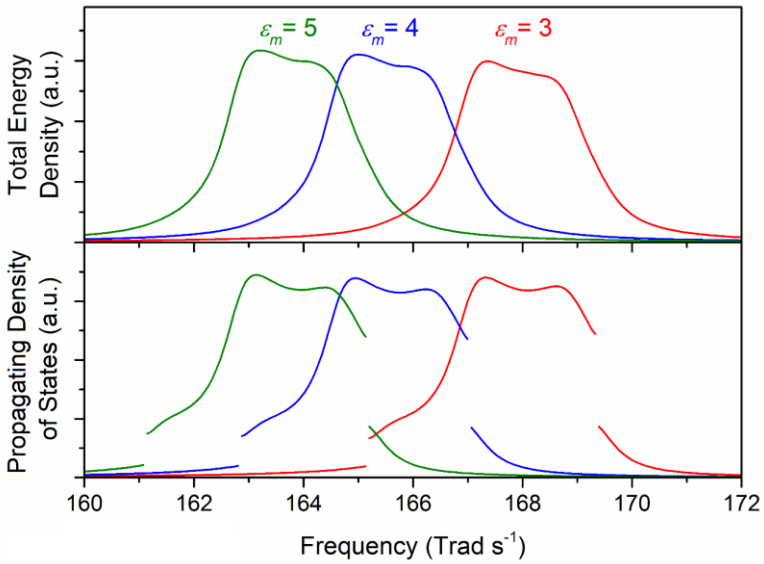

Figure 6.4. (top) Emitted spectral energy density compared to (bottom) the density of states of propagating SPhP modes for SiC nanoparticle chains.

It is not surprising that the characteristics of near-field collective thermal emission from nanoparticle arrays is largely driven by propagating SPhP modes when they are present; the same is true for emission in the near-field from flat surfaces [208]. However, propagating SPhPs on flat surfaces result in a single, sharp peak in thermal emission due to the very high DOS at almost a single frequency. For ordered nanoparticle arrays on the other hand, propagating modes lead to splitting and a decrease in intensity of the resonance peak in thermal emission compared to single nanoparticles. These spectral characteristics are due to interference and phase effects between neighboring particles governed by the dispersion of propagating SPhP waves. When propagating modes are absent, as in SiO_2 nanoparticle arrays, collective effects are additive around the resonance frequency of a single particle. Interference effects no longer cause a splitting of the resonance peaks, because long-range modes are not supported and the emission from neighboring particles

do not strongly influence each other. This leads to an increase in energy density at that frequency and an effective increase in the DOS of the system.

6.2 Radiative Thermal Conductivity of Particle Chains

In the previous section, very good agreement was found between KT and FE in predicting spectral thermal emission peak shapes and locations. On the other hand, a recent study by Kathmann *et al.* found that KT significantly overpredicts the radiative heat transfer near the resonance frequency and has additional limitations for metal nanoparticles supporting SPPs [124]. In this section, these differences are reconciled by calculating the radiative thermal conductivity with both methods for different materials and particle spacings.

6.2.1 Calculation Methods

Consider a chain of isotropic, nonmagnetic nanoparticles of relative permittivity $\varepsilon(\omega)$ immersed in a non-absorbing medium of relative permittivity ε_m, as shown in Figure 6.5. The chain length is much greater than the propagation length of the SPs, such that the heat transfer is diffusive. All particles are at temperature T or $T + \Delta T$ with ΔT approaching zero as required to evaluate thermal conductance in the FE formalism.

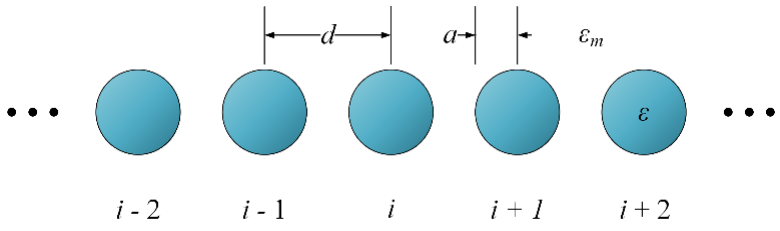

Figure 6.5. Schematic of nanoparticle chain under consideration.

The particles are spherical with radius $a = 25$ nm and are modeled as point dipoles, which is valid when the center-to-center spacing $d \gtrsim 3a$ [31, 78, 83]. The temperature is $T = 500$ K. The material is either hBN in $\varepsilon_m = 1$ as examined by Kathmann *et al.* [124] or SiC in $\varepsilon_m = 4$, because this permittivity maximizes interparticle coupling and corresponds with the previous section. The optical properties of both materials are described by a Lorentz model

$$\varepsilon = \varepsilon_\infty \left(1 + \frac{\omega_{LO}^2 - \omega_{TO}^2}{\omega_{TO}^2 - \omega^2 - i\omega\Gamma}\right) \tag{6.10}$$

where $\varepsilon_\infty = 4.88$ (6.7), $\omega_{LO} = 3.032\times10^{14}$ (1.82×10^{14}) rad s^{-1}, $\omega_{TO} = 2.575\times10^{14}$ (1.49×10^{14}) rad s^{-1}, and $\Gamma = 1.001\times10^{12}$ (8.92×10^{11}) rad s^{-1} for hBN [124, 211] (SiC [144]). The dielectric functions are assumed to be independent of temperature. It is important to note that although hBN is optically anisotropic, isotropic optical properties based on the ordinary component of the dielectric function tensor are used to match the analysis by Kathmann *et al.*

For the FE formalism, the many-body method is used to describe the power absorbed by the *i*th particle in a system as [115]

$$P_i = \int_0^\infty \frac{\hbar\omega}{2\pi} \sum_{j\neq i} \frac{4\chi_i\chi_j}{\left|\alpha_i^{(\mathrm{d})}\right|^2} f_{ji}^{(\mathrm{BE})} \mathrm{Tr}\left(\mathbb{T}_{ij}^{-1}\mathbb{T}_{ij}^{-1\dagger}\right) d\omega \tag{6.11}$$

where $\chi_i = \mathrm{Im}\left(\alpha_i^{(\mathrm{d})}\right) - \left|\alpha_i^{(\mathrm{d})}\right|^2 k^3 (6\pi\varepsilon_m)^{-1}$ and $\mathbb{T}_{ij}^{-1}$ is a subset of the inverted interaction matrix accounting for influences between all particles [115]. By noting that each term in

the summation accounts for the heat transfer from particle j to i, the thermal conductance between two particles can be written as

$$G_{ij} = \frac{\partial P_{ij}(T)}{\partial T} = \int_0^\infty \frac{\hbar\omega}{2\pi} \frac{4\chi_i\chi_j}{|\alpha_i|^2} \frac{\partial f_{BE}}{\partial T_i} \mathrm{Tr}\left(\mathbb{T}_{ij}^{-1}\mathbb{T}_{ij}^{-1\dagger}\right) d\omega \tag{6.12}$$

To evaluate the diffusive thermal conductivity κ, the conductance between every particle in the chain is transformed into a thermal conductivity by following the procedure of Section 5.2.1. For a linear chain, the final thermal conductivity Equation (5.30) can be simplified by recognizing repeated terms and written as

$$\kappa = \frac{1}{A_c} \sum_{j=1}^{N} j G_{ij} L_{ij} \tag{6.13}$$

where $A_c = \pi a^2$ is the cross-sectional area of the chain, there are N particles on each side of the center particle i, j runs from the nearest to the farthest particle on one side of i, and L_{ij} is the center-to-center distance between particles i and j. N is increased until κ converges. $N = 70$ is used for all calculations, and this has been checked to be sufficient in all cases via a maximum convergence criterion of 1% for consecutive iterations.

For the KT formalism, the complex dispersion for the propagating modes must first be obtained [84]. There are two degenerate transverse ($\perp$) modes and one longitudinal ($\parallel$) mode, and their dispersion relations are given by Equations (2.10) and (2.11), respectively. Either ω or k is taken as complex, and the dispersion is solved by varying real k over the first Brillouin zone π/d and solving for complex frequency $\tilde{\omega}$ or by varying real ω and solving for complex wavevector $\tilde{k}$. Once the dispersion is determined, the group velocity

$v_g = \partial\omega/\partial Re(\tilde{k})$ ($v_g = \partial Re(\tilde{\omega})/\partial k$) and propagation length $\Lambda = [2\mathrm{Im}(\tilde{k})]^{-1}$ ($\Lambda = |v_g|[-2\mathrm{Im}(\tilde{\omega})]^{-1}$) are found for the choice of $\tilde{k}$ ($\tilde{\omega}$). For $\tilde{\omega}$, the imaginary part will have negative solutions [84, 85]. This is because the dispersion relations assume a frequency dependence of $e^{-i\omega t}$, requiring $\mathrm{Im}(\tilde{\omega}) < 0$ for oscillations to decay as $t \to \infty$. The typical dispersion relations consequently contain diverging sums [84], which motivates the use of polylogarithms [86] to solve the dispersion relations. Once the dispersions are solved, the diffusive thermal conductivity is calculated with Equation (2.16).

6.2.2 Radiative Thermal Conductivity Results

First, representative dispersion relations and propagation lengths for both SiC and hBN nanoparticle chains are examined to understand their characteristics and collective behavior. Dispersion relations for SiC at $d = 3a$ and hBN at $d = 4a$ are shown in Figure 6.6(a) and (b), and the corresponding propagation lengths are shown in Figure 6.6(c) and (d). The calculations are performed for both $\tilde{\omega}$ (solid lines) and $\tilde{k}$ (dashed lines). The particle spacing is also shown in Figure 6.6(c) and (d), which will become important when considering the validity of KT.

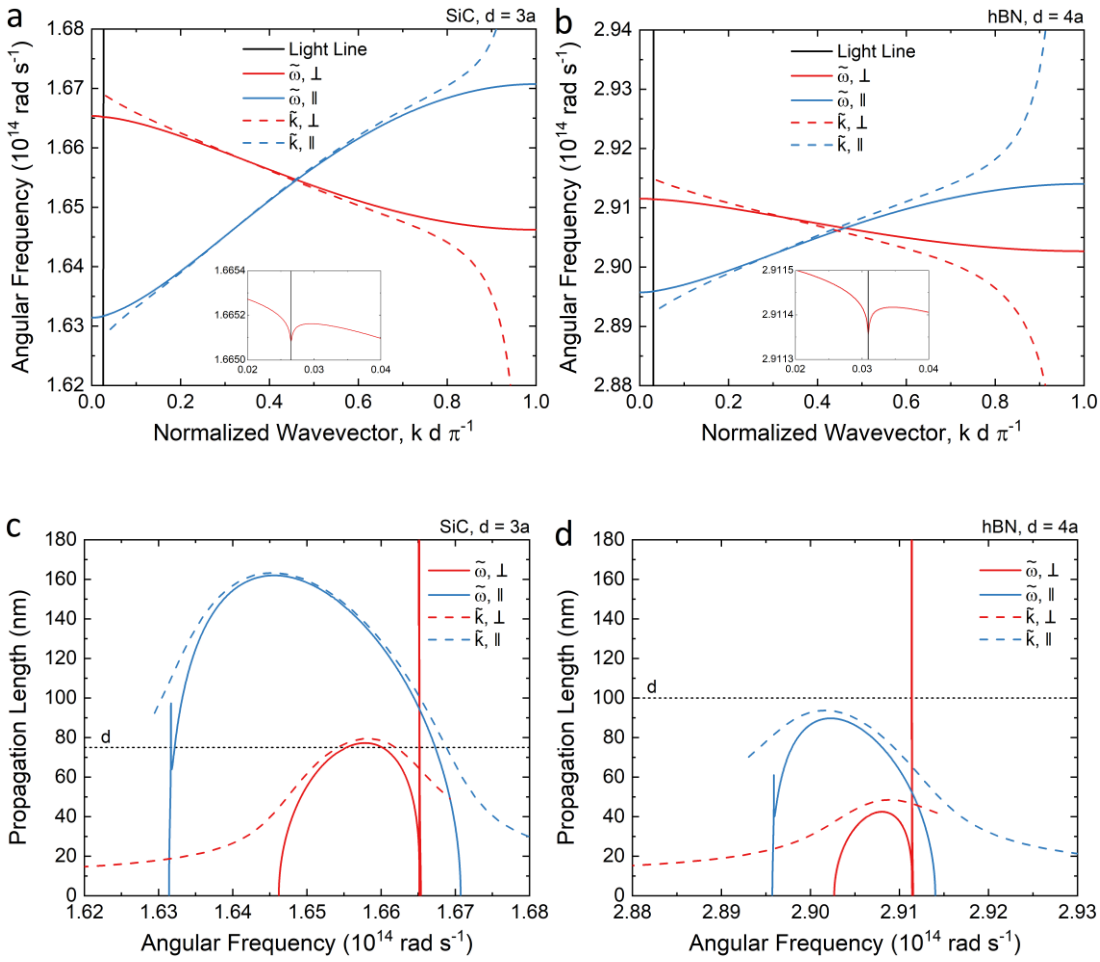

Figure 6.6. (a,b) Dispersion relations and (c,d) propagation lengths for (a,c) SiC and (b,d) hBN nanoparticle chains calculated with both complex ω and complex k.

Both dispersions exhibit the expected behavior and agree with previous calculations for SiC [202] and hBN [124]. For the choice of $\tilde{\omega}$, there is strong coupling with radiative modes at the light line, especially for the transverse modes [84, 85] as illustrated by the insets. This leads to long propagation lengths near that frequency, which will have negligible impact on the radiative thermal conductivity due to the very small bandwidth. The dispersion and propagation lengths for $\tilde{k}$ agree fairly well with those for $\tilde{\omega}$ in the regions of high group velocity, but at the edges of the dispersion there is substantial disagreement. In particular, the dispersion for $\tilde{k}$ diverges at large wavevectors and predicts

low, consistent propagation lengths away from the resonance. The dispersion for $\tilde{\omega}$ does not predict any modes in these regions. For the hBN chain, none of the propagation lengths reach the interparticle spacing, while for the SiC chain most of the longitudinal modes and the center of the transverse modes do. For hBN, this discrepancy calls into question the use of KT, because propagating modes cannot exist if they do not travel between adjacent particles [202, 203].

The spectral radiative thermal conductivity calculated via FE and KT is plotted for SiC at $d = 3a$ and hBN at $d = 4a$ in Figure 6.7(a) and (b).

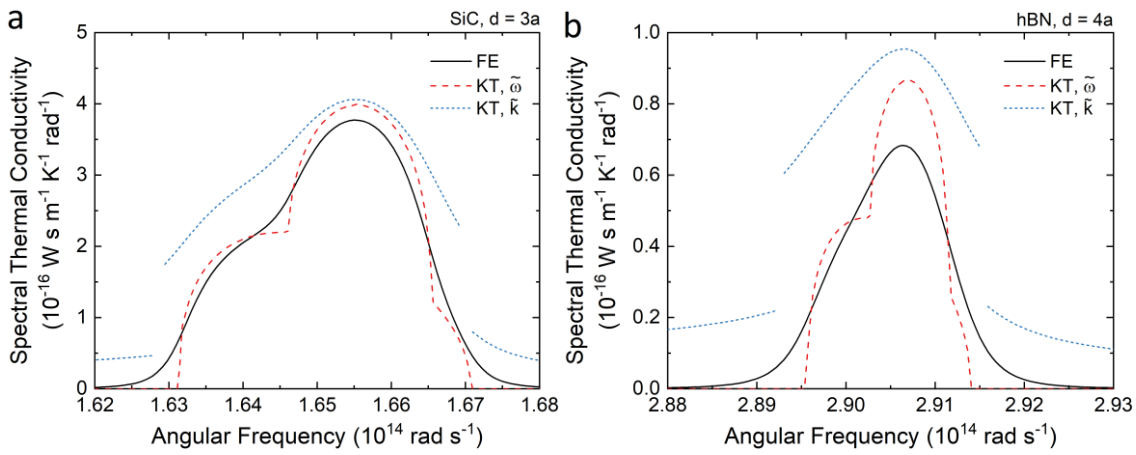

Figure 6.7. Spectral radiative thermal conductivity calculated with FE and KT approaches for (a) SiC and (b) hBN nanoparticle chains.

The results in Figure 6.7(b) match those of Kathmann *et al.* [124] for FE and for KT with $\tilde{\omega}$ when their results are appropriately scaled by $\partial f^{(\mathrm{BE})}/\partial T$. For the SiC case, there is generally good agreement between KT with $\tilde{\omega}$ and FE, with an average absolute error of 10.5% for KT where it is nonzero. The error for total thermal conductivity using KT with $\tilde{\omega}$ after integration is only -3.4% in comparison to the result from FE ($\kappa = 9.99\times10^{-4}$ W m^{-1} K^{-1}). For hBN, on the other hand, KT with $\tilde{\omega}$ substantially overpredicts FE for the

transverse (right peak) modes and has translational error for both the transverse and longitudinal modes. This agrees with the findings of Kathmann *et al.* When KT is used with $\tilde{k}$, the calculations overpredict FE for both materials over the whole spectrum, although the error is more pronounced for hBN.

To understand why KT performs better for SiC at $d = 3a$ than for hBN at $d = 4a$, Figure 6.8 shows the spectral thermal conductivity calculated with all methods for both materials at spacings of $d = 2a$ and $d = 5a$. The spacing of $2a$ violates the assumptions for the dipole approximation, so additional multipolar effects will cause the actual radiative thermal conductivity to differ from that shown here. However, the dipolar contributions to the radiative thermal conductivity predicted by the FE and KT approaches may be safely compared to each other, as they use the same assumptions.

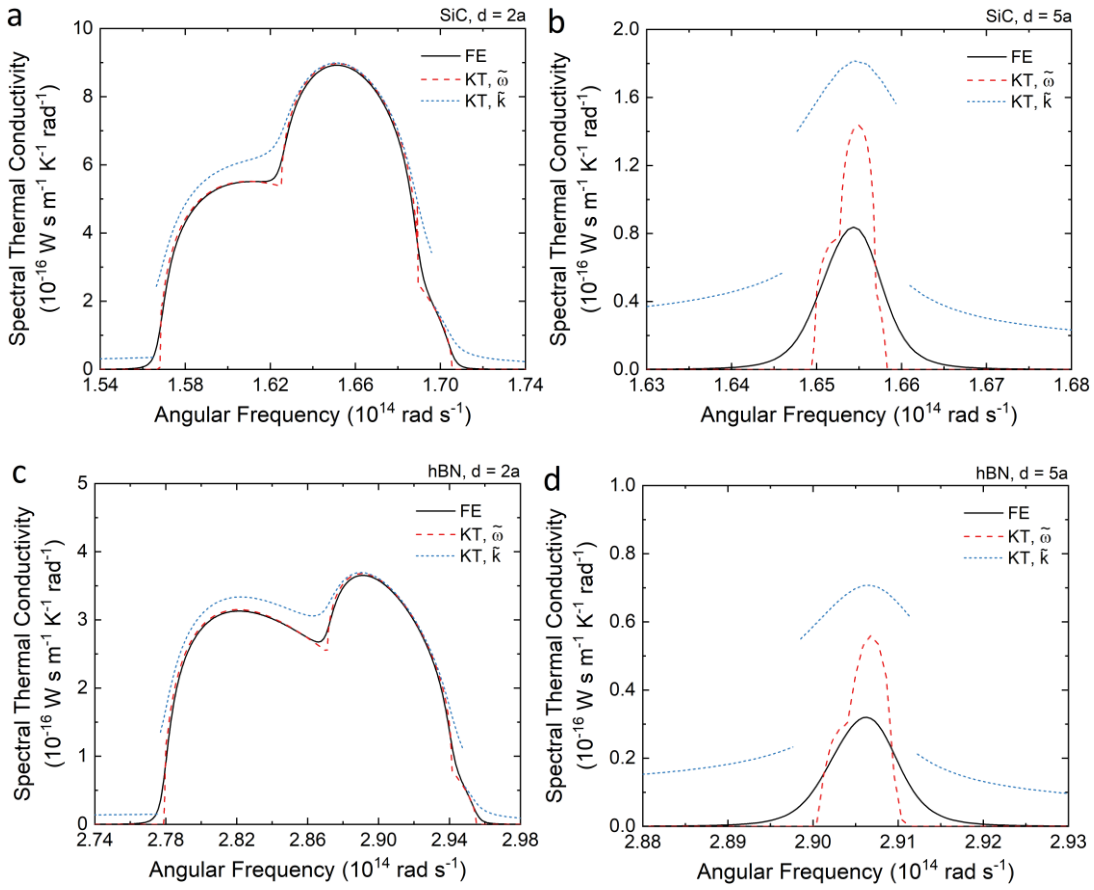

Figure 6.8. Spectral radiative thermal conductivity for (a,b) SiC and (c,d) hBN nanoparticle chains with separation distances of (a,c) $d = 2a$ and (b,d) $d = 5a$.

For the spacing of $d = 2a$ in Figure 6.8(a) and (c), remarkable agreement is observed between KT with $\tilde{\omega}$ and FE for both SiC and hBN. The average absolute error between the two curves is 3.3% (2.7%) for SiC (hBN) where the KT curve is nonzero. The error in total thermal conductivity is -2.5% (0%) for SiC (hBN) compared to $\kappa = 0.0081$ W m^{-1} K^{-1} (0.0048 W m^{-1} K^{-1}) from FE. KT with $\tilde{k}$ still overpredicts the spectral thermal conductivity for both materials at $d = 2a$, but the error is much less than the previous cases. On the other hand, at $d = 5a$ in Figure 6.8(b) and (d) KT clearly fails to predict both the shape and magnitude of the spectral thermal conductivity for both $\tilde{\omega}$ and $\tilde{k}$. The reason for

this difference, as described earlier, is how the propagation lengths compare to d. Plotted in Figure 6.9 are the propagation lengths for SiC at both spacings to illustrate this effect.

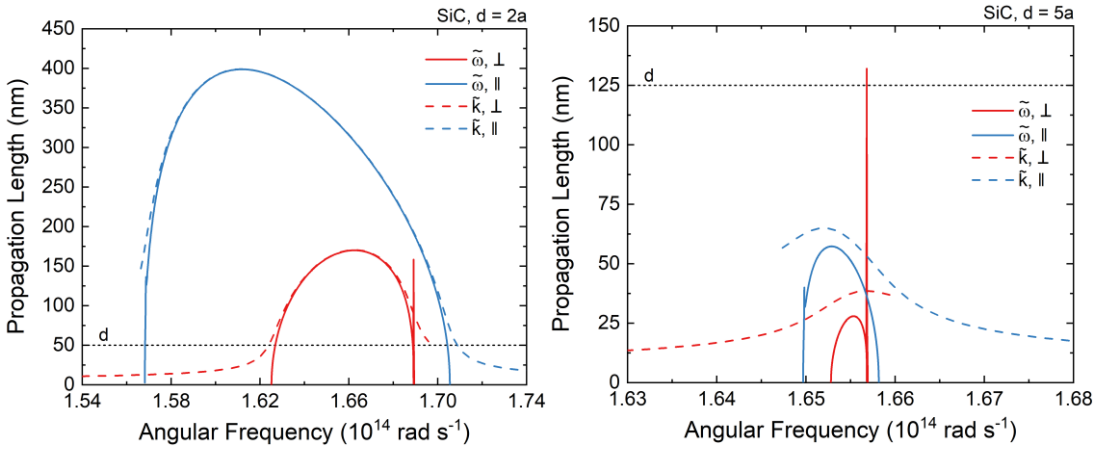

Figure 6.9. Propagation lengths for SiC chains at (a) d = 2a and (b) d = 5a.

As expected, at closer spacing the stronger coupling leads to much longer propagation lengths. In the case shown in Figure 6.9(a), nearly all the modes predicted by KT with $\tilde{\omega}$ exceed d, and the maximum propagation lengths are about $8d$ for the longitudinal and about $3.4d$ for the transverse modes. It is also interesting to note that $\tilde{k}$ has much better agreement with $\tilde{\omega}$ at small spacing, which suggests it may be appropriate to use $\tilde{k}$ in these cases as long as the modes with $\Lambda < d$ are discounted. At farther spacing as shown in Figure 6.9(b), neither the transverse nor the longitudinal modes come close to d. Since the modes cannot span adjacent particles, it is not surprising that KT is an inappropriate formalism for these cases and gives inaccurate results as shown in Figure 6.8(b) and (d).

To further illustrate that KT corresponds with FE when the propagation lengths span adjacent particles, calculations are performed for the same system of hBN particles at

$d = 4a$ as shown in Figure 6.7(b), but the damping coefficient is reduced from $\Gamma = 1.001\times10^{12}$ rad s^{-1} to $\Gamma = 1\times10^{11}$ rad s^{-1}. This fictional material has much lower loss, so the transverse modes now propagate up to about $4d$ and the longitudinal modes up to about $9d$ as shown in Figure 6.10(b). Just as with the closely spaced SiC and hBN particle chains, the FE and KT approaches agree very well as shown in Figure 6.10(a), especially when $\tilde{\omega}$ is used with KT.

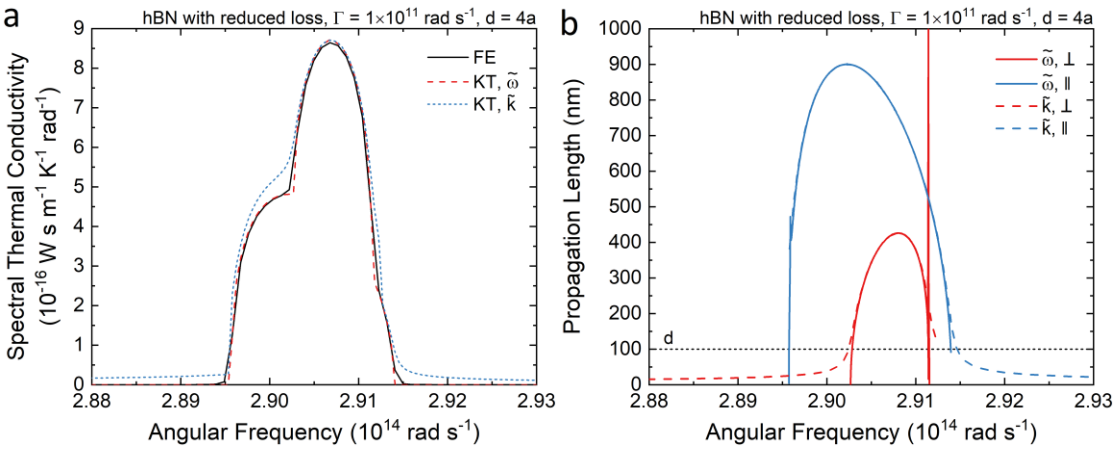

Figure 6.10. (a) Spectral radiative thermal conductivity and (b) propagation lengths for hBN at $d = 4a$ with a reduced damping coefficient $\Gamma = 1\times10^{11}$ rad s^{-1}.

6.3 Conclusions from Comparison of Methods

The comparison of spectral near-field thermal emission from ordered nanoparticle arrays to the density of states from the dispersion relation demonstrates that propagating SPs dictate the thermal electromagnetic interactions when these modes are present. Contrary to planar surfaces, propagating modes decrease and broaden the peak of thermal emission from nanoparticle arrays, and the absence of propagating modes causes an increase in the peak of thermal emission. The comparison of the spectral thermal conductivity calculated by KT and FE also shows that propagating SPs dominate radiative

transport when these modes are present. In particular, the success of KT with $\widetilde{\omega}$ in regimes of strong coupling where $\Lambda > d$ demonstrates conclusively that KT can be a valid method to predict heat transfer by propagating SPs in linear chains of nanostructures. This contradicts the conclusions of Kathmann *et al.* [124] because they only examined chains where the majority of the modes had $\Lambda < d$, and this illustrates that care must be taken to use KT only in its regime of validity. KT with $\tilde{k}$ tends to overpredict KT with $\widetilde{\omega}$, especially at high and low frequencies where $\Lambda < d$. The overprediction decreases when the coupling strength and Λ increase, however, showing that KT with $\tilde{k}$ could still lead to good estimates in these cases if used carefully.

Despite these results, KT still has several limitations when compared to FE as pointed out by Kathmann *et al*. When the polaritonic resonance lies in the frequency range that is thermally excited, such as with SiC and hBN, these contributions will dominate the radiative heat transfer. When the resonance is at much higher frequency, such as with noble metals, these modes are relatively unpopulated and a method such as FE is required to account for radiative transfer at lower frequencies. Another drawback of KT is that it cannot be readily applied to magnetic contributions to heat transfer, which may be important contributors in certain systems.

KT can, however, be a useful tool in some scenarios where it is difficult to apply FE. One of the reasons for the success of KT in studying phonon transport, for example, is that phonon dispersions may be calculated or experimentally determined and used as an input to KT [8]. Polaritonic dispersion relations for nanostructure arrays can also be simulated [80, 212] or accessed experimentally [213], permitting KT to make heat transfer

predictions from these data. Additionally, material structures in anisotropic or nonhomogeneous environments [89] would be difficult to analyze with FE but are much more accessible with KT. KT should therefore continue to be a useful tool in the analysis of heat transfer by propagating surface modes.

CHAPTER 7. CONCLUDING REMARKS

In this dissertation, NFRHT in arrays of nanostructures supporting SPs is examined from several perspectives. On the experimental side, the thermal properties of packed beds of SiO_2 nanoparticles are measured to identify contributions to thermal transport from coupled SPhP modes. The interstitial medium between the particles is modified with adsorbed water or an ethylene glycol coating to investigate the effect of the host medium permittivity. Results are compared to existing NFRHT models and a new scaling formalism to identify shortcomings of existing models. On the computational side, the KT and FE formalisms are used and improved to analyze NFRHT in arrays of different structures and materials. A new absorption spectra method for KT is developed to calculate SP dispersion relations from absorption spectroscopy data, and the method is used to propose a structure of doped plasmonic resonators embedded in an intrinsic semiconductor nanowire. Two different FE formalisms are shown to be mathematically equivalent, and a method to calculate radiative thermal conductivity from FE results is developed and applied to arrays of SiO_2 and SiC nanoparticles. To improve the computational efficiency of FE approaches, a system Green's function method is derived and validated that is analogous to efficient DDA codes. Finally, the KT and FE formalisms are compared to each other to understand the regimes of validity of KT. This chapter will summarize the findings from these studies as well as provide some recommendations for future work to build upon this dissertation.

7.1 Major Findings

The measurements of thermal properties of packed nanoparticle beds demonstrate that coupled SPhP modes in these systems may enhance the thermal conductivity by an

order of magnitude. The increases in thermal conductivity are observed when the interstitial medium is a high permittivity material, and these results cannot be easily explained by other heat transfer mechanisms. Because the nanoparticle beds have a low phonon thermal conductivity due to the high contact resistance between particles, and because they have a high surface area to volume ratio allowing for significant SPhP interactions, packed nanostructures are model systems for the observation and use of NFRHT in a bulk composite. In contrast to macroscale planar parallel surfaces, nanoparticle beds are fabricated and assembled quite easily without the need to maintain a small vacuum gap over a large area.

The new absorption spectra method for KT provides the dispersion relation of propagating SPs for chains of nanostructures in arbitrary nonhomogeneous environments. Importantly, the method uses experimental or simulated spectral response data instead of complicated Green's functions, which allows complex materials and geometries to be examined which were not previously accessible. Doped Si or InAs plasmonic resonators in intrinsic Si or InAs nanowires are capable of sub-diffractional waveguiding with group velocities and propagation lengths an order of magnitude greater than the same resonators suspended in an isotropic environment. Their radiative thermal conductivities can reach about 1 W m^{-1} K^{-1} for 10 nm diameter nanowires at 500 K, which is a higher thermal conductivity at a lower temperature than previous predictions for particle chains. This is comparable to the phonon and electron contributions to thermal transport, which are low in these structures due to boundary scattering in small nanowires.

The many-body method and the T-DDA formalisms of FE are shown to be mathematically equivalent. The T-DDA approach permits a more straightforward use of

the fluctuation-dissipation theorem, and the many-body method requires a reduced absorption factor in the fluctuation-dissipation theorem due to its definition of the induced and fluctuating dipole moments. A new method to calculate the radiative thermal conductivity from the particle-particle thermal conductance is applied to ordered chains, planes, and three-dimensional arrays of SiO_2 and SiC nanoparticles. Their radiative exchanges are strongly influenced by whether the materials support propagating SPs. Ordered nanoparticle chains always exhibit higher radiative thermal conductivities than disordered particle chains due to disruption of propagating modes or increased distance between particles. To address computational limitations of these methods, a system Green's function approach is developed and validated that should enable improvements in computational efficiency.

Comparing the KT and FE formalisms demonstrates that propagating SPs dictate the thermal electromagnetic interactions when these modes are present. This is shown by the agreement between the dispersion density of states and the energy density of spectral thermal emission for ordered SiC nanoparticle arrays, as well as by the agreement in radiative thermal conductivity predicted by the two methods when propagation lengths exceed the interparticle spacing. The success of KT with $\widetilde{\omega}$ in regimes of strong coupling demonstrates conclusively that KT can be a valid method to predict heat transfer by propagating SPs in linear chains of nanostructures.

The findings and methods presented here enhance the understanding of radiative heat transfer among many nanostructures. The structures analyzed, including packed nanoparticle beds and nanowires with repeated plasmonic resonators, could lead to a new class of materials in which NFRHT exceeds phonon/electron conduction. The nanowire

structures should present an opportunity to experimentally observe photonic conduction by surface plasmons. Theoretical clarifications on the use of the fluctuation-dissipation theorem should assist future researchers in its correct use for nanostructures or subvolumes modeled as point dipoles. New computational approaches, including the method of calculating radiative thermal conductivity from FE results and the system Green's function formalism, can help in the efficient design of systems that utilize thermal radiation as a significant form of heat transfer. Finally, the validation of KT when propagation lengths exceed the particle spacing demonstrates that it will continue to be a useful tool in the analysis of heat transfer by propagating SPs.

7.2 Recommendations for Future Work

These studies have identified several opportunities for continued work on NFRHT between nanostructures. A summary of some of the recommended avenues for future research is provided below.

- The packed nanoparticles measured in the experimental study could have included geometric effects such as water or ethylene glycol bridging between adjacent particles [150-153], which can alter both the phonon and radiation transport in these systems. Detailed computational studies of particles with water or glycol bridges, possibly with the system Green's function formalism, could provide deeper insight on thermal transport in these systems.
- Multipole effects could play a significant role in the near-field radiation between nanoparticles, especially at small spacings. However, these are generally not considered in the KT and FE formalisms. Some preliminary research has begun to

lay the groundwork to include multipole effects [92, 122], but additional research is needed to better develop and utilize these approaches.

- The results for the proposed nanowire structures demonstrate a pathway towards significant NFRHT in nanoengineered systems, but additional work is needed to identify ideal materials, geometries, and operating conditions for this transport mechanism. Future analytical work should focus on optimization of coupling between resonators, including investigating the impact of dopant concentration [193] and nonuniform/noncircular nanowire cross-sections. Future experimental efforts could focus on thermal conductivity measurements of single nanowires [194].
- The nanoparticle arrays examined here all contained uniform materials and particle sizes as well as limited disorder. Additional studies should focus on arrays with multiple particle materials and sizes and detailed studies of disorder, especially disordered arrays with close particle spacing.

APPENDIX A. PACKED PARTICLE EXPERIMENTAL DETAILS

A.1 Experimental Methods

Amorphous SiO_2 and polycrystalline Si nanoparticles were purchased from US Research Nanomaterials, Inc. and Sigma-Aldrich. Fourier-transform infrared (FTIR) attenuated transmission reflection (ATR) spectroscopy was performed on the as-received nanoparticles using a Perkin Elmer Spectrum 100 FTIR spectrometer with a Pike VeeMax II variable angle ATR attachment. Zinc selenide (index of refraction = 2.4) was chosen for the ATR crystal (the nanoparticles were compressed into films on this substrate). For frequencies greater 207 Trad s^{-1}, the refractive index for SiO_2 never exceeds 1.5, so the critical angle is 38.7° (or less). For frequencies less than 207 Trad s^{-1}, the refractive index of SiO_2 exceeds that of zinc selenide and has a large imaginary part resulting in high external reflection by the bulk SiO_2 even in the lower frequency range. Furthermore, diffuse reflectance results are also present in the nanoparticle bed spectra. Thus the FTIR-ATR spectra are combined ATR, external reflectance, and diffuse reflectance results.

Thermal conductivity, thermal diffusivity, and volumetric specific heat of packed nanoparticle beds were measured between -50 and 200 °C with the Hot Disk TPS 2500 S transient plane source thermal constants analyser following international standard ISO 22007-2. This standard has an established thermal conductivity measurement uncertainty range of 2-5%. The transient nature of the technique, combined with the transient plane source model used in the Hot Disk TPS 2500 S, allows thermal conductivity, thermal diffusivity, and specific heat to be measured independently. The measurement uncertainty range is 5-10% for thermal diffusivity and specific heat. The measurements were carefully

calibrated on materials with known properties, and made at least 3 times for each collected data point to minimize uncertainty. Nanoparticles were packed on both sides of a Kapton measurement sensor into a stainless-steel cylindrical holder with about 2 kPa. The nanoparticles were added to the holder in steps so that the 2 kPa weight could be used to compress the nanoparticles in increments to ensure even packing on both sides of the sensor. It is not expected that the nanoparticles are packed into perfect crystals, so there should be some natural variations in packing geometry in reproduced experiments.

For the adsorbed water system, The Hot Disk measurement sensor and sample holder containing the nanoparticles were placed in a Tenney Junior environmental test chamber to control the sample temperature. The samples were dried in the environmental chamber before each test by flowing dry air at 150 °C for at least 1 hour (except for the tests in Figure A.1(b) inset to compare), to establish an air interface at the nanoparticle surfaces. The airflow was stopped, and the chamber closed, to begin measurements. Each sample was measured for three consecutive temperature sweeps from 150 to -50 °C, -50 to 150 °C, and 150 to -50 °C. The samples were held at each measurement set point for about 1 hour to reach steady state, and 30-60 min to collect data from several measurements. Using three temperature sweeps allowed adsorbed water to return in the second, increasing temperature sweep to increase the relative permittivity of the medium at the nanoparticle surface interface. Relative humidity in the chamber was measured with an Omega HX15-W High-Temperature Relative Humidity/Temperature Transmitter, and humidity ratio was calculated from measured relative humidity, measured temperature, and ambient pressure. The humidity ratio uncertainties are maximum values for each given range calculated by propagation of uncertainty. The chamber humidity ratio was between 1% and 3% $\pm$ 0.3%

during the second sweep; the amount of humidity was undetectable in the two decreasing temperature sweeps. The third temperature sweep was intended to reveal any hysteresis, and none was observed. The data collected at higher chamber humidity (up to 18.7% $\pm$ 2.7% humidity ratio) in Figure 3.3(b) was obtained by placing a water-soaked sponge in the chamber during an increasing temperature test.

The ethylene glycol coated nanoparticles were prepared with a solution chemistry process. 4.8 g of as-received nanoparticles were mixed with 60 equivalents ethylene glycol (267 mL) or with 30 equivalents ethylene glycol (134 mL) and 100 equivalents deionized water (144 mL). Ethylene glycol was purchased from Sigma-Aldrich and McMaster-Carr. The solution was heated and stirred at 105-115 °C for 4 hours, cooled, and centrifuged at 25,000 rpm for 20 min to separate the coated nanoparticles. The resulting samples were baked in a dry environment at 115 °C for 4 hours to remove any remaining water. Thermal properties were measured with a similar method as the uncoated nanoparticles. Testing began at 0 °C or ambient temperature and proceeded in increasing temperature steps. Near the boiling point of ethylene glycol, thermal conductivity sharply decreased as shown in Figure 3.4(a). Measurements at 200 °C are only reported for the datasets in which thermal conductivity had stabilized by the time of the measurement. When a stable measurement was obtained at 200 °C, an additional measurement was then taken at 190 °C to show the return to the phonon value of thermal conductivity of SiO_2 nanoparticle beds. The loss of ethylene glycol near the boiling point suggests that the nanoparticles were coated through hydrogen bonding interactions. Weight measurements before and after testing along with thermogravimetric analysis show the samples typically consisted of about 40% SiO_2 by

weight. The differential scanning calorimetry measurement was performed with a TA Instruments Q2000 DSC.

A.2 Reproducibility of Thermal Conductivity Measurements

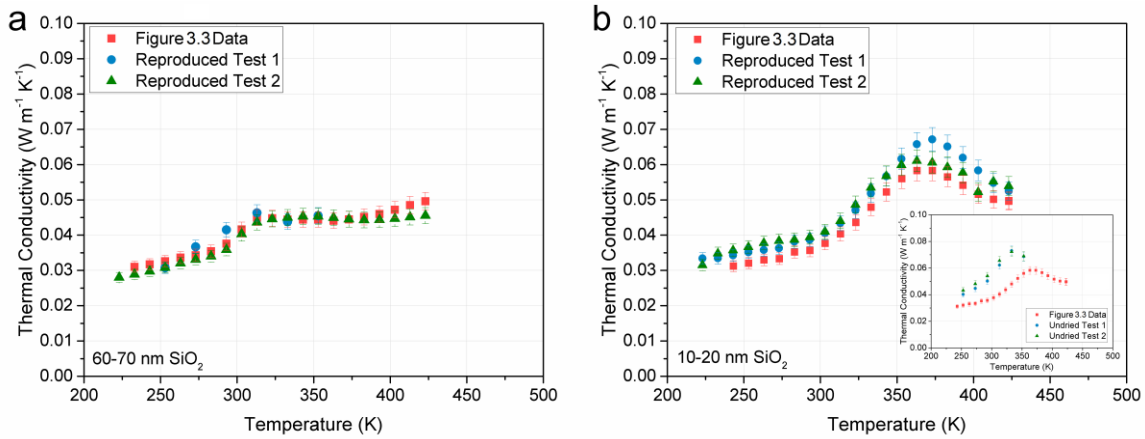

Figure A.1. Reproduced thermal conductivity measurements of packed SiO_2 nanoparticles in a humid environment.

The thermal conductivity of SiO_2 nanoparticles 60-70 nm in diameter as a function of temperature is shown in Figure A.1(a). The SPhP red square data are from Figure 3.3(a). The two reproduced experiments were conducted at different times, with fresh nanoparticles each time, over the span of one year. The thermal conductivity of SiO_2 nanoparticles 10-20 nm in diameter as a function of temperature is shown in Figure A.1(b). The red square data are from Figure 3.3(b). The two reproduced experiments were conducted at different times, with fresh nanoparticles each time, over the span of one year. The inset shows two reproduced experiments conducted prior to the measurements in Figure 3.3(b), both with fresh nanoparticles. The nanoparticles were not dried before the test to collect the data in the inset, which increased the content of adsorbed water similarly to the high humidity data in Figure 3.3(b). The error bars in all measurements are +/- 5%

based on the uncertainty of the measurement technique, which is greater than the standard deviation of several measurements at each temperature.

A.3 Thermal Conductivity of Packed Si Nanoparticle Beds

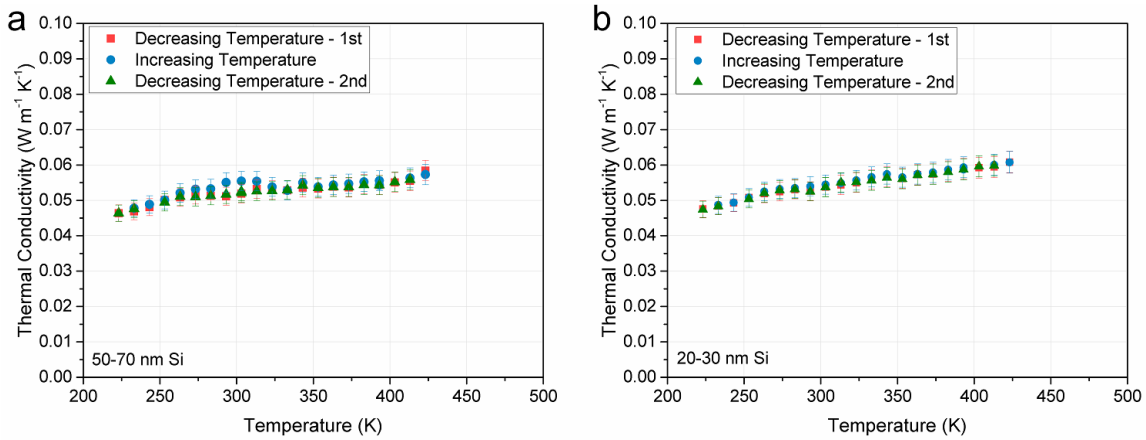

Figure A.2. Thermal conductivity measurements of packed Si nanoparticles.

The thermal conductivity of Si nanoparticles 50-70 nm in diameter as a function of temperature is shown in Figure A.2(a). The thermal conductivity of Si nanoparticles 20-30 nm in diameter as a function of temperature is shown in Figure A.2(b). The error bars in all measurements are +/- 5% based on the uncertainty of the measurement technique, which is greater than the standard deviation of several measurements at each temperature. The data for three consecutive temperature sweeps as described in Appendix A.1 overlap within the experimental uncertainty for each data set. The lack of a departure from the linear trend in the temperature increase is evidence that adsorbed water does not play a role in heat transfer through the bed.

A.4 Specific Heat of Packed SiO_2 Nanoparticle Beds

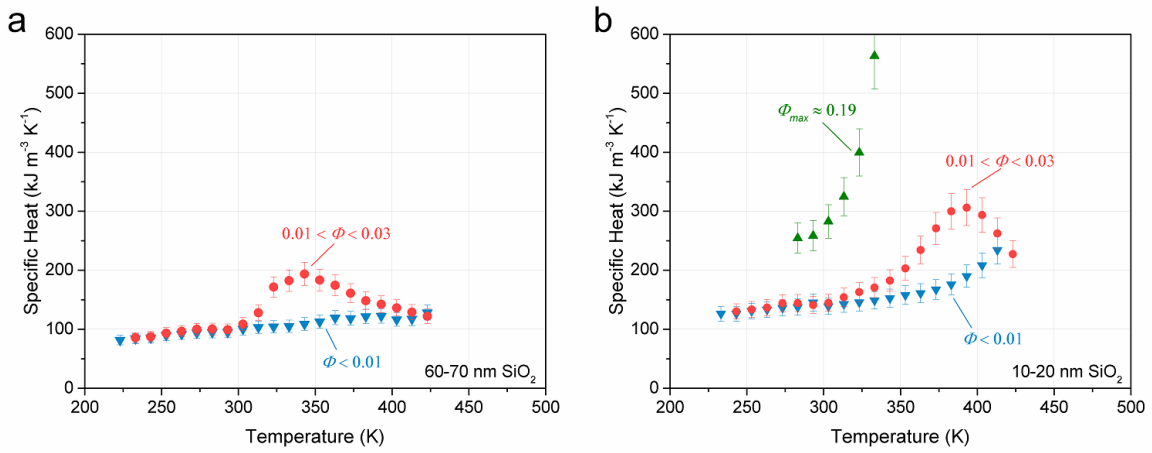

Figure A.3. Specific heat measurements of packed SiO_2 nanoparticles in a humid environment

The measured specific heat of SiO_2 nanoparticles 60-70 nm diameter as a function of temperature is shown in Figure A.3(a). This is the same sample as shown in Figure 3.3(a). The measured specific heat of SiO_2 nanoparticles 10-20 nm diameter as a function of temperature is shown in Figure A.3(b). This is the same sample as shown in Figure 3.3(b). The specific heat with water adsorbed (the higher humidity ratio data sets) includes contributions from the SPhP specific heat, phonon specific heat, and adsorbed water. Similarities in shape to the thermal conductivity data in Figure 3.3 suggest that SPhPs may affect the specific heat, as well as possible contributions from the presence of adsorbed water and phase change. The peaks in specific heat are not at the same locations as the peaks in thermal conductivity, which illustrates the independence of the thermal conductivity and specific heat measurements. These trends have additionally been validated with Differential Scanning Calorimetry measurements. The data sets for each SiO_2 sample correspond to consecutive temperature sweeps as described in Appendix A.1.

The error bars in all measurements are +/- 10% based on the uncertainty of the measurement technique, which is greater than the standard deviation of several measurements at each temperature. The peaks in the temperature dependent specific heat correspond to the release of adsorbed molecular water layers.

A.5 Specific Heat of Packed Si Nanoparticle Beds

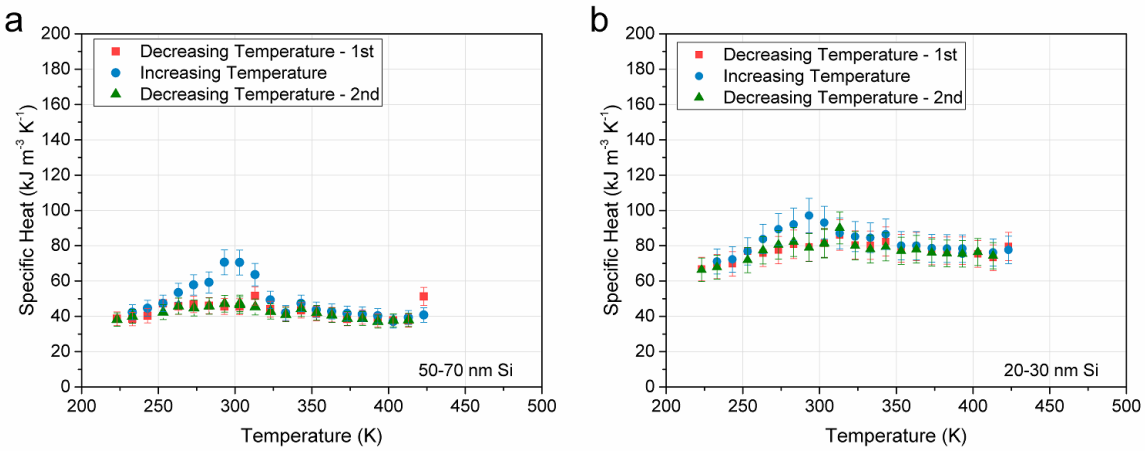

Figure A.4. Specific heat measurements of packed Si nanoparticles.

The measured specific heat of Si nanoparticles 50-70 nm diameter as a function of temperature is shown in Figure A.4(a). The measured specific heat of Si nanoparticles 20-30 nm diameter as a function of temperature is shown in Figure A.4(b). The three data sets for each sample correspond to three consecutive temperature sweeps as described in Appendix A.1. The error bars in all measurements are +/- 10% based on the uncertainty of the measurement technique, which is greater than the standard deviation of several measurements at each temperature. The magnitudes of these specific heat data are close to half the magnitudes of values for specific heat data for SiO_2, so the contribution of the specific heat of adsorbed water could be larger in this case. The peaks in specific heat are

not accompanied by a peak in thermal conductivity (Figure A.2), which differs from the case for SiO_2. The peaks in specific heat are attributed to the transition from solid to liquid water, which increases the water specific heat by about two times [214], and then the loss in water content from its incremental release at increased temperatures.

A.6 SPhP Dispersion in a Chain of Nanoparticles

The simplified equation for the SPhP dispersion relation for a chain of polar nanoparticles is given by Equation (3.3). This equation contains an infinite summation representing the number of nanoparticles to include in the dispersion, but in these calculations only the first five terms are used. To show that higher terms are negligible, the dispersion relation for N = 1 to N = 5 terms is plotted in Figure A.5, which clearly shows convergence for N = 5.

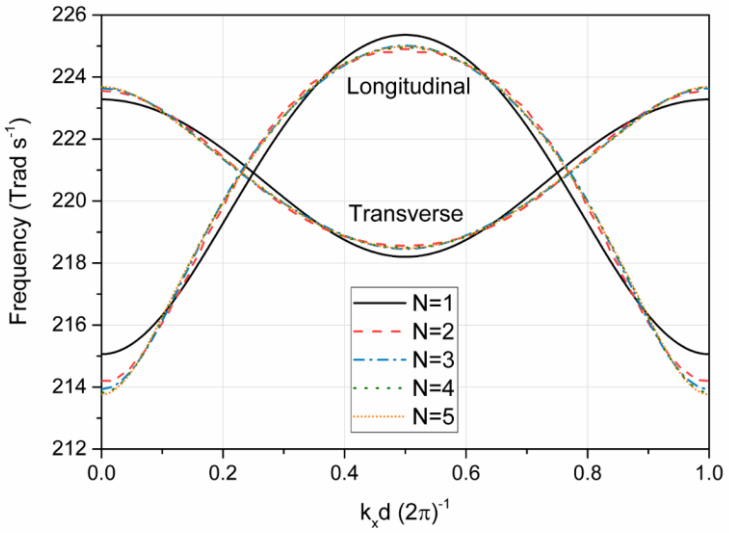

Figure A.5. SPhP dispersion for 65 nm diameter SiO_2 particles in contact for various numbers of nearest neighbors included in the summation.

A.7 Modeling Details for Comparison to Experiments

The slope of the dispersion curves shows that the wave coupling between nanoparticles can carry energy along the chain. This motivates the KT model of thermal conduction by SPhP wave propagation along nanoparticle chains. The equation for one-dimensional diffusive thermal conductivity in this scenario developed by Ben-Abdallah *et al.* [92] is

$$\kappa = \frac{1}{\pi A_c}\frac{\hbar^2}{k_B T^2}\sum_p \int_0^{Br} v_g^2(k)\gamma(k)\omega^2(k)\frac{e^{\hbar\omega/k_B T}}{(e^{\hbar\omega/k_B T}-1)^2}\,dk \tag{A.1}$$

where A_c, T, Br, v_g, and γ are the cross-sectional area of the chain, temperature, edge of the first Brillion zone $2\pi/d$, group velocity, and mode lifetime. The mode lifetime can be simply approximated as $\gamma = 2/\Gamma$ [25], where Γ is the damping constant (8.92 Trad s^{-1} for SiO_2). Together, the group velocity times the mode lifetime $v_g\gamma$ is the same as the propagation length [215] Λ (mean free path), which is related to the probability of transmission in the diffusive regime [147] by $\mathcal{T} = \Lambda/\mathrm{L}$ where L is the length of the system. This leads to a strong dependence on the group velocities in the dispersion, which can be seen by the dispersion and calculated thermal conductivity curves in Figure 3.7 and Figure 3.8. When the dispersion occupies a narrower frequency range (higher density of states) when the medium permittivity increases, the group velocities decrease, causing the thermal conductivity to drop. Note that the thermal conductivity equation in three-dimensions (the system examined here) will have the same dependence on group velocity and mode lifetime [147]. The propagation lengths based on the group velocities in the dispersion relation are plotted below for a chain of 65 nm diameter SiO_2 particles in contact with a medium relative permittivity of $\varepsilon_m = 1$ and $\varepsilon_m = 4$. The results show that the propagation lengths

are on the order of the nanoparticle spacing, which raises doubts about the applicability of a propagating wave model.

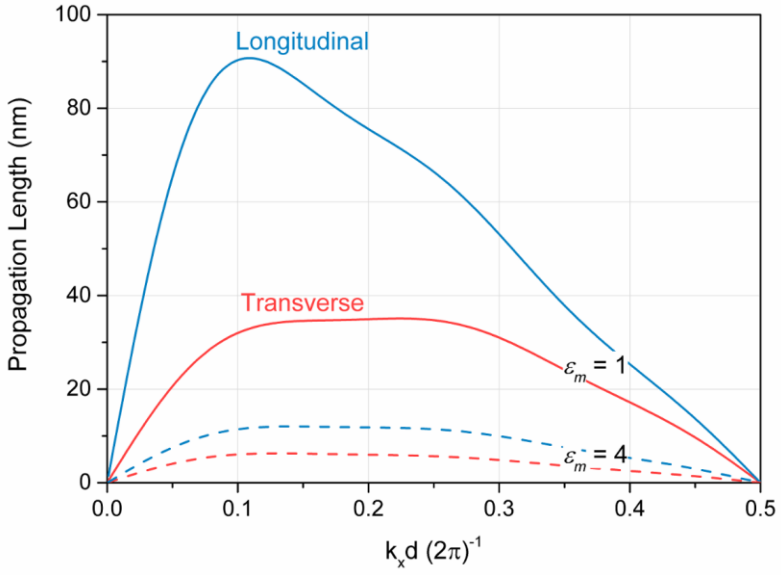

Figure A.6. Propagation lengths for a chain of 65 nm diameter SiO_2 nanoparticles in contact in two different media.

An alternative method of calculating thermal conductivity in a nanoparticle bed is through the FE formalism or many-body method as described in Section 2.3.2. To extend this method to find thermal conductivity, first an equation is expressed for the total heat flux along a chain of N nanoparticles with a temperature gradient along the chain axis dT/dx:

$$Q = \sum_{i=1}^{N-1} \sum_{j=i+1}^{N} G_{ij} \frac{dT}{dx} d(j-i) \tag{A.2}$$

where G_{ij} is the thermal conductance between the ith and jth nanoparticles and d is the inter-particle spacing. Using Fourier's law, the thermal conductivity is then

$$\kappa = \frac{d}{A_c} \sum_{i=1}^{N-1} \sum_{j=i+1}^{N} G_{ij}\,(j-i) \tag{A.3}$$

This equation was used to find the thermal conductivity curves plotted in Figure 3.8. $N = 61$ nanoparticles was used for the calculations and was check to ensure convergence.

An explanation for why this model predicts declining thermal conductivity with increasing medium permittivity can be found by examining the model's dependence on the nanoparticle polarizability. The thermal conductance between the *i*th and *j*th nanoparticles depends on a transmission coefficient, given by Ben-Abdallah *et al.* as [114]

$$\mathcal{T}_{ij}(\omega) = \frac{4}{3}\frac{\omega^4}{c^4}\mathrm{Im}(\alpha_i)\mathrm{Im}\big(\alpha_j\big)\mathrm{Tr}\big[\mathbb{G}_{ij}\mathbb{G}_{ij}^{\dagger}\big] \tag{A.4}$$

where $\mathbb{G}_{ij}$ is the system dyadic Green's function between the two nanoparticles. When the imaginary part of the polarizability decreases, the transmission coefficient will also decrease. For SiO_2 nanoparticles in the frequency range of interest, the polarizability will decrease with increasing medium permittivity. This is shown graphically below by the spectral Clausius-Mossotti polarizability for a 65 nm diameter SiO_2 particle. The solid lines are the real part of the polarizability and the dashed lines are the imaginary part. Curves are given for values of medium relative permittivity of 1, 3, and 5 (blue). As the medium permittivity increases, the average imaginary permittivity also decreases, which leads to the drop in thermal conduction predicted by the many-body radiation model.

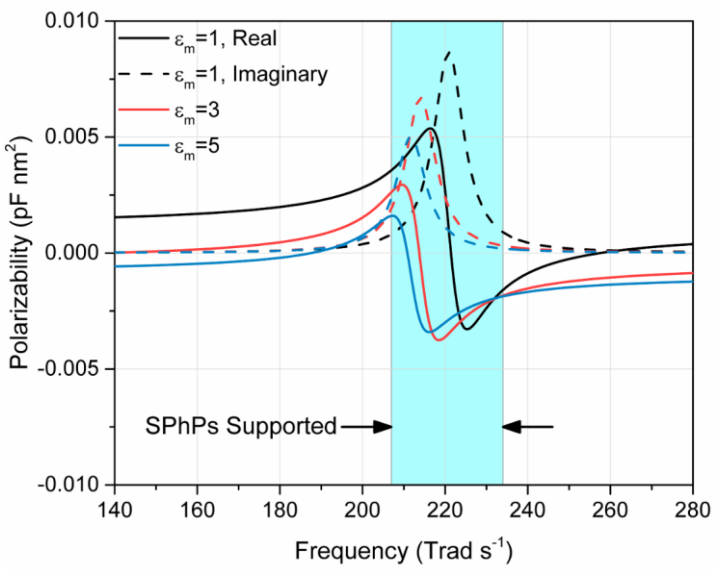

Figure A.7. Clausius-Mossotti polarizability of 65 nm diameter SiO_2 nanoparticles.

APPENDIX B. DETAILS OF ABSORPTION SPECTRA MODEL

B.1 Derivation of Dispersion Relation

For N identical plasmonic resonators in a chain modeled as harmonic oscillators [81, 160] with center-to-center spacing d, displacement **x**, restoring force spring constant K, effective mass m, and damping coefficient ζ, a force balance on the nth resonator leads to the equation of motion

$$\sum_{j=1}^{N} B_j\left(x_{n-j} + x_{n+j}\right) = m\frac{d^2x_n}{dt^2} + \zeta\frac{dx_n}{dt} + Kx_n \tag{B.1}$$

where N is the number of neighboring resonators to consider, $B_j x_{n\pm l}$ is the force exerted by the jth neighbor on the nth resonator, and the vector notation in **x** is removed because only longitudinal polarization is considered. Introducing the coupling strength of the jth neighbor with the nth resonator $\omega_{c,j} = \sqrt{B_j/m}$, the dipole moment $p = qx$ where q is the charge, the damping ratio $\xi = \zeta/m$, and the natural frequency $\omega_1 = \sqrt{K/m}$, Equation (4.1) is obtained and repeated here:

$$\sum_{j=1}^{N} \omega_{c,j}^2\left(p_{n-j} + p_{n+j}\right) = \frac{d^2p_n}{dt^2} + \xi\frac{dp_n}{dt} + \omega_1^2 p_n \tag{B.2}$$

Propagating wave solutions to this equation are sought of the form $p_{n\pm j} = P\mathrm{e}^{-\Gamma t - i[k(n\pm j)d - \omega t]}$, where P is the amplitude, k is the wavevector, ω is the real part of the complex frequency, and Γ is the imaginary part of the complex frequency

corresponding to the spectral damping rate. Inserting this into Equation (B.2), evaluating the time derivatives, and simplifying results in

$$\sum_{j=1}^{N} \omega_{c,j}^2 \left(\mathrm{e}^{ikjd} + \mathrm{e}^{-ikjd}\right) = (-\Gamma + i\omega)^2 + (-\Gamma + i\omega)\xi + \omega_1^2 \tag{B.3}$$

Using the trigonometric identity $\cos y = \left(\mathrm{e}^{ix} + \mathrm{e}^{-ix}\right)/2$ and rearranging the right side allows this to be rewritten as

$$2\sum_{j=1}^{N} \omega_{c,j}^2 \cos(kjd) = \Gamma(\Gamma - \xi) - \omega^2 + \omega_1^2 + i\omega(\xi - 2\Gamma) \tag{B.4}$$

Separating the real and imaginary parts results in the dispersion relation given in Equation (4.2):

$$\begin{gathered} 0 = \omega^2 - \Gamma(\Gamma - \xi) - \omega_1^2 + 2\sum_{j=1}^{N} \omega_{c,j}^2 \cos(kjd) \text{ (Real)} \\ 0 = 2\Gamma - \xi \text{ (Imaginary)} \end{gathered} \tag{B.5}$$

B.2 Coupling Strength

For two nanoscale resonators a and b separated by a distance much less than the resonant wavelength, such that the incident illumination exerts the same force $F(t) = F_0 \mathrm{e}^{i\omega t}$ on the resonators, the coupled equations of motion for each resonator are

$$F_0 e^{i\omega t} + Bx_b = m\frac{d^2x_a}{dt^2} + \zeta\frac{dx_a}{dt} + kx_a$$
$$F_0 e^{i\omega t} + Bx_a = m\frac{d^2x_b}{dt^2} + \zeta\frac{dx_b}{dt} + kx_b \tag{B.6}$$

One method to find solutions to these coupled equations is to take linear combinations of them. Adding the equations and introducing $z = x_a + x_b$ yields

$$\frac{2F_0}{m} e^{i\omega t} + \omega_c^2 z = \frac{d^2z}{dt^2} + \xi\frac{dz}{dt} + \omega_1^2 z \tag{B.7}$$

where the previous definitions of ω_c, ξ, and ω_1 have been used. Solutions to this equation take the form $z(t) = Ce^{i\omega t}$. Inserting this and solving for C yields

$$C = \frac{2F_0/m}{(\omega_1^2 - \omega_c^2) - \omega^2 + i\omega\xi} \tag{B.8}$$

The amplitude of oscillation is therefore given as

$$|C| = \sqrt{C \cdot C^*} = \frac{2F_0/m}{(\omega_1^2 - \omega_c^2 - \omega^2)^2 + \omega^2\xi^2} \tag{B.9}$$

and the phase is

$$\tan(\phi) = \frac{\mathrm{Im}(C)}{\mathrm{Re}(C)} = -\frac{\xi\omega}{\omega_1^2 - \omega_c^2 - \omega^2} \tag{B.10}$$

which allows the solution to the coupled equation of motion to be written as $z(t) = |C|e^{i\phi}e^{i\omega t}$. Only the real part of the force and the solution, however, is physical. The power delivered to the two oscillators is then expressed as

$$\dot{W}(t) = \mathrm{Re}[F(t)]\mathrm{Re}\left[\frac{dz}{dt}\right] = -F_0\omega|C|\cos(\omega t)\sin(\omega t + \phi) \tag{B.11}$$

When this is averaged over once period of oscillation the following is obtained:

$$\langle\dot{W}(t)\rangle = \frac{F_0^2}{\xi m}\cdot\frac{\xi^2\omega^2}{\xi^2\omega^2 + (\omega_0^2 - \omega_c^2 - \omega^2)^2} \tag{B.12}$$

The measured or simulated absorption peak corresponds to $d\langle\dot{W}(t)\rangle/d\omega = 0$, which provides the coupling strength to be defined as

$$\omega = \omega_2 = \sqrt{\omega_1^2 - \omega_c^2} \tag{B.13}$$

B.3 Absorption Spectra and Dispersion with Strong Coupling

The absorption efficiency spectra calculated from the discrete dipole approximation are plotted in Figure B.1(a) for SiC nanoparticles embedded in a background material of permittivity $\varepsilon_m = 1$ and Figure B.1(b) for SiO_2 nanoparticles embedded in a background material of permittivity of $\varepsilon_m = 4$. The particles are 12 nm in diameter and separated by distances S of 4, 6, 8, and 10 nm. The spectrum for a single particle is also shown in black, which is used for comparison to the results from Mie theory shown in Figure B.2. As S decreases, the coupling strength and shift in absorption peak from the single particle case increase.

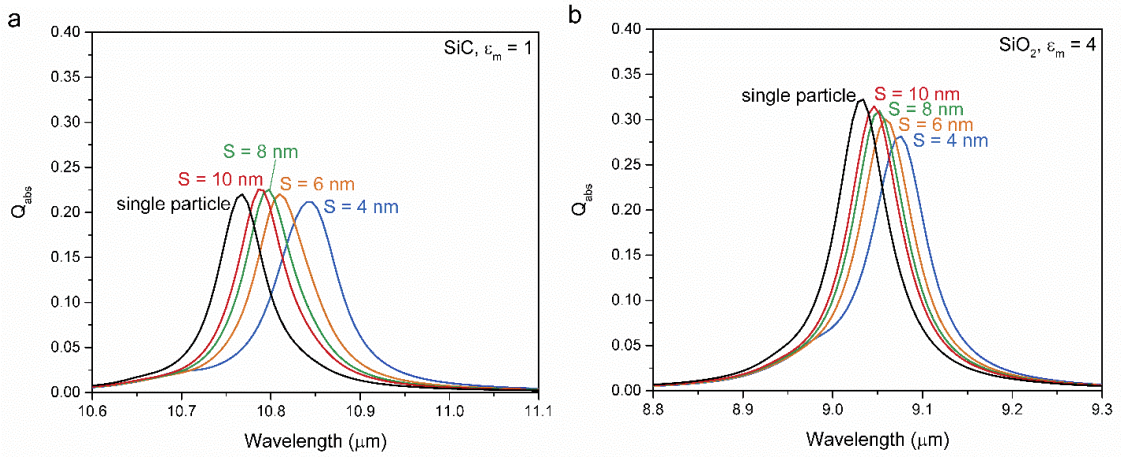

Figure B.1. Absorption efficiency calculated from the DDA for 12 nm diameter (a) SiC particles in ε_m = 1 and (b) SiO_2 particles in ε_m = 4.

The absorption efficiency spectra calculated from Mie theory [78, 171] for a 12 nm diameter SiC nanoparticle embedded in a background material of permittivity $\varepsilon_m = 1$ is plotted in Figure B.2 (a) and a SiO_2 nanoparticle embedded in a background material of permittivity of $\varepsilon_m = 4$ in Figure B.2(b). The absorption peaks agree well with the results from the discrete dipole approximation shown in Figure B.1.

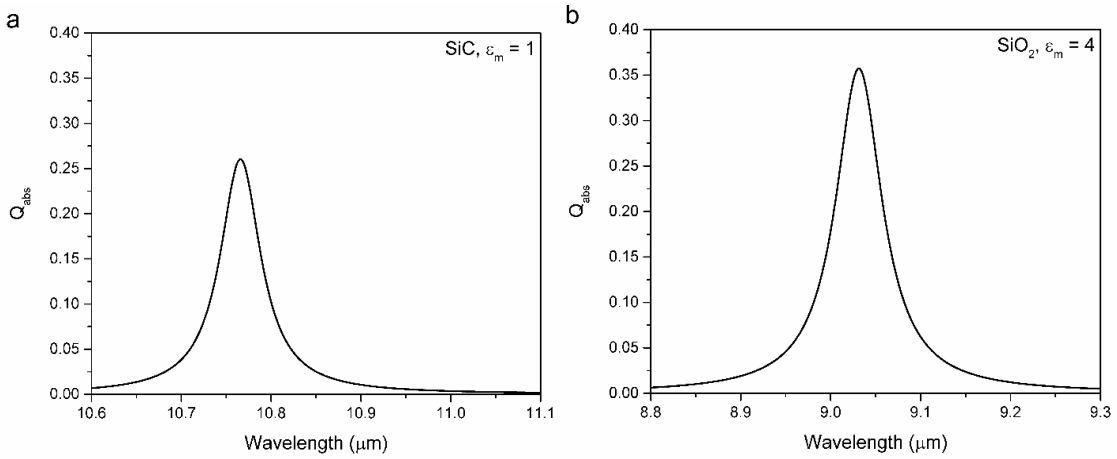

Figure B.2. Absorption efficiency calculated from Mie theory for 12 nm diameter (a) SiC particles in ε_m = 1 and (b) SiO_2 particles in ε_m = 4.

The dispersion relation for a doped Si resonator chain in an intrinsic Si nanowire with N_e = 1×10^{21} cm^{-3}, AR = 0.8, S = 10 nm, and a diameter of 150 nm is plotted in Figure B.3. The light line in intrinsic Si is also shown. For resonators that exhibit very strong coupling, such as these, the dispersion becomes very steep at low frequencies and wavevectors, such that the group velocities exceed the speed of light in the medium. These portions of the dispersion relation are therefore removed from the solution.

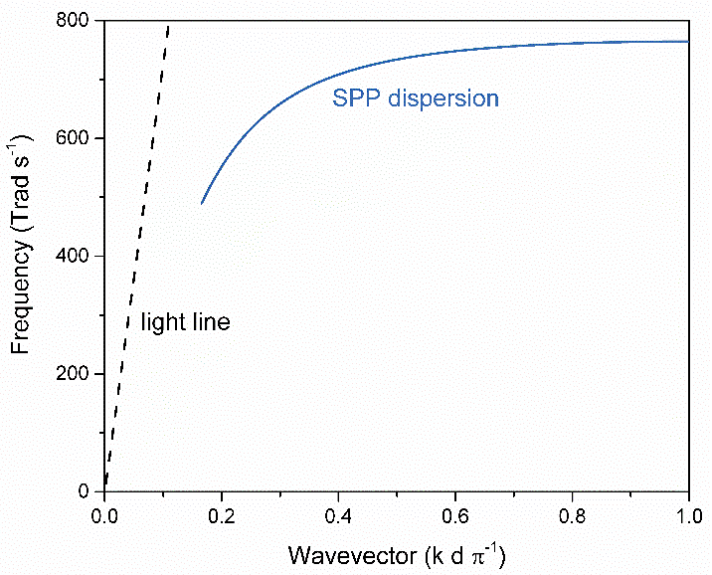

Figure B.3. Dispersion for doped Si resonators in an intrinsic Si nanowire with very strong coupling.

B.4 Plasmon Ruler Equation and Contributions to Thermal Transport

The contribution of $\omega\, \partial f_{BE}/\partial T$ factors to the radiative thermal conductivity are shown in Figure B.4 for varying frequency and temperature. This shows that lower energy propagating modes are preferable for thermal transport.

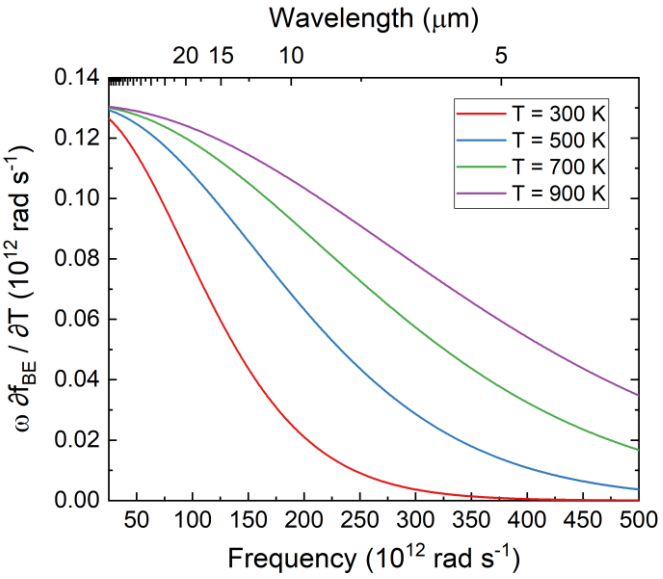

Figure B.4. Frequency and Bose-Einstein distribution contributions to the thermal conductivity.

The impact of separation distance on photonic thermal conductivity for InAs and Si nanowires with $D = 100$ nm and $L = 100$ nm is plotted in Figure B.5. Although distances are shown down to 1 nm, in this small regime the near-field radiation formalism is questionable, so all other calculations are performed at $S = 5$ nm.

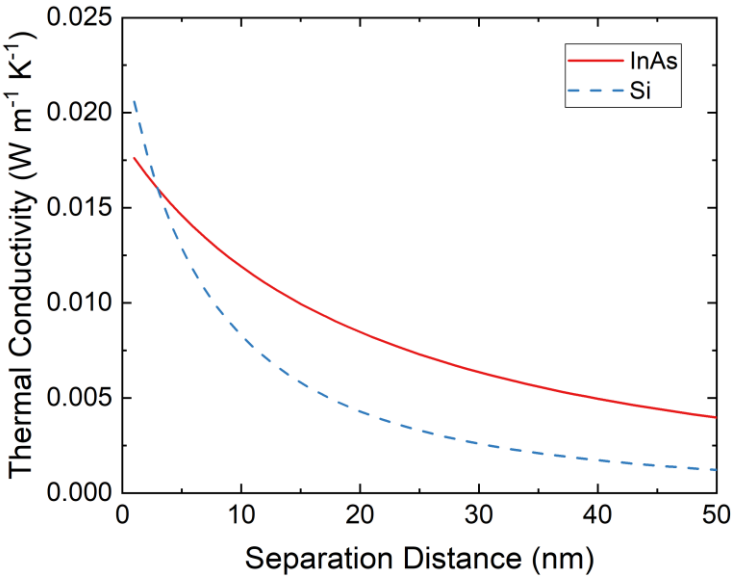

Figure B.5. Impact of separation distance on photonic thermal conductivity for InAs and Si nanowire systems.

The decay length scaling factor for InAs and Si nanowires is plotted in Figure B.6 as a function of nanowire diameter for either fixed resonator length or fixed resonator aspect ratio, with $S = 5$ nm in all cases. Diameter has little effect as long as the aspect ratio is constant, but τ decreases with increasing AR as D decreases.

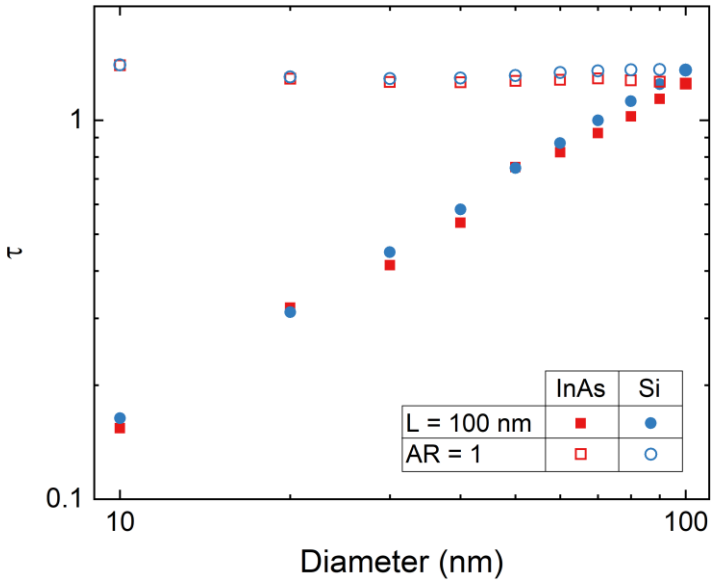

Figure B.6. Decay length scaling factor for InAs and Si nanowires as a function of nanowire diameter.

The proportionality constant in the plasmon ruler equation is plotted in Figure B.7 for InAs and Si nanowires as a function of nanowire diameter for either fixed resonator length or fixed resonator aspect ratio, with $S = 5$ nm in all cases. A_0 increases substantially as AR increases, which tends to increase photonic conduction.

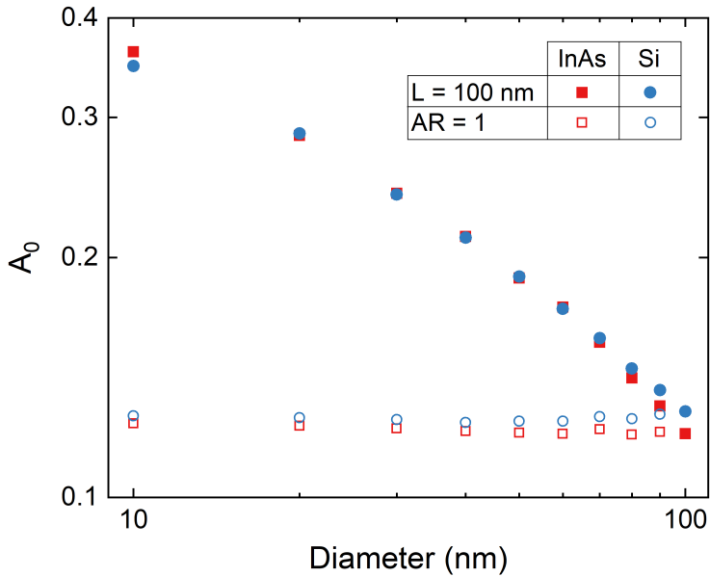

Figure B.7. Proportionality constant in plasmon ruler equation InAs and Si nanowires as a function of nanowire diameter.

The single resonator peak absorption frequency for InAs nanowires is plotted in Figure B.8 as a function of nanowire diameter for either fixed resonator length or fixed resonator aspect ratio. Lower frequency resonances with larger AR increase thermal transport.

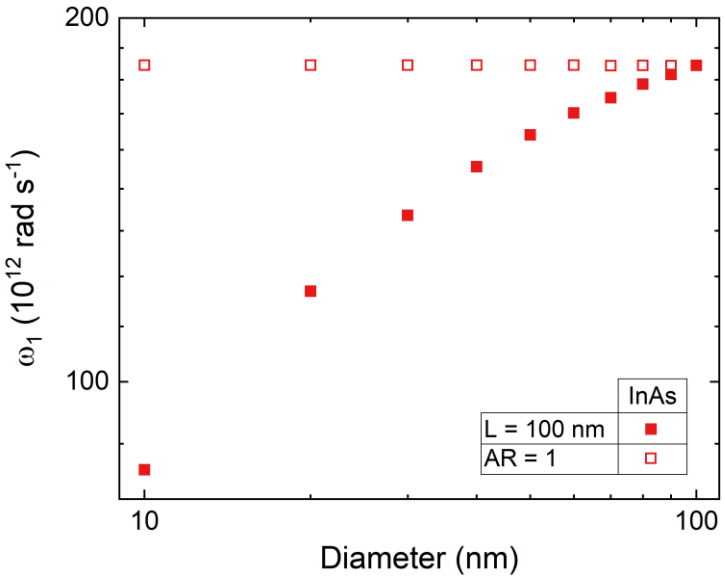

Figure B.8. Single resonator peak absorption frequency for InAs nanowires as a function of nanowire diameter.

The single resonator peak absorption frequency for Si nanowires is plotted in Figure B.9 as a function of nanowire diameter for either fixed resonator length or fixed resonator aspect ratio. Lower frequency resonances with larger AR increase thermal transport.

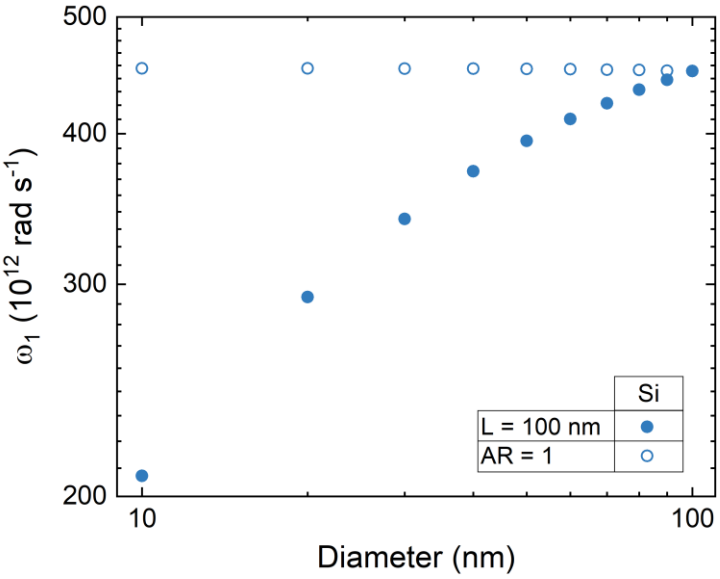

Figure B.9. Single resonator peak absorption frequency for Si nanowires as a function of nanowire diameter.

The propagation lengths and spectral thermal conductivity are plotted in Figure B.10 for InAs nanowires with three different diameters as either $L = 100$ nm (solid lines) or $AR = 1$ (dashed lines) is held constant. The axes share common scales with Figure B.11 for comparison. Although propagation length decreases with diameter, the thermal conductivity increases due to its inverse proportionality to nanowire area and the shift of the dispersion to lower frequencies when $L = 100$ nm.

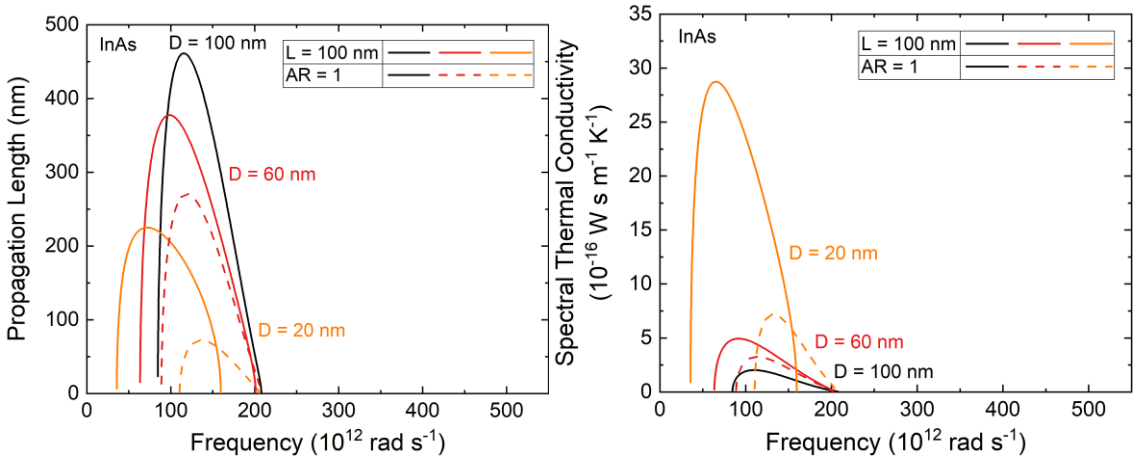

Figure B.10. (a) Propagation lengths and (b) spectral thermal conductivity for InAs nanowires with three different diameters.

The propagation lengths and spectral thermal conductivity are plotted in Figure B.11 for Si nanowires with three different diameters as either $L = 100$ nm (solid lines) or $AR = 1$ (dashed lines) is held constant. The axes share common scales with Figure B.10 for comparison. Similar effects are seen with InAs nanowires in Figure B.10.

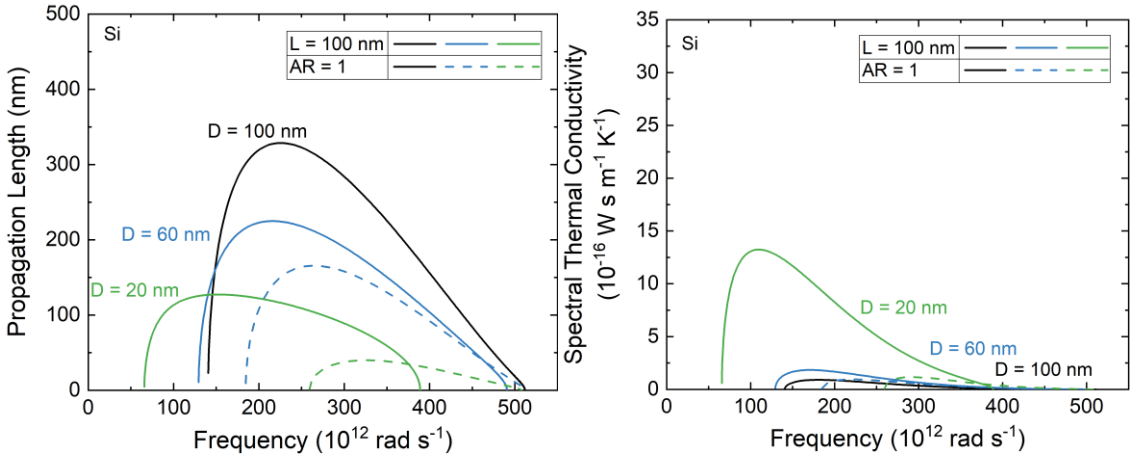

Figure B.11. (a) Propagation lengths and (b) spectral thermal conductivity for Si nanowires with three different diameters.

APPENDIX C. DERIVATIONS FOR MANY-DIPOLE FLUCTUATIONAL ELECTRODYNAMICS

C.1 Dipole Moments in the T-DDA

For completeness a derivation is shown here of the induced part of the dipole moment shown in Equation (5.7) as well as the fluctuating part as used in the T-DDA. To begin, the differential forms of Faraday's law and Ampère's law in the ith particle or subvolume are

$$\begin{aligned} \nabla \times \mathbf{E}_i &= i\omega\mu_0 \mathbf{H}_i \\ \nabla \times \mathbf{H}_i &= \mathbf{J}_i^{(\mathrm{fl})} + \mathbf{J}_i^{(\mathrm{ind})} - i\omega\varepsilon_0 \varepsilon_i' \mathbf{E}_i \end{aligned} \tag{C.1}$$

where the currents $\mathbf{J}_i^{(\mathrm{fl})}$ and $\mathbf{J}_i^{(\mathrm{ind})}$ have been split into parts due to thermal fluctuations and due to the electric field, and ε_i' is the real part of the relative permittivity. With the constitutive relation $\mathbf{J}_i^{(\mathrm{ind})} = \sigma \mathbf{E}_i$, where σ is the electrical conductivity, and the definition of the complex relative permittivity $\varepsilon_i = \varepsilon_i' + i\frac{\sigma}{\omega\varepsilon_0}$, Ampère's law may be rewritten as

$$\nabla \times \mathbf{H}_i = \mathbf{J}_i^{(\mathrm{fl})} - i\omega\varepsilon_0 \varepsilon_i \mathbf{E}_i \tag{C.2}$$

Taking the curl of Faraday's law and using Ampère's law, the vectorial wave equation is obtained:

$$\nabla \times \nabla \times \mathbf{E}_i - k_0^2 \varepsilon_i \mathbf{E}_i = i\omega\mu_0 \mathbf{J}_i^{(\mathrm{fl})} \tag{C.3}$$

where $k_0^2 = \omega^2 \mu_0 \varepsilon_0$. This may be written in terms of an equivalent source current as

$$\nabla \times \nabla \times \mathbf{E}_i - k_0^2 \varepsilon_m \mathbf{E}_i = i\omega\mu_0 \mathbf{J}_i^{(\mathrm{eq})} \tag{C.4}$$

where

$$\mathbf{J}_i^{(\mathrm{eq})} = -i\omega\varepsilon_0(\varepsilon_i - \varepsilon_m)\mathbf{E}_i + \mathbf{J}_i^{(\mathrm{fl})} \tag{C.5}$$

When the volume of the ith particle or subvolume is much smaller than the thermal wavelength, it may be modeled as a point dipole. The dipole moment is related to the current by [25]

$$\mathbf{p}_i = \frac{i}{\omega}\int_{V_i} \mathbf{J}_i dV \tag{C.6}$$

Inserting Equation (C.5) into Equation (C.6), the definition of the total dipole moment is obtained:

$$\mathbf{p}_i = \underbrace{V_i\varepsilon_0(\varepsilon_i - \varepsilon_m)\mathbf{E}_i}_{\mathbf{p}_i^{(\mathrm{ind})}} + \underbrace{\frac{i}{\omega}\int_{V_i} \mathbf{J}_i^{(\mathrm{fl})} dV}_{\mathbf{p}_i^{(\mathrm{fl})}} \tag{C.7}$$

In Equation (C.7), the induced and fluctuating parts of the dipole moment are shown, and the bare polarizability $\alpha_i^{(0)} = V_i(\varepsilon_i - \varepsilon_m)$ appears in the induced part as shown in Equation (5.7).

C.2 Fluctuation-Dissipation Theorem from Thermal Currents

Equation (5.20) provides the fluctuation-dissipation theorem in terms of the particle bare polarizability as derived in reference [197] and summarized in reference [15]. This

equation may also be derived directly from the fluctuation-dissipation theorem for the thermal currents as done in reference [51]. The fluctuation-dissipation theorem [24, 195, 196] for the convention of the Fourier transform chosen is

$$\langle J_{j,\gamma}^{(\mathrm{fl})}(\omega) J_{j',\gamma'}^{(\mathrm{fl})*}(\omega')\rangle = 4\pi\hbar\omega^2\varepsilon_0 f^{(\mathrm{BE})}\left(\omega, T_j\right)\mathrm{Im}\left(\varepsilon_j\right)\delta_{jj'}\delta_{\gamma\gamma'}\delta(\omega-\omega') \qquad \text{(C.8)}$$

Assuming a small enough volume such that the current may be approximated as constant throughout, Equation (C.6) may be used to transform this into an equation for fluctuating dipole moments:

$$\langle p_{j,\gamma}^{(\mathrm{fl})}(\omega) p_{j',\gamma'}^{(\mathrm{fl})*}(\omega')\rangle = 4\pi\hbar V_j\varepsilon_0 f^{(\mathrm{BE})}\left(\omega, T_j\right)\mathrm{Im}\left(\varepsilon_j\right)\delta_{jj'}\delta_{\gamma\gamma'}\delta(\omega-\omega') \qquad \text{(C.9)}$$

Equation (C.9) is identical to Equation (5.20), because $V_j\varepsilon_0\mathrm{Im}\left(\varepsilon_j\right) = \mathrm{Im}(\alpha_j^{(0)})$.

C.3 Reduced Absorption Factor

To transform the result for the net radiation heat transfer given by Equation (5.24) to the same form as that obtained in the many-body theory, a definition of the reduced absorption factor was used in terms of the dressed and bare polarizabilities in Equation (5.25) which is repeated here:

$$\chi_i = \frac{\left|\alpha_i^{(\mathrm{d})}\right|^2 \mathrm{Im}\left(\alpha_i^{(0)}\right)}{\left|\alpha_i^{(0)}\right|^2} \qquad \text{(C.10)}$$

Here it is proven that this definition is equivalent to that used in the many-body theory [115]:

$$\chi_i = \mathrm{Im}\left(\alpha_j^{(\mathrm{d})}\right) - \frac{k^3}{6\pi\varepsilon_m}\left|\alpha_j^{(\mathrm{d})}\right|^2 \tag{C.11}$$

Equation (C.11) can be written in terms of the dyadic Green's function $\mathbb{G}_{ii}^{(0)}$ as

$$\chi_i = \mathrm{Im}\left(\alpha_j^{(\mathrm{d})} - \frac{k^2}{\varepsilon_m}\mathbb{G}_{ii}^{(0)}\left|\alpha_j^{(\mathrm{d})}\right|^2\right) \tag{C.12}$$

Using the definition of the dressed polarizability from Equation (5.5), this becomes

$$\chi_i = \mathrm{Im}\left[\alpha_j^{(\mathrm{d})} + \left(\frac{1}{\alpha_j^{(\mathrm{d})}} - \frac{1}{\alpha_j^{(0)}}\right)\left|\alpha_j^{(\mathrm{d})}\right|^2\right] \tag{C.13}$$

With some algebraic manipulation and use of the identities $zz^* = |z|^2$ and $\mathrm{Im}(z^*) = -\mathrm{Im}(z)$, Equation (C.13) can be shown to be identical to Equation (C.10).

REFERENCES

[1] D. Polder and M. Van Hove, "Theory of radiative heat transfer between closely spaced bodies," *Phys. Rev. B,* vol. 4, no. 10, pp. 3303-3314, 1971, doi: 10.1103/PhysRevB.4.3303.

[2] L. Hu, A. Narayanaswamy, X. Y. Chen, and G. Chen, "Near-field thermal radiation between two closely spaced glass plates exceeding Planck's blackbody radiation law," *Appl. Phys. Lett.,* vol. 92, no. 13, p. 133106, 2008, doi: 10.1063/1.2905286.

[3] M. Francoeur, "Near-Field Thermal Radiation," in *Handbook of Thermal Science and Engineering*, F. A. Kulacki Ed. Cham: Springer, 2017.

[4] J. C. Cuevas and F. J. García-Vidal, "Radiative heat transfer," *ACS Photonics,* vol. 5, no. 10, pp. 3896-3915, 2018, doi: 10.1021/acsphotonics.8b01031.

[5] E. J. Tervo, E. Bagherisereshki, and Z. M. Zhang, "Near-field radiative thermoelectric energy converters: a review," *Frontiers in Energy,* vol. 12, no. 1, pp. 5-21, 2018, doi: 10.1007/s11708-017-0517-z.

[6] C. Dhand *et al.,* "Methods and strategies for the synthesis of diverse nanoparticles and their applications: a comprehensive overview," *RSC Adv.,* vol. 5, no. 127, pp. 105003-105037, 2015, doi: 10.1039/C5RA19388E.

[7] Y. Xia *et al.,* "One-dimensional Nanostructures: Synthesis, characterization, and applications," *Adv. Mater.,* vol. 15, no. 5, pp. 353-389, 2003, doi: 10.1002/adma.200390087.

[8] Z. M. Zhang, *Nano/Microscale Heat Transfer*. McGraw-Hill New York, 2007.

[9] R. Prasher, "Ultralow thermal conductivity of a packed bed of crystalline nanoparticles: A theoretical study," *Phys. Rev. B,* vol. 74, no. 16, p. 165413, 2006, doi: 10.1103/PhysRevB.74.165413.

[10] A. Ott, R. Messina, P. Ben-Abdallah, and S.-A. Biehs, "Magnetothermoplasmonics: from theory to applications," *J. Photonics Energy,* vol. 9, no. 3, pp. 1-19, 2019, doi: 10.1117/1.JPE.9.032711.

[11] M. Ferrera, N. Kinsey, A. Shaltout, C. DeVault, V. Shalaev, and A. Boltasseva, "Dynamic nanophotonics [invited]," *Journal of the Optical Society of America B,* vol. 34, no. 1, pp. 95-103, 2017, doi: 10.1364/JOSAB.34.000095.

[12] Y. Yang, S. Basu, and L. Wang, "Radiation-based near-field thermal rectification with phase transition materials," *Appl. Phys. Lett.,* vol. 103, no. 16, p. 163101, 2013, doi: 10.1063/1.4825168.

[13] M. Planck, *The Theory of Heat Radiation*. New York: Dover, 1991.

[14] J. B. Pendry, "Radiative exchange of heat between nanostructures," *J. Phys.: Condens. Matter,* vol. 11, no. 35, pp. 6621-6633, 1999, doi: Doi 10.1088/0953-8984/11/35/301.

[15] K. Joulain, J.-P. Mulet, F. Marquier, R. Carminati, and J.-J. Greffet, "Surface electromagnetic waves thermally excited: Radiative heat transfer, coherence properties and Casimir forces revisited in the near field," *Surf. Sci. Rep.,* vol. 57, no. 3-4, pp. 59-112, 2005, doi: 10.1016/j.surfrep.2004.12.002.

[16] M. Francoeur and M. Pinar Mengüç, "Role of fluctuational electrodynamics in near-field radiative heat transfer," *J. Quant. Spectrosc. Radiat. Transfer,* vol. 109, no. 2, pp. 280-293, 2008, doi: 10.1016/j.jqsrt.2007.08.017.

[17] S. Basu, Z. M. Zhang, and C. J. Fu, "Review of near-field thermal radiation and its application to energy conversion," *Int. J. Energy Res.,* vol. 33, no. 13, pp. 1203-1232, 2009, doi: 10.1002/er.1607.

[18] S.-A. Biehs, P. Ben-Abdallah, and F. Rosa, "Nanoscale radiative heat transfer and its applications," in *Infrared Radiation*, V. Morozhenko Ed.: InTech, 2012, pp. 1-26.

[19] M. T. H. Reid, A. W. Rodriguez, and S. G. Johnson, "Fluctuation-induced phenomena in nanoscale systems: harnessing the power of noise," *Proc. IEEE,* vol. 101, no. 2, pp. 531-545, 2013, doi: 10.1109/JPROC.2012.2191749.

[20] B. Song, A. Fiorino, E. Meyhofer, and P. Reddy, "Near-field radiative thermal transport: From theory to experiment," *AIP Adv.,* vol. 5, no. 5, p. 053503, 2015, doi: 10.1063/1.4919048.

[21] X. Liu, L. Wang, and Z. M. Zhang, "Near-field thermal radiation: recent progress and outlook," *Nanoscale Microscale Thermophys. Eng.,* vol. 19, no. 2, pp. 98-126, 2015, doi: 10.1080/15567265.2015.1027836.

[22] J. D. Caldwell *et al.,* "Low-loss, infrared and terahertz nanophotonics using surface phonon polaritons," *Nanophotonics,* vol. 4, no. 1, pp. 44-68, 2015, doi: 10.1515/nanoph-2014-0003.

[23] A. Zangwill, *Modern Electrodynamics*. Cambridge: Cambridge University Press, 2013.

[24] S. M. Rytov, Y. A. Kravtsov, and V. I. Tatarskii, *Principles of Statistical Radiophysics 3: Elements of Random Fields*. Springer-Verlag Berlin Heidelberg, 1989.

[25] D. J. Griffiths, *Introduction to Electrodynamics*, Fourth ed. Boston: Pearson, 2013.

[26] P. Ben-Abdallah, K. Joulain, J. Drevillon, and G. Domingues, "Near-field heat transfer mediated by surface wave hybridization between two films," *J. Appl. Phys.*, vol. 106, no. 4, p. 044306, 2009, doi: 10.1063/1.3204481.

[27] A. Narayanaswamy and G. Chen, "Direct computation of thermal emission from nanostructures," *Annual review of heat transfer*, vol. 14, no. 14, 2005, doi: 10.1103/PhysRevB.77.075125.

[28] M. Francoeur, M. Pinar Mengüç, and R. Vaillon, "Solution of near-field thermal radiation in one-dimensional layered media using dyadic Green's functions and the scattering matrix method," *J. Quant. Spectrosc. Radiat. Transfer*, vol. 110, no. 18, pp. 2002-2018, 2009, doi: https://doi.org/10.1016/j.jqsrt.2009.05.010.

[29] Z. H. Zheng and Y. M. Xuan, "Theory of near-field radiative heat transfer for stratified magnetic media," *Int. J. Heat Mass Transfer*, vol. 54, no. 5-6, pp. 1101-1110, 2011, doi: 10.1016/j.ijheatmasstransfer.2010.11.012.

[30] C. Otey and S. Fan, "Numerically exact calculation of electromagnetic heat transfer between a dielectric sphere and plate," *Phys. Rev. B*, vol. 84, no. 24, p. 245431, 2011, doi: 10.1103/PhysRevB.84.245431.

[31] A. Narayanaswamy and G. Chen, "Thermal near-field radiative transfer between two spheres," *Phys. Rev. B*, vol. 77, no. 7, p. 075125, 2008, doi: 10.1103/PhysRevB.77.075125.

[32] V. A. Golyk, M. Krüger, and M. Kardar, "Heat radiation from long cylindrical objects," *Phys. Rev. E*, vol. 85, no. 4, p. 046603, 2012, doi: 10.1103/PhysRevE.85.046603.

[33] B. Czapla and A. Narayanaswamy, "Thermal radiative energy exchange between a closely-spaced linear chain of spheres and its environment," *J. Quant. Spectrosc. Radiat. Transfer*, vol. 227, pp. 4-11, 2019, doi: 10.1016/j.jqsrt.2019.01.020.

[34] S. A. Biehs, P. Ben-Abdallah, F. S. S. Rosa, K. Joulain, and J. J. Greffet, "Nanoscale heat flux between nanoporous materials," *Opt. Express*, vol. 19, no. S5, pp. A1088-A1103, 2011, doi: 10.1364/OE.19.0A1088.

[35] S.-A. Biehs, O. Huth, and F. Rüting, "Near-field radiative heat transfer for structured surfaces," *Phys. Rev. B*, vol. 78, no. 8, p. 085414, 2008, doi: 10.1103/PhysRevB.78.085414.

[36] G. Bimonte, "Scattering approach to Casimir forces and radiative heat transfer for nanostructured surfaces out of thermal equilibrium," *Phys. Rev. A*, vol. 80, no. 4, p. 042102, 2009, doi: 10.1103/PhysRevA.80.042102.

[37] R. Messina and M. Antezza, "Scattering-matrix approach to Casimir-Lifshitz force and heat transfer out of thermal equilibrium between arbitrary bodies," *Phys. Rev. A*, vol. 84, no. 4, p. 042102, 2011, doi: 10.1103/PhysRevA.84.042102.

[38] M. Krüger, T. Emig, and M. Kardar, "Nonequilibrium electromagnetic fluctuations: Heat transfer and interactions," *Phys. Rev. Lett.*, vol. 106, no. 21, p. 210404, 2011, doi: 10.1103/PhysRevLett.106.210404.

[39] M. Krüger, G. Bimonte, T. Emig, and M. Kardar, "Trace formulas for nonequilibrium Casimir interactions, heat radiation, and heat transfer for arbitrary objects," *Phys. Rev. B*, vol. 86, no. 11, p. 115423, 2012, doi: 10.1103/PhysRevB.86.115423.

[40] C. R. Otey, L. X. Zhu, S. Sandhu, and S. H. Fan, "Fluctuational electrodynamics calculations of near-field heat transfer in non-planar geometries: A brief overview," *Journal of Quantitative Spectroscopy & Radiative Transfer*, vol. 132, pp. 3-11, 2014, doi: 10.1016/j.jqsrt.2013.04.017.

[41] A. W. Rodriguez, M. T. H. Reid, and S. G. Johnson, "Fluctuating-surface-current formulation of radiative heat transfer for arbitrary geometries," *Phys. Rev. B*, vol. 86, no. 22, p. 220302, 2012, doi: 10.1103/PhysRevB.86.220302.

[42] A. W. Rodriguez, M. T. H. Reid, and S. G. Johnson, "Fluctuating-surface-current formulation of radiative heat transfer: Theory and applications," *Phys. Rev. B*, vol. 88, no. 5, p. 054305, 2013, doi: 10.1103/PhysRevB.88.054305.

[43] A. G. Polimeridis, M. T. H. Reid, W. Jin, S. G. Johnson, J. K. White, and A. W. Rodriguez, "Fluctuating volume-current formulation of electromagnetic fluctuations in inhomogeneous media: Incandescence and luminescence in arbitrary geometries," *Phys. Rev. B*, vol. 92, no. 13, p. 134202, 2015, doi: 10.1103/PhysRevB.92.134202.

[44] C. Luo, A. Narayanaswamy, G. Chen, and J. D. Joannopoulos, "Thermal radiation from photonic crystals: A direct calculation," *Phys. Rev. Lett.*, vol. 93, no. 21, p. 213905, 2004, doi: 10.1103/PhysRevLett.93.213905.

[45] A. W. Rodriguez *et al.*, "Frequency-selective near-field radiative heat transfer between photonic crystal slabs: A computational approach for arbitrary geometries and materials," *Phys. Rev. Lett.*, vol. 107, no. 11, p. 114302, 2011, doi: 10.1103/PhysRevLett.107.114302.

[46] A. Datas, D. Hirashima, and K. Hanamura, "FDTD simulation of near-field radiative heat transfer between thin films supporting surface phonon polaritons: Lessons learned," *J. Therm. Sci. Technol.*, vol. 8, no. 1, pp. 91-105, 2013, doi: 10.1299/jtst.8.91.

[47] A. Didari and M. P. Menguc, "Analysis of near-field radiation transfer within nano-gaps using FDTD method," *Journal of Quantitative Spectroscopy & Radiative Transfer*, vol. 146, pp. 214-226, 2014, doi: 10.1016/j.jqsrt.2014.04.002.

[48] S.-B. Wen, "Direct numerical simulation of near field thermal radiation based on wiener chaos expansion of thermal fluctuating current," *J. Heat Transfer,* vol. 132, no. 7, pp. 072704-072704-7, 2010, doi: 10.1115/1.4000995.

[49] B. Liu and S. Shen, "Broadband near-field radiative thermal emitter/absorber based on hyperbolic metamaterials: Direct numerical simulation by the Wiener chaos expansion method," *Phys. Rev. B,* vol. 87, no. 11, p. 115403, 2013, doi: 10.1103/PhysRevB.87.115403.

[50] S. Edalatpour and M. Francoeur, "The Thermal Discrete Dipole Approximation (T-DDA) for near-field radiative heat transfer simulations in three-dimensional arbitrary geometries," *J. Quant. Spectrosc. Radiat. Transfer,* vol. 133, pp. 364-373, 2014, doi: 10.1016/j.jqsrt.2013.08.021.

[51] S. Edalatpour, M. Cuma, T. Trueax, R. Backman, and M. Francoeur, "Convergence analysis of the thermal discrete dipole approximation," *Phys. Rev. E,* vol. 91, no. 6, p. 063307, 2015, doi: 10.1103/PhysRevE.91.063307.

[52] S. Edalatpour and M. Francoeur, "Near-field radiative heat transfer between arbitrarily shaped objects and a surface," *Phys. Rev. B,* vol. 94, no. 4, p. 045406, 2016, doi: 10.1103/PhysRevB.94.045406.

[53] R. M. A. Ekeroth, A. Garcia-Martin, and J. C. Cuevas, "Thermal discrete dipole approximation for the description of thermal emission and radiative heat transfer of magneto-optical systems," *Phys. Rev. B,* vol. 95, no. 23, p. 235428, 2017, doi: 10.1103/PhysRevB.95.235428.

[54] A. Narayanaswamy, S. Shen, and G. Chen, "Near-field radiative heat transfer between a sphere and a substrate," *Phys. Rev. B,* vol. 78, no. 11, 2008, doi: 10.1103/PhysRevB.78.115303.

[55] E. Rousseau *et al.,* "Radiative heat transfer at the nanoscale," *Nat. Photonics,* vol. 3, no. 9, pp. 514-517, 2009, doi: 10.1038/Nphoton.2009.144.

[56] S. Shen, A. Narayanaswamy, and G. Chen, "Surface phonon polaritons mediated energy transfer between nanoscale gaps," *Nano Lett,* vol. 9, no. 8, pp. 2909-13, 2009, doi: 10.1021/nl901208v.

[57] S. Shen, A. Mavrokefalos, P. Sambegoro, and G. Chen, "Nanoscale thermal radiation between two gold surfaces," *Appl. Phys. Lett.,* vol. 100, no. 23, 2012, doi: 10.1063/1.4723713.

[58] P. Van Zwol, L. Ranno, and J. Chevrier, "Tuning near field radiative heat flux through surface excitations with a metal insulator transition," *Phys. Rev. Lett.,* vol. 108, no. 23, p. 234301, 2012, doi: 10.1103/PhysRevLett.108.234301.

[59] P. J. van Zwol, S. Thiele, C. Berger, W. A. de Heer, and J. Chevrier, "Nanoscale radiative heat flow due to surface plasmons in graphene and doped silicon," *Phys.*

Rev. Lett., vol. 109, no. 26, p. 264301, 2012, doi: 10.1103/PhysRevLett.109.264301.

[60] J. W. Shi, P. F. Li, B. A. Liu, and S. Shen, "Tuning near field radiation by doped silicon," *Appl. Phys. Lett.*, vol. 102, no. 18, 2013, doi: 10.1063/1.4804631.

[61] R. St-Gelais, B. Guha, L. X. Zhu, S. H. Fan, and M. Lipson, "Demonstration of strong near-field radiative heat transfer between integrated nanostructures," *Nano Lett.*, vol. 14, no. 12, pp. 6971-6975, 2014, doi: 10.1021/nl503236k.

[62] B. Song *et al.*, "Enhancement of near-field radiative heat transfer using polar dielectric thin films," *Nat. Nanotechnol.*, vol. 10, no. 3, pp. 253-258, 2015, doi: 10.1038/Nnano.2015.6.

[63] J. W. Shi, B. A. Liu, P. F. Li, L. Y. Ng, and S. Shen, "Near-field energy extraction with hyperbolic metamaterials," *Nano Lett.*, vol. 15, no. 2, pp. 1217-1221, 2015, doi: 10.1021/nl504332t.

[64] K. Kim *et al.*, "Radiative heat transfer in the extreme near field," *Nature*, vol. 528, no. 7582, p. 387, 2015, doi: 10.1038/nature16070.

[65] R. St-Gelais, L. Zhu, S. Fan, and M. Lipson, "Near-field radiative heat transfer between parallel structures in the deep subwavelength regime," *Nat. Nanotechnol.*, vol. 11, no. 6, pp. 515-519, 2016, doi: 10.1038/nnano.2016.20.

[66] B. Song, D. Thompson, A. Fiorino, Y. Ganjeh, P. Reddy, and E. Meyhofer, "Radiative heat conductances between dielectric and metallic parallel plates with nanoscale gaps," *Nat. Nanotechnol.*, vol. 11, no. 6, p. 509, 2016, doi: 10.1038/Nnano.2016.17.

[67] A. Fiorino, D. Thompson, L. X. Zhu, B. Song, P. Reddy, and E. Meyhofer, "Giant enhancement in radiative heat transfer in sub-30 nm gaps of plane parallel surfaces," *Nano Lett.*, vol. 18, no. 6, pp. 3711-3715, 2018, doi: 10.1021/acs.nanolett.8b00846.

[68] R. S. Ottens *et al.*, "Near-field radiative heat transfer between macroscopic planar surfaces," *Phys. Rev. Lett.*, vol. 107, no. 1, 2011, doi: 10.1103/PhysRevLett.107.014301.

[69] T. Ijiro and N. Yamada, "Near-field radiative heat transfer between two parallel SiO2 plates with and without microcavities," *Appl. Phys. Lett.*, vol. 106, no. 2, p. 023103, 2015.

[70] K. Ito, A. Miura, H. Iizuka, and H. Toshiyoshi, "Parallel-plate submicron gap formed by micromachined low-density pillars for near-field radiative heat transfer," *Appl. Phys. Lett.*, vol. 106, no. 8, 2015, doi: 10.1063/1.4913692.

[71] M. Lim, S. S. Lee, and B. J. Lee, "Near-field thermal radiation between doped silicon plates at nanoscale gaps," *Phys. Rev. B,* vol. 91, no. 19, 2015, doi: 10.1103/PhysRevB.91.195136.

[72] M. P. Bernardi, D. Milovich, and M. Francoeur, "Radiative heat transfer exceeding the blackbody limit between macroscale planar surfaces separated by a nanosize vacuum gap," *Nat. Commun.,* vol. 7, 2016, doi: 10.1038/ncomms12900.

[73] J. I. Watjen, B. Zhao, and Z. M. Zhang, "Near-field radiative heat transfer between doped-Si parallel plates separated by a spacing down to 200 nm," *Appl. Phys. Lett.,* vol. 109, no. 20, p. 203112, 2016, doi: 10.1063/1.4967384.

[74] M. Ghashami, H. Y. Geng, T. Kim, N. Iacopino, S. K. Cho, and K. Park, "Precision measurement of phonon-polaritonic near-field energy transfer between macroscale planar structures under large thermal gradients," *Phys. Rev. Lett.,* vol. 120, no. 17, 2018, doi: 10.1103/PhysRevLett.120.175901.

[75] A. Fiorino, L. X. Zhu, D. Thompson, R. Mittapally, P. Reddy, and E. Meyhofer, "Nanogap near-field thermophotovoltaics," *Nat. Nanotechnol.,* vol. 13, no. 9, p. 806, 2018, doi: 10.1038/s41565-018-0172-5.

[76] T. Inoue, T. Koyama, D. D. Kang, K. Ikeda, T. Asano, and S. Noda, "One-chip near-field thermophotovoltaic device integrating a thin-film thermal emitter and photovoltaic cell," *Nano Lett.,* vol. 19, no. 6, pp. 3948-3952, 2019, doi: 10.1021/acs.nanolett.9b01234.

[77] L. Zhu, A. Fiorino, D. Thompson, R. Mittapally, E. Meyhofer, and P. Reddy, "Near-field photonic cooling through control of the chemical potential of photons," *Nature,* vol. 566, no. 7743, pp. 239-244, 2019, doi: 10.1038/s41586-019-0918-8.

[78] C. F. Bohren and D. R. Huffman, *Absorption and Scattering of Light by Small Particles*. Weinheim: WILEY-VCH, 2004.

[79] M. I. Mishchenko, *Electromagnetic Scattering by Particles and Particle Groups: An Introduction*. New York: Cambridge University Press, 2014.

[80] M. Quinten, A. Leitner, J. R. Krenn, and F. R. Aussenegg, "Electromagnetic energy transport via linear chains of silver nanoparticles," *Opt. Lett.,* vol. 23, no. 17, pp. 1331-3, 1998, doi: 10.1364/OL.23.001331.

[81] M. L. Brongersma, J. W. Hartman, and H. A. Atwater, "Electromagnetic energy transfer and switching in nanoparticle chain arrays below the diffraction limit," *Phys. Rev. B,* vol. 62, no. 24, pp. 16356-16359, 2000, doi: 10.1103/PhysRevB.62.R16356.

[82] S. A. Maier *et al.,* "Local detection of electromagnetic energy transport below the diffraction limit in metal nanoparticle plasmon waveguides," *Nat. Mater.,* vol. 2, no. 4, pp. 229-232, 2003, doi: 10.1038/nmat852.

[83] S. Y. Park and D. Stroud, "Surface-plasmon dispersion relations in chains of metallic nanoparticles: An exact quasistatic calculation," *Phys. Rev. B,* vol. 69, no. 12, p. 125418, 2004, doi: 10.1103/Physrevb.69.125418.

[84] W. H. Weber and G. W. Ford, "Propagation of optical excitations by dipolar interactions in metal nanoparticle chains," *Phys. Rev. B,* vol. 70, no. 12, p. 125429, 2004, doi: 10.1103/Physrevb.70.125429.

[85] A. F. Koenderink and A. Polman, "Complex response and polariton-like dispersion splitting in periodic metal nanoparticle chains," *Phys. Rev. B,* vol. 74, no. 3, p. 033402, 2006, doi: 10.1103/Physrevb.74.033402.

[86] D. S. Citrin, "Plasmon-polariton transport in metal-nanoparticle chains embedded in a gain medium," *Opt. Lett.,* vol. 31, no. 1, pp. 98-100, 2006, doi: 10.1364/OL.31.000098.

[87] N. J. Halas, S. Lal, W.-S. Chang, S. Link, and P. Nordlander, "Plasmons in strongly coupled metallic nanostructures," *Chem. Rev.,* vol. 111, no. 6, pp. 3932-3934, 2011, doi: 10.1021/cr200061k.

[88] C. A. Downing, E. Mariani, and G. Weick, "Retardation effects on the dispersion and propagation of plasmons in metallic nanoparticle chains," *J. Phys.: Condens. Matter,* vol. 30, no. 2, p. 025301, 2017, doi: 10.1088/1361-648x/aa9d59.

[89] E. J. Tervo, D. S. Boyuk, B. A. Cola, Z. M. M. Zhang, and M. A. Filler, "Sub-diffractional waveguiding by mid-infrared plasmonic resonators in semiconductor nanowires," *Nanoscale,* vol. 10, no. 12, pp. 5708-5716, 2018, doi: 10.1039/c8nr00701b.

[90] W. L. Barnes, A. Dereux, and T. W. Ebbesen, "Surface plasmon subwavelength optics," *Nature,* vol. 424, no. 6950, pp. 824-830, 2003, doi: 10.1038/nature01937.

[91] S. Lal, S. Link, and N. J. Halas, "Nano-optics from sensing to waveguiding," *Nat. Photonics,* vol. 1, no. 11, pp. 641-648, 2007, doi: 10.1038/nphoton.2007.223.

[92] P. Ben-Abdallah, K. Joulain, J. Drevillon, and C. Le Goff, "Heat transport through plasmonic interactions in closely spaced metallic nanoparticle chains," *Phys. Rev. B,* vol. 77, no. 7, p. 075417, 2008, doi: 10.1103/PhysRevB.77.075417.

[93] E. M. Purcell and C. R. Pennypacker, "Scattering and cbsorption of light by nonspherical dielectric grains," *Astrophys. J.,* vol. 186, pp. 705-714, 1973, doi: 10.1086/152538.

[94] M. A. Yurkin and A. G. Hoekstra, "The discrete dipole approximation: An overview and recent developments," *Journal of Quantitative Spectroscopy & Radiative Transfer,* vol. 106, no. 1-3, pp. 558-589, 2007, doi: 10.1016/j.jqsrt.2007.01.034.

[95] B. T. Draine, "The discrete-dipole approximation and its application to interstellar graphite grains," *Astrophys. J.*, vol. 333, p. 848, 1988, doi: 10.1086/166795.

[96] B. T. Draine and J. Goodman, "Beyond Clausius-Mossotti: Wave propagation on a polarizable point lattice and the discrete dipole approximation," *Astrophys. J.*, vol. 405, p. 685, 1993, doi: 10.1086/172396.

[97] B. T. Draine and P. J. Flatau, "Discrete-dipole approximation for scattering calculations," *Journal of the Optical Society of America A*, vol. 11, no. 4, pp. 1491-1499, 1994, doi: 10.1364/Josaa.11.001491.

[98] B. T. Draine, "The discrete dipole approximation for light scattering by irregular targets," in *Light Scattering by Nonspherical Particles: Theory, Measurements, and Applications*, M. I. Mishchenko, J. W. Hovenier, and L. D. Travis Eds. San Diego: Academic Press, 2000, p. 131.

[99] B. T. Draine and P. J. Flatau, "User Guide for the Discrete Dipole Approximation Code DDSCAT 6.1," *arXiv:astro-ph/0409262v2*, 2006.

[100] G. H. Goedecke and S. G. Obrien, "Scattering by irregular inhomogeneous particles via the digitized Greens-function algorithm," *Appl. Opt.*, vol. 27, no. 12, pp. 2431-2438, 1988, doi: Doi 10.1364/Ao.27.002431.

[101] A. Lakhtakia, "Strong and weak forms of the method of moments and the coupled dipole method for scattering of time-harmonic electromagnetic fields," *International Journal of Modern Physics C*, vol. 03, no. 03, pp. 583-603, 1992, doi: 10.1142/S0129183192000385.

[102] J. Rahola, "Solution of dense systems of linear equations in the discrete-dipole approximation," *SIAM Journal on Scientific Computing*, vol. 17, no. 1, pp. 78-89, 1996, doi: 10.1137/0917007.

[103] N. B. Piller, "Coupled-dipole approximation for high permittivity materials," *Opt. Commun.*, vol. 160, no. 1, pp. 10-14, 1999, doi: https://doi.org/10.1016/S0030-4018(98)00645-2.

[104] F. M. Kahnert, "Numerical methods in electromagnetic scattering theory," *J. Quant. Spectrosc. Radiat. Transfer*, vol. 79-80, pp. 775-824, 2003, doi: 10.1016/S0022-4073(02)00321-7.

[105] S. B. Singham and C. F. Bohren, "Light scattering by an arbitrary particle: a physical reformulation of the coupled dipole method," *Opt. Lett.*, vol. 12, no. 1, pp. 10-12, 1987, doi: 10.1364/OL.12.000010.

[106] O. S. Kim, P. Meincke, O. Breinbjerg, and E. JøRgensen, "Method of moments solution of volume integral equations using higher-order hierarchical Legendre basis functions," *Radio Sci.*, vol. 39, no. 5, p. RS5003, 2004, doi: 10.1029/2004RS003041.

[107] A. Lakhtakia and G. W. Mulholland, "On two numerical techniques for light scattering by dielectric agglomerated structures," *J. Res. Nat. Inst. Stand. Technol.*, vol. 98, no. 6, pp. 699-716, 1993, doi: 10.6028/jres.098.046.

[108] P. Ben-Abdallah, "Heat transfer through near-field interactions in nanofluids," *Appl. Phys. Lett.*, vol. 89, no. 11, p. 113117, 2006, doi: 10.1063/1.2349857.

[109] J. Ordonez-Miranda, L. Tranchant, S. Gluchko, and S. Volz, "Energy transport of surface phonon polaritons propagating along a chain of spheroidal nanoparticles," *Phys. Rev. B*, vol. 92, no. 11, p. 115409, 2015, doi: 10.1103/PhysRevB.92.115409.

[110] J. Ordonez-Miranda, L. Tranchant, K. Joulain, Y. Ezzahri, J. Drevillon, and S. Volz, "Thermal energy transport in a surface phonon-polariton crystal," *Phys. Rev. B*, vol. 93, no. 3, p. 35428, 2016, doi: 10.1103/PhysRevB.93.035428.

[111] J. Ordonez-Miranda, K. Joulain, and Y. Ezzahri, "Thermal conductance of a surface phonon-polariton crystal made up of polar nanorods," *Z. Naturforsch. A*, vol. 72, no. 2, pp. 135-139, 2017, doi: 10.1515/zna-2016-0454.

[112] F. V. Ramirez and A. J. H. McGaughey, "Plasmonic thermal transport in graphene nanodisk waveguides," *Phys. Rev. B*, vol. 96, no. 16, p. 165428, 2017, doi: 10.1103/PhysRevB.96.165428.

[113] E. J. Tervo, M. E. Gustafson, Z. M. Zhang, B. A. Cola, and M. A. Filler, "Photonic thermal conduction by infrared plasmonic resonators in semiconductor nanowires," *Appl. Phys. Lett.*, vol. 114, no. 16, p. 163104, 2019, doi: 10.1063/1.5093309.

[114] P. Ben-Abdallah, S.-A. Biehs, and K. Joulain, "Many-body radiative heat transfer theory," *Phys. Rev. Lett.*, vol. 107, no. 11, p. 114301, 2011, doi: 10.1103/PhysRevLett.107.114301.

[115] R. Messina, M. Tschikin, S. A. Biehs, and P. Ben-Abdallah, "Fluctuation-electrodynamic theory and dynamics of heat transfer in systems of multiple dipoles," *Phys. Rev. B*, vol. 88, no. 10, p. 104307, 2013, doi: 10.1103/PhysRevB.88.104307.

[116] K. Sääskilahti, J. Oksanen, and J. Tulkki, "Quantum Langevin equation approach to electromagnetic energy transfer between dielectric bodies in an inhomogeneous environment," *Phys. Rev. B*, vol. 89, no. 13, p. 134301, 2014, doi: 10.1103/PhysRevB.89.134301.

[117] M. Nikbakht, "Radiative heat transfer in anisotropic many-body systems: Tuning and enhancement," *J. Appl. Phys.*, vol. 116, no. 9, p. 094307, 2014, doi: 10.1063/1.4894622.

[118] M. Nikbakht, "Radiative heat transfer in fractal structures," *Phys. Rev. B*, vol. 96, no. 12, p. 125436, 2017, doi: 10.1103/PhysRevB.96.125436.

[119] J. Dong, J. Zhao, and L. Liu, "Radiative heat transfer in many-body systems: Coupled electric and magnetic dipole approach," *Phys. Rev. B,* vol. 95, no. 12, p. 125411, 2017, doi: 10.1103/PhysRevB.95.125411.

[120] L. Zhu, Y. Guo, and S. Fan, "Theory of many-body radiative heat transfer without the constraint of reciprocity," *Phys. Rev. B,* vol. 97, no. 9, p. 094302, 2018, doi: 10.1103/PhysRevB.97.094302.

[121] J. Chen, C. Y. Zhao, and B. X. Wang, "Near-field thermal radiative transfer in assembled spherical systems composed of core-shell nanoparticles," *J. Quant. Spectrosc. Radiat. Transfer,* vol. 219, pp. 304-312, 2018, doi: 10.1016/j.jqsrt.2018.08.024.

[122] D. Becerril and C. Noguez, "Near-field energy transfer between nanoparticles modulated by coupled multipolar modes," *Phys. Rev. B,* vol. 99, no. 4, p. 045418, 2019, doi: 10.1103/PhysRevB.99.045418.

[123] J. B. Khurgin and A. Boltasseva, "Reflecting upon the losses in plasmonics and metamaterials," *MRS Bull.,* vol. 37, no. 8, pp. 768-779, 2012, doi: 10.1557/mrs.2012.173.

[124] C. Kathmann, R. Messina, P. Ben-Abdallah, and S. A. Biehs, "Limitations of kinetic theory to describe near-field heat exchanges in many-body systems," *Phys. Rev. B,* vol. 98, no. 11, 2018, doi: 10.1103/PhysRevB.98.115434.

[125] S. A. Maier, P. G. Kik, and H. A. Atwater, "Optical pulse propagation in metal nanoparticle chain waveguides," *Phys. Rev. B,* vol. 67, no. 20, p. 205402, 2003, doi: 10.1103/PhysRevB.67.205402.

[126] P. Ben-Abdallah, R. Messina, S.-A. Biehs, M. Tschikin, K. Joulain, and C. Henkel, "Heat superdiffusion in plasmonic nanostructure networks," *Phys. Rev. Lett.,* vol. 111, no. 17, p. 174301, 2013, doi: 10.1103/PhysRevLett.111.174301.

[127] P. Ben-Abdallah, "Photon thermal hall effect," *Phys. Rev. Lett.,* vol. 116, no. 8, p. 084301, 2016, doi: 10.1103/PhysRevLett.116.084301.

[128] I. Latella and P. Ben-Abdallah, "Giant thermal magnetoresistance in plasmonic structures," *Phys. Rev. Lett.,* vol. 118, no. 17, p. 173902, 2017, doi: 10.1103/PhysRevLett.118.173902.

[129] L. Zhu and S. Fan, "Persistent directional current at equilibrium in nonreciprocal many-body near field electromagnetic heat transfer," *Phys. Rev. Lett.,* vol. 117, no. 13, p. 134303, 2016, doi: 10.1103/PhysRevLett.117.134303.

[130] S. Edalatpour, V. Hatamipour, and M. Francoeur, "Spectral redshift of the thermal near field scattered by a probe," *Phys. Rev. B,* vol. 99, no. 16, p. 165401, 2019, doi: 10.1103/PhysRevB.99.165401.

[131] M. A. Snyder, J. A. Lee, T. M. Davis, L. E. Scriven, and M. Tsapatsis, "Silica nanoparticle crystals and ordered coatings using lys-sil and a novel coating device," *Langmuir*, vol. 23, no. 20, pp. 9924-9928, 2007, doi: 10.1021/la701063v.

[132] E. J. Tervo, O. S. Adewuyi, J. S. Hammonds, and B. A. Cola, "High thermal conductivity in polaritonic SiO2 nanoparticle beds," *Mater. Horiz.*, vol. 3, no. 5, pp. 434-441, 2016, doi: 10.1039/c6mh00098c.

[133] A. Babuty, K. Joulain, P.-O. Chapuis, J.-J. Greffet, and Y. De Wilde, "Blackbody spectrum revisited in the near field," *Phys. Rev. Lett.*, vol. 110, no. 14, p. 146103, 2013, doi: 10.1103/PhysRevLett.110.146103.

[134] R. M. Almeida, "Detection of LO modes in glass by infrared reflection spectroscopy at oblique incidence," *Phys. Rev. B*, vol. 45, no. 1, pp. 161-170, 1992, doi: 10.1103/PhysRevB.45.161.

[135] G. Borstel, H. J. Falge, and A. Otto, "Surface and bulk phonon-polaritons observed by attenuated total reflection," in *Solid-State Physics*, vol. 74, (Springer Tracts in Modern Physics: Springer Berlin Heidelberg, 1974, ch. 2, pp. 107-148.

[136] W.-T. Liu and Y. R. Shen, "Sum-frequency phonon spectroscopy on alpha-quartz," *Phys. Rev. B*, vol. 78, no. 2, p. 024302, 2008, doi: 10.1002/andp.201000093.

[137] W.-T. Liu and Y. R. Shen, "Surface vibrational modes of alpha-quartz(0001) probed by sum-frequency spectroscopy," *Phys. Rev. Lett.*, vol. 101, no. 1, p. 016101, 2008, doi: 10.1103/PhysRevLett.101.016101.

[138] M. L. Hair and W. Hertl, "Adsorption on hydroxylated silica surfaces," *The Journal of Physical Chemistry*, vol. 73, no. 12, pp. 4269-4276, 1969, doi: 10.1021/j100846a039.

[139] H. Fröhlich, *Theory of Dielectrics*. Clarendon Press, 1949.

[140] X. J. Hu, R. Prasher, and K. Lofgreen, "Ultralow thermal conductivity of nanoparticle packed bed," *Appl. Phys. Lett.*, vol. 91, no. 20, p. 203113, 2007, doi: Doi 10.1063/1.2814959.

[141] T. F. Sun and A. S. Teja, "Density, viscosity, and thermal conductivity of aqueous ethylene, diethylene, and triethylene glycol mixtures between 290 K and 450 K," *J. Chem. Eng. Data*, vol. 48, no. 1, pp. 198-202, 2003, doi: 10.1021/je025610o.

[142] P. E. Hopkins, B. Kaehr, E. S. Piekos, D. Dunphy, and C. J. Brinker, "Minimum thermal conductivity considerations in aerogel thin films," *J. Appl. Phys.*, vol. 111, no. 11, p. 113532, 2012, doi: 10.1063/1.4729325.

[143] J.-P. Mulet, K. Joulain, R. Carminati, and J.-J. Greffet, "Nanoscale radiative heat transfer between a small particle and a plane surface," *Appl. Phys. Lett.*, vol. 78, no. 19, pp. 2931-2933, 2001, doi: doi:http://dx.doi.org/10.1063/1.1370118.

[144] E. D. Palik, *Handbook of Optical Constants of Solids*. Orlando: Academic Press, 1985.

[145] B. Cola, "(Invited) Thermal Energy Conduction in a Surface Phonon Polariton Crystal," *ECS Meeting Abstracts,* vol. 28, p. 1068, 2015.

[146] J.-J. Greffet, R. Carminati, K. Joulain, J.-P. Mulet, S. Mainguy, and Y. Chen, "Coherent emission of light by thermal sources," *Nature,* vol. 416, no. 6876, pp. 61-64, 2002, doi: 10.1038/416061a.

[147] T. Fisher, *Thermal Energy at the Nanoscale* (Lessons from Nanoscience). World Scientific Publishing Co, 2014.

[148] W. C. Tait and R. L. Weiher, "Contributions of Scattering of Polaritons by Phonons to Emission of Radiation by Solids," *Physical Review,* vol. 178, no. 3, pp. 1404-1410, 1969. [Online]. Available: http://link.aps.org/doi/10.1103/PhysRev.178.1404.

[149] A. D. Phan, T.-L. Phan, and L. M. Woods, "Near-field heat transfer between gold nanoparticle arrays," *J. Appl. Phys.,* vol. 114, no. 21, p. 214306, 2013, doi: 10.1063/1.4838875.

[150] S. Leroch and M. Wendland, "Influence of capillary bridge formation onto the silica nanoparticle interaction studied by grand canonical Monte Carlo simulations," *Langmuir : the ACS journal of surfaces and colloids,* vol. 29, no. 40, pp. 12410-12420, 2013, doi: 10.1021/la402002f.

[151] M. O. Elsahati and R. F. Richards, "Effect of moisture on nanoparticle packed beds," *Int. J. Heat Mass Transfer,* vol. 112, pp. 171-184, 2017, doi: 10.1016/j.ijheatmasstransfer.2017.04.073.

[152] F. Meng, M. Elsahati, J. Liu, and R. F. Richards, "Thermal resistance between amorphous silica nanoparticles," *J. Appl. Phys.,* vol. 121, no. 19, p. 194302, 2017, doi: 10.1063/1.4983753.

[153] F. Meng, J. Liu, and R. F. Richards, "Effect of water vapor on the thermal resistance between amorphous silica nanoparticles," *J. Appl. Phys.,* vol. 124, no. 5, p. 054303, 2018, doi: 10.1063/1.5038117.

[154] D. S. Boyuk, L.-W. Chou, and M. A. Filler, "Strong near-field coupling of plasmonic resonators embedded in Si nanowires," *ACS Photonics,* vol. 3, no. 2, pp. 184-189, 2016, doi: 10.1021/acsphotonics.5b00581.

[155] L.-W. Chou, D. S. Boyuk, and M. A. Filler, "Optically abrupt localized surface plasmon resonances in Si nanowires by mitigation of carrier density gradients," *ACS Nano,* vol. 9, no. 2, pp. 1250-1256, 2015, doi: 10.1021/nn504974z.

[156] S. Kim, D. J. Hill, C. W. Pinion, J. D. Christesen, J. R. McBride, and J. F. Cahoon, "Designing morphology in epitaxial silicon nanowires: The role of gold, surface chemistry, and phosphorus doping," *ACS Nano,* vol. 11, no. 5, pp. 4453-4462, 2017, doi: 10.1021/acsnano.7b00457.

[157] M. Heurlin *et al.*, "Continuous gas-phase synthesis of nanowires with tunable properties," *Nature,* vol. 492, p. 90, 2012, doi: 10.1038/nature11652.

[158] S. J. Allen, D. C. Tsui, and R. A. Logan, "Observation of the two-dimensional plasmon in silicon inversion layers," *Phys. Rev. Lett.,* vol. 38, no. 17, pp. 980-983, 1977, doi: 10.1103/PhysRevLett.38.980.

[159] L.-W. Chou, R. D. Near, D. S. Boyuk, and M. A. Filler, "Influence of Dielectric Anisotropy on the Absorption Properties of Localized Surface Plasmon Resonances Embedded in Si Nanowires," *The Journal of Physical Chemistry C,* vol. 118, no. 10, pp. 5494-5500, 2014, doi: 10.1021/jp501452q.

[160] J. Zuloaga and P. Nordlander, "On the energy shift between near-field and far-field peak intensities in localized plasmon systems," *Nano Lett.,* vol. 11, no. 3, pp. 1280-1283, 2011, doi: 10.1021/nl1043242.

[161] P. K. Jain, W. Huang, and M. A. El-Sayed, "On the universal scaling behavior of the distance decay of plasmon coupling in metal nanoparticle pairs: A plasmon ruler equation," *Nano Lett.,* vol. 7, no. 7, pp. 2080-2088, 2007, doi: 10.1021/nl071008a.

[162] S. Underwood and P. Mulvaney, "Effect of the solution refractive index on the color of gold colloids," *Langmuir,* vol. 10, no. 10, pp. 3427-3430, 1994, doi: 10.1021/la00022a011.

[163] T. R. Jensen, M. L. Duval, K. L. Kelly, A. A. Lazarides, G. C. Schatz, and R. P. Van Duyne, "Nanosphere lithography: Effect of the external dielectric medium on the surface plasmon resonance spectrum of a periodic array of silver nanoparticles," *The Journal of Physical Chemistry B,* vol. 103, no. 45, pp. 9846-9853, 1999, doi: 10.1021/jp9926802.

[164] E. Prodan, A. Lee, and P. Nordlander, "The effect of a dielectric core and embedding medium on the polarizability of metallic nanoshells," *Chem. Phys. Lett.,* vol. 360, no. 3, pp. 325-332, 2002, doi: http://dx.doi.org/10.1016/S0009-2614(02)00850-3.

[165] K.-S. Lee and M. A. El-Sayed, "Gold and silver nanoparticles in sensing and imaging: Sensitivity of plasmon response to size, shape, and metal composition," *The Journal of Physical Chemistry B,* vol. 110, no. 39, pp. 19220-19225, 2006, doi: 10.1021/jp062536y.

[166] P. K. Jain and M. A. El-Sayed, "Noble metal nanoparticle pairs: Effect of medium for enhanced nanosensing," *Nano Lett.,* vol. 8, no. 12, pp. 4347-4352, 2008, doi: 10.1021/nl8021835.

[167] C. Sonnichsen, B. M. Reinhard, J. Liphardt, and A. P. Alivisatos, "A molecular ruler based on plasmon coupling of single gold and silver nanoparticles," *Nat. Biotechnol.,* vol. 23, no. 6, pp. 741-745, 2005, doi: 10.1038/nbt1100.

[168] A. M. Funston, C. Novo, T. J. Davis, and P. Mulvaney, "Plasmon coupling of gold nanorods at short distances and in different geometries," *Nano Lett.*, vol. 9, no. 4, pp. 1651-1658, 2009, doi: 10.1021/nl900034v.

[169] N. Liu, M. Hentschel, T. Weiss, A. P. Alivisatos, and H. Giessen, "Three-dimensional plasmon rulers," *Science,* vol. 332, no. 6036, pp. 1407-1410, 2011, doi: 10.1126/science.1199958.

[170] S. Law, D. C. Adams, A. M. Taylor, and D. Wasserman, "Mid-infrared designer metals," *Opt. Express,* vol. 20, no. 11, pp. 12155-12165, 2012, doi: 10.1364/OE.20.012155.

[171] C. Mätzler, "MATLAB functions for Mie scattering and absorption," Institut für Angewandte Physik, Bern, Switzerland, 2002.

[172] S. Basu, B. J. Lee, and Z. M. Zhang, "Infrared radiative properties of heavily doped ailicon at room temperature," *J. Heat Transfer,* vol. 132, no. 2, p. 023301, 2009, doi: 10.1115/1.4000171.

[173] J. D. Christesen, C. W. Pinion, E. M. Grumstrup, J. M. Papanikolas, and J. F. Cahoon, "Synthetically encoding 10 nm morphology in silicon nanowires," *Nano Lett.*, vol. 13, no. 12, pp. 6281-6286, 2013, doi: 10.1021/nl403909r.

[174] T. N. Theis, "Plasmons in inversion layers," *Surf. Sci.*, vol. 98, no. 1, pp. 515-532, 1980, doi: 10.1016/0039-6028(80)90533-6.

[175] G. V. Naik, V. M. Shalaev, and A. Boltasseva, "Alternative plasmonic materials: Beyond gold and silver," *Adv. Mater.,* vol. 25, no. 24, pp. 3264-3294, 2013, doi: 10.1002/adma.201205076.

[176] Y. Zhong, S. D. Malagari, T. Hamilton, and D. M. Wasserman, "Review of mid-infrared plasmonic materials," *J. Nanophotonics,* vol. 9, no. 1, p. 093791, 2015, doi: 10.1117/1.JNP.9.093791.

[177] M. Hocevar *et al.,* "Growth and optical properties of axial hybrid III–V/silicon nanowires," *Nat. Commun.,* vol. 3, p. 1266, 2012, doi: 10.1038/ncomms2277.

[178] M. F. Modest, *Radiative Heat Transfer,* 3 ed. New York: Academic Press, 2013.

[179] D. Li and C. Z. Ning, "All-semiconductor active plasmonic system in mid-infrared wavelengths," *Opt. Express,* vol. 19, no. 15, pp. 14594-14603, 2011, doi: 10.1364/OE.19.014594.

[180] Y. Wu, Y. Cui, L. Huynh, C. J. Barrelet, D. C. Bell, and C. M. Lieber, "Controlled growth and structures of molecular-scale silicon nanowires," *Nano Lett.*, vol. 4, no. 3, pp. 433-436, 2004, doi: 10.1021/nl035162i.

[181] K. Kloppstech *et al.*, "Giant heat transfer in the crossover regime between conduction and radiation," *Nat. Commun.*, vol. 8, p. 14475, 2017, doi: 10.1038/ncomms14475.

[182] L. Cui *et al.*, "Study of radiative heat transfer in Ångström- and nanometre-sized gaps," *Nat. Commun.*, vol. 8, p. 14479, 2017, doi: 10.1038/ncomms14479.

[183] V. Chiloyan, J. Garg, K. Esfarjani, and G. Chen, "Transition from near-field thermal radiation to phonon heat conduction at sub-nanometre gaps," *Nat. Commun.*, vol. 6, p. 6755, 2015, doi: 10.1038/ncomms7755.

[184] Z. Wang, J. E. Alaniz, W. Jang, J. E. Garay, and C. Dames, "Thermal conductivity of nanocrystalline silicon: Importance of grain size and frequency-dependent mean free paths," *Nano Lett.*, vol. 11, no. 6, pp. 2206-2213, 2011, doi: 10.1021/nl1045395.

[185] A. J. Minnich *et al.*, "Modeling study of thermoelectric SiGe nanocomposites," *Phys. Rev. B*, vol. 80, no. 15, p. 155327, 2009, doi: 10.1103/PhysRevB.80.155327.

[186] H. Lee, D. Vashaee, D. Z. Wang, M. S. Dresselhaus, Z. F. Ren, and G. Chen, "Effects of nanoscale porosity on thermoelectric properties of SiGe," *J. Appl. Phys.*, vol. 107, no. 9, p. 094308, 2010, doi: 10.1063/1.3388076.

[187] O. Yuji *et al.*, "Thermoelectric properties of heavily boron- and phosphorus-doped silicon," *Japanese Journal of Applied Physics*, vol. 54, no. 7, p. 071301, 2015, doi: 10.7567/JJAP.54.071301.

[188] C. Dames and G. Chen, "Theoretical phonon thermal conductivity of Si/Ge superlattice nanowires," *J. Appl. Phys.*, vol. 95, no. 2, pp. 682-693, 2003, doi: 10.1063/1.1631734.

[189] S. G. Walkauskas, D. A. Broido, K. Kempa, and T. L. Reinecke, "Lattice thermal conductivity of wires," *J. Appl. Phys.*, vol. 85, no. 5, pp. 2579-2582, 1999, doi: 10.1063/1.369576.

[190] S. M. Sze, *Physics of semiconductor devices*, 2nd ed. New York: Wiley, 1981.

[191] C. J. Fu and Z. M. Zhang, "Nanoscale radiation heat transfer for silicon at different doping levels," *Int. J. Heat Mass Transfer*, vol. 49, pp. 1703-1718, 2006, doi: 10.1016/j.ijheatmasstransfer.2005.09.037.

[192] Z. Tong, L. H. Liu, L. S. Li, and H. Bao, "Temperature-dependent infrared optical properties of 3C-, 4H- and 6H-SiC," *Physica B*, vol. 537, pp. 194-201, 2018, doi: 10.1016/j.physb.2018.02.023.

[193] B. Liu, J. Shi, K. Liew, and S. Shen, "Near-field radiative heat transfer for Si based metamaterials," *Opt. Commun.,* vol. 314, pp. 57-65, 2014, doi: 10.1016/j.optcom.2013.10.074.

[194] M. T. Pettes and L. Shi, "Thermal and structural characterizations of individual single-, double-, and multi-walled carbon nanotubes," *Adv. Funct. Mater.,* vol. 19, no. 24, pp. 3918-3925, 2009, doi: 10.1002/adfm.200900932.

[195] H. B. Callen and T. A. Welton, "Irreversibility and generalized noise," *Physical Review,* vol. 83, no. 1, pp. 34-40, 1951, doi: 10.1103/PhysRev.83.34.

[196] E. M. Lifshitz and L. P. Pitaevski, "Chap. VIII, Electromagnetic Fluctuations," in *Course of Theoretical Physics, Statistical Physics Part 2,* vol. 9. Oxford: Pergamon, 1980, ch. VIII, pp. 314-359.

[197] A. Manjavacas and F. J. Garcia de Abajo, "Vacuum friction in rotating particles," *Phys Rev Lett,* vol. 105, no. 11, p. 113601, 2010, doi: 10.1103/PhysRevLett.105.113601.

[198] E. J. Tervo, M. Francoeur, B. A. Cola, and Z. M. Zhang, "Thermal radiation in systems of many dipoles," 2019, arXiv:1906.10003 [cond-mat.mes-hall].

[199] A. D. Yaghjian, "Electric dyadic Greens-functions in the source region," *Proc. IEEE,* vol. 68, no. 2, pp. 248-263, 1980, doi: 10.1109/Proc.1980.11620.

[200] N. de Sousa, L. S. Froufe-Pérez, J. J. Sáenz, and A. García-Martín, "Magneto-optical activity in high index dielectric nanoantennas," *Sci. Rep.,* vol. 6, p. 30803, 2016, doi: 10.1038/srep30803.

[201] A. Manjavacas and F. J. García de Abajo, "Radiative heat transfer between neighboring particles," *Phys. Rev. B,* vol. 86, no. 7, p. 075466, 2012, doi: 10.1103/PhysRevB.86.075466.

[202] E. J. Tervo, Z. M. Zhang, and B. A. Cola, "Collective near-field thermal emission from polaritonic nanoparticle arrays," *Phys. Rev. Mater.,* vol. 1, no. 1, p. 015201, 2017, doi: 10.1103/PhysRevMaterials.1.015201.

[203] E. J. Tervo, B. A. Cola, and Z. M. Zhang, "Near-field radiative thermal conductivity of nanoparticle chains," in *16th International Heat Transfer Conference*, Beijing, China, 2018: Begell House, 2018, pp. 8313-8319, doi: 10.1615/IHTC16.rti.023143.

[204] A. Yuksel and M. Cullinan, "Modeling of nanoparticle agglomeration and powder bed formation in microscale selective laser sintering systems," *Addit. Manuf.,* vol. 12, pp. 204-215, 2016, doi: 10.1016/j.addma.2016.07.002.

[205] M. A. Yurkin and A. G. Hoekstra, "User manual for the discrete dipole approximation code ADDA 1.4.0-alpha," 2018, https://github.com/adda-team/adda/raw/v1.4.0/doc/manual.pdf.

[206] A. Yuksel, E. T. Yu, M. Cullinan, and J. Murthy, "Effect of particle size distribution on near-field thermal energy transfer within the nanoparticle packings," *J. Photonics Energy,* vol. 9, no. 3, pp. 1-11, 11, 2019, doi: 10.1117/1.JPE.9.032707.

[207] E. J. Tervo, B. A. Cola, and Z. M. Zhang, "Validity of kinetic theory for radiative heat transfer in nanoparticle chains," in *The 9th International Symposium on Radiative Transfer,* Athens, Greece, 2019, arXiv:1901.10608 [cond-mat.mes-hall]: Begell House.

[208] A. V. Shchegrov, K. Joulain, R. Carminati, and J. J. Greffet, "Near-field spectral effects due to electromagnetic surface excitations," *Phys. Rev. Lett.,* vol. 85, no. 7, pp. 1548-1551, 2000, doi: 10.1103/PhysRevLett.85.1548.

[209] A. D. Phan, T. L. Phan, and L. M. Woods, "Near-field heat transfer between gold nanoparticle arrays," *J. Appl. Phys.,* vol. 114, no. 21, p. 214306, 2013, doi: 10.1063/1.4838875.

[210] D. Z. A. Chen, "Energy transmission through and along thin films mediated by surface phonon-polaritons," Doctor of Philosophy, Mechanical Engineering, Massachusetts Institute of Technology, Cambridge, MA, 2007. [Online]. Available: http://dspace.mit.edu/handle/1721.1/42067

[211] R. Geick, C. H. Perry, and G. Rupprecht, "Normal modes in hexagonal boron nitride," *Physical Review,* vol. 146, no. 2, pp. 543-547, 1966, doi: 10.1103/PhysRev.146.543.

[212] B. Willingham and S. Link, "Energy transport in metal nanoparticle chains via sub-radiant plasmon modes," *Opt. Express,* vol. 19, no. 7, pp. 6450-61, 2011, doi: 10.1364/OE.19.006450.

[213] T. G. Folland *et al.,* "Probing hyperbolic polaritons using infrared attenuated total reflectance micro-spectroscopy," *MRS Commun.,* vol. 8, no. 4, pp. 1418-1425, 2018, doi: 10.1557/mrc.2018.205.

[214] T. L. Bergman, F. P. Incropera, A. S. Lavine, and D. P. DeWitt, *Fundamentals of heat and mass transfer,* seventh ed. John Wiley & Sons, 2011.

[215] G. Chen, *Nanoscale energy transport and conversion*. Oxford University Press, New York, 2005.